A Linear Algebraic Framework for Autofocus in Synthetic Aperture Radar

by

Kuang-Hung Liu

A dissertation submitted in partial fulfillment
of the requirements for the degree of
Doctor of Philosophy
(Electrical Engineering-Systems)
in The University of Michigan
2011

Doctoral Committee:

Professor David C. Munson, Jr., Chair
Professor Alfred O. Hero III
Associate Professor Martin J. Strauss
Assistant Professor Clayton D. Scott
Assistant Professor Ami Wiesel, Hebrew University of Jerusalem

© $\frac{\text{Kuang-Hung Liu}}{\text{All Rights Reserved}}$ 2011

To My Family.

ACKNOWLEDGMENTS

I would first like to express my most sincere gratitude to my thesis advisor, Prof. David C. Munson, Jr., whose guidance and encouragement have made this thesis possible. Prof. Munson's support and patience from the preliminary to the concluding level enabled me to experiment on research ideas with great freedom. His energy and optimism has offered great momentum and inspiration throughout my doctoral research. Prof. Munson's influential role as a mentor and friend will continue to guide me in all of my future endeavors.

I am grateful to Prof. Ami Wiesel of the Hebrew University of Jerusalem for his guidance and friendship. His reasoning and insight has help me to mature as a researcher. Without his collaboration I could not have achieved such fruitful results. I would also like to thank my committee members for their insightful discussion and constructive feedback which has paved the way for completion of this thesis.

I am heartily thankful to my colleagues and friends both here at Michigan and back in Taiwan; your friendship and encouragement has supported me as I hurdled all the obstacles in my graduate studies. I deeply appreciate the University and all faculty and staff members of the EECS department for providing such a friendly and intellectually stimulating environment; this has been an unforgettable experience and I cherish every moment of it.

Last but not the least, I wish to express my love and gratitude to my parents, brother and my beloved wife, Wei-Ya, for their endless support and understanding as I have pursued my dream.

TABLE OF CONTENTS

CHAPTER

LIST OF FIGURES

Figure

ABSTRACT

Synthetic aperture radar (SAR) provides a means of producing high-resolution microwave images using an antenna of small size. SAR images have wide applications in surveillance, remote sensing, and mapping of the surfaces of both the Earth and other planets. The defining characteristic of SAR is its coherent processing of data collected by an antenna at locations along a trajectory in space. In principle, we can produce an image of extraordinary resolution. However, imprecise position measurements associated with data collected at each location cause phase errors that, in turn, cause the reconstructed image to suffer distortion, sometimes so severe that the image is completely unrecognizable. Autofocus algorithms apply signal processing techniques to restore the focused image.

This thesis focuses on the study of the SAR autofocus problem from a linear algebraic perspective. We first propose a general autofocus algorithm, called Fourier-domain Multichannel Autofocus (FMCA), that is developed based on an image support constraint. FMCA can accommodate nearly any SAR imaging scenario, whether it be wide-angle or bistatic (transmit and receive antennas at separate locations). The performance of FMCA is shown to be superior compared to current state-of-the-art autofocus techniques.

Next, we recognize that at the heart of many autofocus algorithms is an optimization problem, referred to as a constant modulus quadratic program (CMQP). Currently, CMQP generally is solved by using an eigenvalue relaxation approach. We propose an alternative relaxation approach based on semidefinite programming, which has recently attracted considerable attention in other signal processing applications. Preliminary results show that the new method provides promising performance advantages at the expense of increasing computational cost.

Lastly, we propose a novel autofocus algorithm based on maximum likelihood estimation, called maximum likelihood autofocus (MLA). The main advantage of MLA is its reliance on a rigorous statistical model rather than on somewhat heuristic reverse-engineering arguments. We show both the analytical and experimental advantages of MLA over existing autofocus methods.

CHAPTER 1

Introduction

Synthetic aperture radar (SAR) is used to produce a high-resolution microwave image using a small antenna. High resolution in the range direction is achieved through traditional pulse compression, while high resolution in the cross-range direction is obtained by illuminating the target from many viewing angles (called the radar's look angles). In one form of SAR, termed *spotlight mode*, the radar antenna is continuously steered to illuminate the target with each transmitted microwave pulse. When the same antenna is used for both transmitting and receiving, it is referred to as *monostatic* SAR, while in *bistatic* SAR, spatially separated antennas are used for transmitting and receiving. In this thesis, we will focus on spotlight mode SAR and consider both monostatic and bistatic applications. Figure 1.1 illustrates imaging using spotlight mode SAR where a small antenna is mounted on an aircraft and is continuously steered to illuminate the scene of interest with each transmitted microwave pulse. In this chapter, we will first briefly review the tomographic formulation of SAR, as this will serve as the foundation for all subsequent discussions. Then we will introduce the cause and effect of autofocus phase errors for both monosatatic and bistatic SAR systems. We will conclude this introductory chapter with a review of existing autofocus methods and an overview of this thesis. For some applications of SAR imaging, please refer to [1, 2, 3].

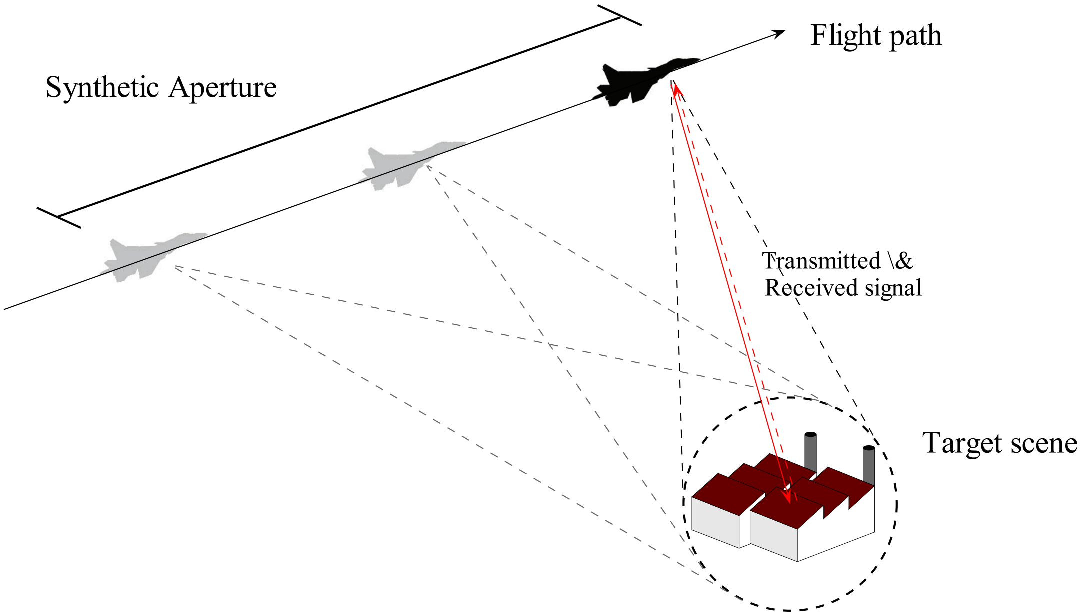

Figure 1.1: Example of spotlight mode monostatic SAR.

1.1 Tomographic Formulation of SAR System and Image Formation

The collected return signal in SAR can be conveniently modeled using a tomographic formulation, which allows us to view returned signals as data lying in the *Fourier domain* of the target reflectivity, after demodulating with a copy of the transmitted signal [4]. The location of the data in the Fourier domain lies on a polar annulus and is a function of the radar waveform parameters and the radar's look angle, which are known to us. Thus, image reconstruction can be obtained through the traditional polar formatting algorithm [4, 5].

Figure 1.2 shows the "plan view" geometry of a monostatic SAR, where the target scene of radius L is illuminated, and the return signal is collected, by the radar traversing a range of look angles $\theta_m : \theta_{min} \leq \theta_m \leq \theta_{max},\ m = 1, 2, \ldots, M$. The goal is to construct the target's continuous complex-valued reflectivity function $r(x, y)$ and use its magnitude $|r(x, y)|$ for image display. The following assumptions made throughout this thesis are crucial to the problem formulation.

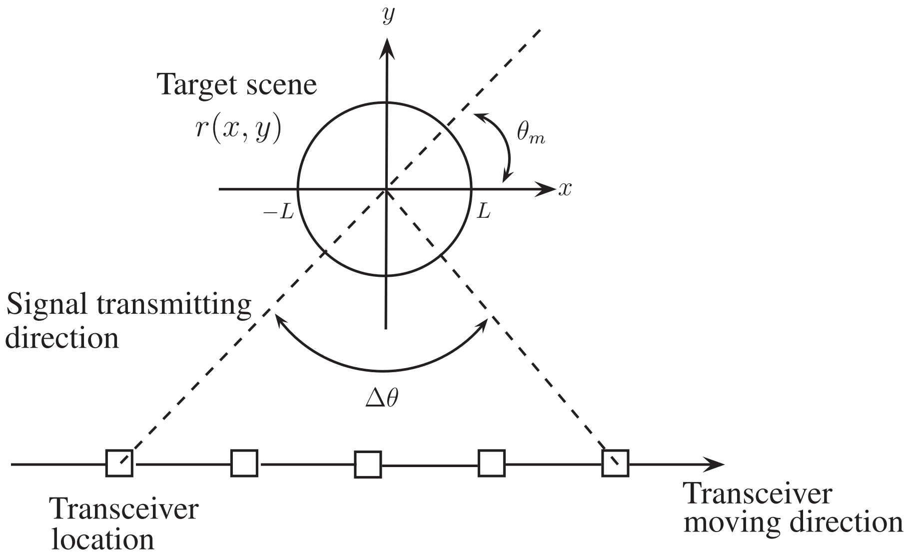

Figure 1.2: Geometry of spotlight-mode monostatic SAR

1. *Far-field assumption*: Unless otherwise specified, we assume that the radar platform operates at a standoff distance that is large compared to the target scene diameter. Under this assumption, when the transmitted radar pulse reaches the target, it can be well approximated by a planar wavefront.
2. *Reflectivity invariance*: The target reflectivity function $r(x, y)$ is assumed to be independent of both the look angle and the frequency of incident radiation.

From the far-field assumption, data collection at look angle, θ_m, can be conceptually viewed as collecting information from the 1-D projection of $r(x, y)$ at angle θ_m. This is illustrated in Fig. 1.3. The 1-D projection function, $p_{\theta_m}(\bar{y})$, indexed by m is given by

$$p_{\theta_m}(\bar{y}) = \int_{-L}^{L} r(\bar{x}\cos\theta_m - \bar{y}\sin\theta_m,\ \bar{x}\sin\theta_m + \bar{y}\cos\theta_m)\, d\bar{x}. \tag{1.1}$$

In this work, we assume that the radar is transmitting a narrow-band linear FM

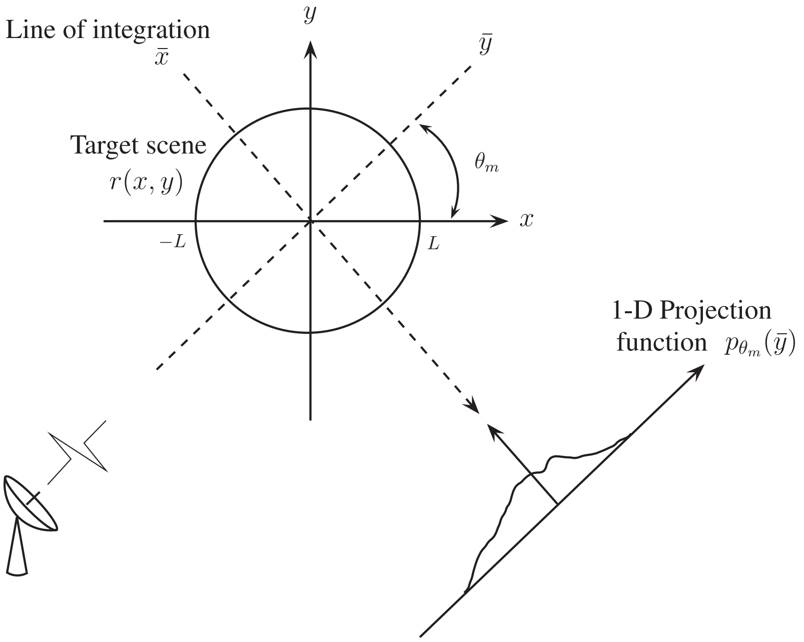

Figure 1.3: 1-D Projection function

pulse of the form $\mathrm{Re}\{s(t)\}$ with

$$s(t) = \begin{cases} \exp\Big(j(\omega_0 t + \alpha t^2)\Big) & |t| \leq T/2 \\ 0 & \text{otherwise,} \end{cases}$$

where ω_0 is the carrier frequency, T is the duration of the pulse, and 2α is the FM rate. The collected return signal is then demodulated with $\mathrm{Re}\{s(t)\}$ and $-\mathrm{Im}\{s(t)\}$, each delayed by the two-way travel time from the transmitter to the target to the receiver, and low-pass filtered to remove the high-frequency term to produce a baseband signal. The baseband signal collected from look angle θ_m, denoted by $P_{\theta_m}(\bar{Y})$, can be expressed as

$$P_{\theta_m}(\bar{Y}) = \int_{\infty}^{\infty} p_{\theta_m}(\bar{y})\, e^{-j\bar{y}\bar{Y}}\, d\bar{y}, \tag{1.2}$$

which is the 1-D Fourier transform of $p_{\theta_m}(\bar{y})$.

Let $R(\Omega_x, \Omega_y)$ be the 2-D Fourier transform of $r(x,y)$. From the projection slice theorem in tomography, $P_{\theta_m}(\bar{Y})$ is equal to $R(\Omega_x, \Omega_y)$ evaluated along a line in Fourier

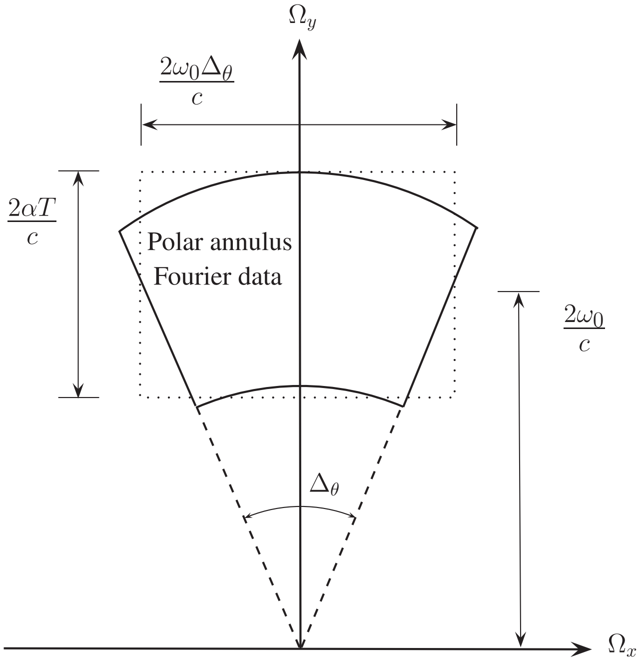

Figure 1.4: Collected Fourier data for monostatic SAR

space that lies at angle θ_m measured from axis Ω_x. The duration of the transmitted pulse, T, provides a restriction on the range of frequencies over which $P_{\theta_m}(\bar{Y})$ is acquired, and the carrier frequency ω_0 causes $P_{\theta_m}(\bar{Y})$ to be offset from the origin of Fourier space [4]. $P_{\theta_m}(\bar{Y})$ can be described as

$$P_{\theta_m}(\bar{Y}) = \begin{cases} R(\bar{Y}\cos\theta_m, \bar{Y}\sin\theta_m) & \frac{2}{c}(\omega_0 - \alpha T) \le \bar{Y} \le \frac{2}{c}(\omega_0 + \alpha T) \\ 0 & \text{otherwise.} \end{cases} \tag{1.3}$$

It can be observed from Eqn. (1.3) that the collected Fourier data from many look angles lie on a polar annulus as shown in Fig. 1.4. The Fourier data have frequency offset $\frac{2\omega_0}{c}$ and bandwidth described by the range of look angles and the duration of the transmitted FM signal [5]. In practice, not only do we collect data from discrete look angles, θ_m, we also collect discrete samples from each of the $P_{\theta_m}(\bar{Y})$. Let $\bar{Y}_1, \cdots, \bar{Y}_N$ denote the sample indices of $P_{\theta_m}(\bar{Y})$. In summary, we are collecting 2-D discrete samples on the Fourier space of $r(x, y)$ evaluated on a polar grid. Let $\mathrm{G}[m, n]$ denote the collected

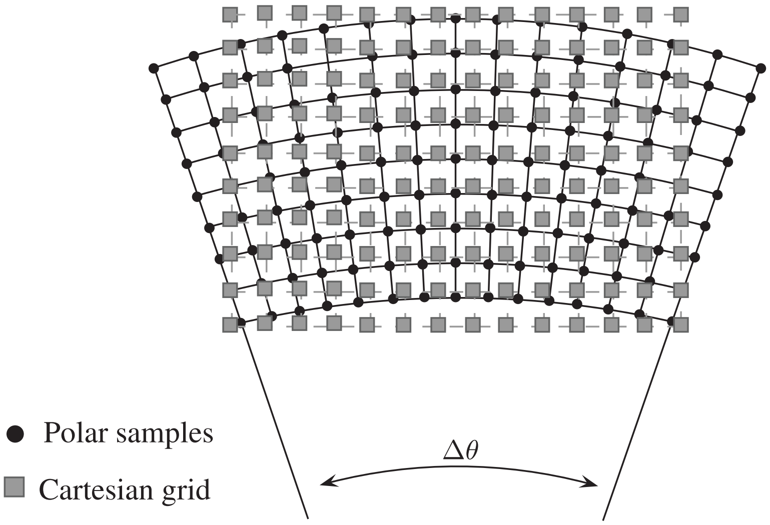

Figure 1.5: Interpolation to Cartesian grid

discrete Fourier data. Then

$$\mathrm{G}[m,n] = P_{\theta_m}(\bar{Y}_n). \tag{1.4}$$

From $\mathrm{G}[m,n]$ we could reconstruct a discrete image of $r(x,y)$, denoted by $g[u,v]$, using a discretized inverse Fourier transform. However, performing the straightforward inverse Fourier transform would be computationally expensive due to the nonuniform grid that $\mathrm{G}[m,n]$ lies on. In SAR imaging, a popular image reconstruction method is to first interpolate the Fourier data from a nonuniform grid to a Cartesian grid and then use an inverse FFT to form the final image as suggested in Fig. 1.5. In practice, a linear interpolator is almost always used for the polar-to-Cartesian interpolation; for example see [5]. The explanation of the feasibility of using only an offset portion of the Fourier data for image reconstruction is provided in [6]. Other image reconstruction methods are discussed in [7, 8, 9, 10, 11].

Next, we briefly review the tomographic formulation for a bistatic SAR. The geometry of a bistatic SAR with a stationary transmitter and moving receiver is shown in Fig. 1.6. Such a scenario is sometimes used where a high-powered transmitter stands off in a safe location and the receiver covertly collects data to form the SAR image. It

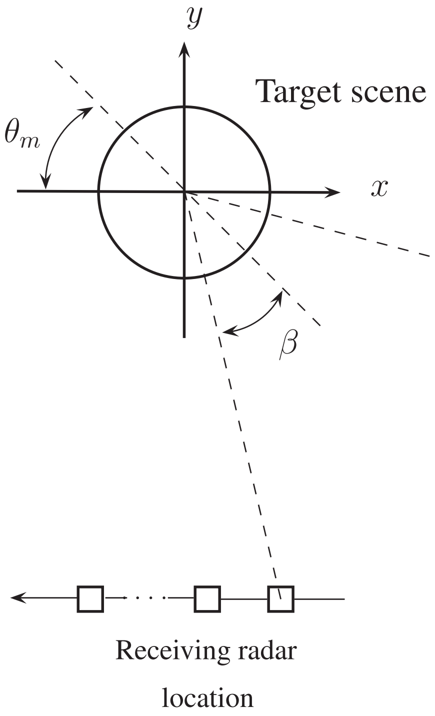

Figure 1.6: Geometry of spotlight-mode bistatic SAR

can be shown that the demodulated collected return signal $P_{\theta_m}(\bar{Y})$ also corresponds to a radial slice at angle θ_m of the 2-D Fourier transform of $r(x,y)$ [12]. In bistatic SAR, $P_{\theta_m}(\bar{Y})$ has the form of

$$P_{\theta_m}(\bar{Y}) = \begin{cases} R(\bar{Y}\cos\theta_m, \bar{Y}\sin\theta_m) & \frac{2|\cos(\beta)|}{c}(\omega_0 - \alpha T) \le \bar{Y} \le \frac{2|\cos(\beta)|}{c}(\omega_0 + \alpha T) \\ 0 & \text{otherwise.} \end{cases} \tag{1.5}$$

The collected Fourier data grid for this bistatic SAR system is shown in Fig. 1.7. As in the monostatic case, image reconstruction can be accomplished via interpolation of the Fourier data to a Cartesian grid, followed by an inverse FFT.

1.2 SAR Autofocus Problem

A challenge in SAR imaging is that in order to correctly (coherently) demodulate the return signals, the two-way travel time of each radar pulse must be known accurately.

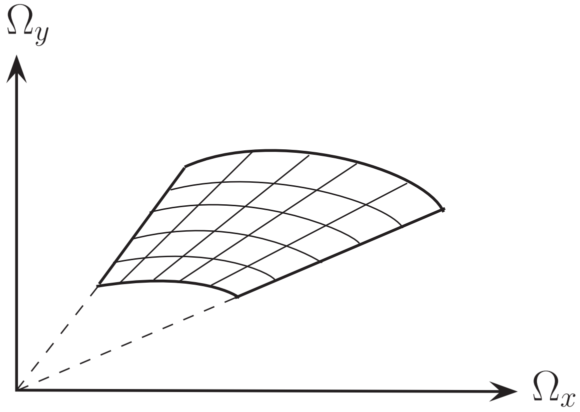

Figure 1.7: Collected Fourier data grid for bistatic SAR

Let τ_m denote the two-way travel time for radar pulse from look angle θ_m. Then the collected returned signal should be demodulated with

$$\mathrm{Re}\{s(t-\tau_m)\} \quad \text{and} \quad -\mathrm{Im}\{s(t-\tau_m)\}. \tag{1.6}$$

However, inaccurate time measurements, due to imprecise knowledge of the location of the radar or due to signals propagating through media having a spatially-varying propagation velocity, cause an unknown delay error of ε_m in the demodulated signal. Thus, in practice, the signal is demodulated with

$$\mathrm{Re}\{s(t-\tau_m+\varepsilon_m)\} \quad \text{and} \quad -\mathrm{Im}\{s(t-\tau_m+\varepsilon_m)\} \tag{1.7}$$

instead. This timing delay error can be closely approximated as introducing an unknown constant phase shift to the demodulated radar returns [5]. Since data collected from the same look angle are associated with the same timing delay error, the phase corruption are modeled as constant for all Fourier data collected from a fixed angle. More specifically, let $\tilde{\mathrm{G}}[m,n]$ denote the collected phase corrupted Fourier data, which are related to the uncorrupted Fourier data $\mathrm{G}[m,n]$ by

$$\tilde{\mathrm{G}}[m,n] = \mathrm{G}[m,n]\; e^{j\varepsilon_m \omega_0}. \tag{1.8}$$

Without loss of generality, we will denote the unknown phase as $\phi(m) = \varepsilon_m \omega_0,\ m = 1, \cdots, M$. In practice, $\phi(m)$ may range from highly correlated to *i.i.d.*, depending on the center frequency of the radar (shorter wavelengths lead to more variable $\phi(m)$) the errors in estimating the trajectory of the radar platform, and time and spatially varying signal propagation effects. The presence of the phase errors will cause the reconstructed image to suffer distortion resulting in a defocused image. The defocusing effect comes from Eqn. (1.8), which has the equivalent effect of convolving the focused image with a blurring kernel. The blurring kernel is both 2-D and spatially varying, because the phase error in Eqn. (1.8) varies with the angular coordinate in a polar (non-Cartesian) coordinate system. One approach to sometimes remedy this undesired effect is to improve the physical system design, which will often result in more expensive hardware. An alternative approach is to apply more sophisticated signal processing to the image formation process. In particular, signal processing can be applied to automatically remove undesired phase errors. This image restoration technique is called autofocus.

In summary, a SAR system with and without autofoucs phase corruption is depicted in Fig. 1.8.

1.3 Related Work

The SAR autofocus problem is, in general, an ill-conditioned inverse problem. In order for the problem to be well defined, it is common practice to impose additional constraints either on the underlying image or the imaging system. Here, we review previous autofocus algorithms and discuss their strengths and weaknesses.

Many algorithms have been developed for the SAR autofocus problem. Most of them

Without autofocus phase error

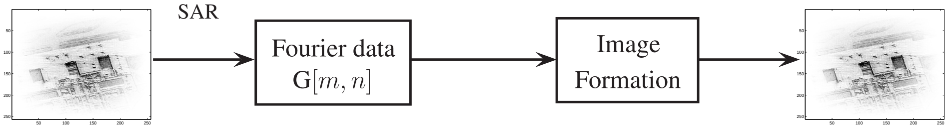

With autofocus phase error

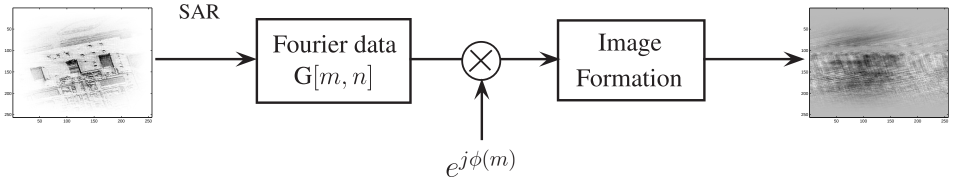

Figure 1.8: Summary of SAR autofocus problem.

are for the monostatic SAR scenario, due to its wide application. Earlier autofocus algorithms assume (explicitly or implicitly) simple models for either the underlying image or autofocus phase errors. Inverse filtering methods produce phase estimates by isolating the blurring kernel of a single point target from the rest of the image. A main drawback of this approach is the difficulty of isolating point targets in a real SAR image. Another earlier autofocus algorithm, which met with some success, is the map drift algorithm [13, 14, 15]. Map drift is based on two assumptions: first, it assumes that the autofocus phase error function can be completely described by a finite polynomial expansion, and second, it assumes that the SAR is operating over a narrow range of look angles so that the Fourier data grid is nearly Cartesian. In practice, map drift can perform well in situations where the autofocus phase function can be adequately described by a low-order polynomial. For situations where the SAR operates over a wide range of look angles or when a higher-order autofocus phase function is involved, map drift becomes considerably nonideal.

Phase gradient autofocus (PGA) is the most widely applied autofocus algorithm to date [16]. It is based on two assumptions: the first one is that SAR operates over a narrow range of look angles, and the second assumption, also the most crucial one, is that the scene contains strong point targets. Unlike inverse filtering, PGA iteratively combines phase error information gathered from all the point targets to produce a more robust phase error estimate. Hypothetically, PGA can correct phase errors of any form. In practice, it is more challenging for PGA to correct a white or rapidly varying autofocus phase function. For more information about PGA and its extensions, please refer to [5, 17, 18, 19, 20].

Another popular class of autofocus algorithms is called sharpness maximization autofocus. These algorithms are based on the assumption that a focused image should also be a sharp image. When a sharpness metric is defined, an autofocus method can be constructed to compensate the phase errors by maximizing the sharpness of the reconstructed image [21, 22, 23, 24, 25, 26, 27]. Popular metrics that measure image sharpness include entropy and various powers of the image intensity [28]. These algorithms tend to favor sparse images, such as collections of point scatterers. While the restoration results obtained using these methods often are outstanding, the techniques sometimes fail to produce correct restorations when the underlying scene is poorly described by the implicitly assumed image model. Furthermore, the use of an heuristic sharpness measure makes it hard to provide any performance guarantee.

More recently, a promising autofocus method, called multichannel autofocus (MCA), has been developed based on the image support constraint [29]. Unlike other assumptions used by previous methods, the image support constraint can be enforced by the antenna pattern in any practical system. MCA determines the phase errors through a linear algebraic formulation by assuming a spatially limited image. MCA exhibits superior restoring capability compared with other methods and does not depends on characteristics of the image. One crucial assumption of MCA is that the Fourier data grid is Cartesian, so the SAR must operate over a narrow range of look angles. It has been found that when this assumption is violated, even slightly, MCA suffers significant performance loss [30]. Further discussion of MCA will be provided in the next chapter.

In summary, all of the above mentioned autofocus methods place different assumptions either on the unknown phase error, underlying image or imaging scenario. The assumption that SAR operates across a narrow range of look angles is crucial to many autofocus algorithms and we will discuss this assumption more thoroughly in the next chapter.

1.4 Thesis Outline and Contributions

The objective of our work is to develop a general autofocus algorithm that can accommodate the broadest range of SAR imaging applications. The following is the outline of this thesis and our contributions.

Chapter 2: This chapter presents a new autofocus algorithm, termed Fourier-domain multichannel autofocus (FMCA), that is derived under a linear algebraic framework, allowing the SAR image to be focused in a noniterative fashion. Motivated by the mutichannel autofocus (MCA) approach, the proposed autofocus algorithm invokes the assumption of a low-return region, which generally is provided within the antenna sidelobes. Unlike MCA, FMCA works with the collected polar Fourier data directly and is capable of accommodating both wide-angle monostatic SAR and bistatic SAR scenarios. Most autofocus algorithms rely on the assumption that the radar's range of look angles is small so that the phase errors can be modeled as varying along only one dimension in the spatial image. And, in some cases, implicit assumptions are made regarding the SAR scene. Performance of such autofocus algorithms degrades if the assumptions are not satisfied. FMCA has the advantage that it does not require prior assumptions about the range of look angles, nor characteristics of the scene.

Chapter 3: At the heart of three state-of-the-art autofocus algorithms, namely Phase Gradient Autofocus, Multichannel Autofocus and Fourier-domain Multichannel Autofocus, is the solution to a constant modulus quadratic program (CMQP). Currently, these algorithms solve CMQP by using an eigenvalue relaxation approach. We propose an alternative relaxation approach based on semidefinite programming, which has recently attracted considerable attention in other signal processing problems. Experimental results show that our proposed methods provide promising performance advantages in exchange for an increase in computational cost.

Chapter 4: In this chapter, we propose a bilinear parametric model for the unknown image and the nuisance autofocus phase parameters, and derive an efficient maximum likelihood autofocus (MLA) algorithm. In the special case of a simple image model and a narrow range of look angles, MLA coincides with the successful multichannel autofocus (MCA) approach. MLA can be interpreted as a generalization of MCA to a larger class of models with a larger range of look angles. We analyze its advantages over previous extensions of MCA in terms of identifiability conditions as well as noise sensitivity. We demonstrate the superior performance of MLA using computer simulations for both the correct and mismatched system models. MLA performs better than other methods both in terms of mean squared error and visual quality of the restored image.

1.5 Notation

In this thesis, a capital boldface letter $\mathbf{A}$ denotes a matrix and a lower-case boldface letter $\mathbf{a}$ denotes a column vector. A superscript ^{H} denotes the hermitian transpose and † denotes the pseudo-inverse. The function $\mathrm{vec}(\mathbf{A})$ stacks the columns of matrix $\mathbf{A}$ to produce a column vector. Let $\mathrm{tr}(\mathbf{A})$ denote the trace of matrix $\mathbf{A}$, and $\mathrm{Diag}(\mathbf{a})$ be the diagonal matrix with elements of vector $\mathbf{a}$ on the main diagonal. Let $\mathrm{rank}(\mathbf{A})$ denote the rank of matrix $\mathbf{A}$, and $\mathcal{N}(\mathbf{A})$ denote the null space of $\mathbf{A}$. We write $\mathbf{A} \succeq 0$ to indicate that $\mathbf{A}$ is a positive semidefinite matrix. For an index set s, $\mathbf{A}_s(\mathbf{A}^s)$ represents the submatrix of $\mathbf{A}$ formed by the rows(columns) of $\mathbf{A}$ indexed by s. For a complex number c, $|c|$ represents the magnitude of c and $\angle(c)$ represents the phase of c.

CHAPTER 2

Fourier-domain Multichannel Autofocus

Motivated by Multichannel autofocus (MCA), Fourier-domain Multichannel Autofocus (FMCA) applies a subspace-based technique to the autofocus problem and constructs a subspace where the focused image resides. The basis of the subspace is found from the corrupted Fourier data. By requiring that the underlying SAR image have a region with zero or nearly-zero pixel values, and establishing the relationship between the SAR image and the collected Fourier data, we can write a set of linear equations that allow us to determine the phase errors directly [31, 32]. The requirement for this known region with zero (or nearly zero) pixel values generally is satisfied by the low-return region within the sidelobes of the antenna pattern. In practice, this region is created by acquiring the collected returned signals with sufficiently small sample spacings in both the range and cross-range frequency coordinates, so that the reconstructed image has coverage extending beyond the heavily illuminated portion of the target scene determined by the antenna pattern. This linear framework allows us to determine the phase errors in a noniterative fashion, and the formulation of the reconstruction problem does not depend on characteristics of the underlying scene. Although in our approach it is more complicated to express the relationship between the spatial image and the autofocus phase errors, compared to MCA and PGA, it is this Fourier-domain observation that allows our algorithm to accommodate wide-angle monostatic SAR and bistatic SAR.

The organization of this chapter is as follows. First we briefly review the MCA framework in Section 2.1. Then we derive the FMCA framework and propose a procedure for image restoration in Section 2.2. Section 2.3 compares FMCA with MCA. Simulation results are presented in Section 2.4. Finally, a summary of this chapter is given in Section 2.5.

2.1 Review of Multichannel Autofocus

In this section, we introduce the fundamental assumptions and limitations of the MCA framework, as this will help to distinguish our work from MCA. For a complete description of MCA, please refer to [29]. MCA is based on two important assumptions: that the image support is known, and that the SAR operates over a narrow range of look angles. We first will elaborate on these two concepts and then show how MCA exploits these two assumptions to compensate for the autofocus phase errors.

2.1.1 Small-angle Assumption

The assumption that the SAR operates over a narrow range of look angles, or the small-angle assumption, for short, is crucial for many prevalent autofocus algorithms, including PGA and MCA. Here we discuss how the small-angle assumption simplifies the autofocus problem.

From Eqn. (1.8), each column of the actual collected Fourier data, $\tilde{\mathrm{G}}$, is corrupted by the same multiplicative phase error $e^{j\phi(m)}$, therefore, the phase error is essentially a one-dimensional (1-D) function. In the following, we will show how the small-angle assumption transforms the phase errors into a 1-D function in the *spatial domain* so that with additional information on image characteristics, this 1-D phase function can be compensated.

When the range of look angles is sufficiently small, i.e., $\Delta\theta \ll 1$, we can observe from Fig. 1.4 that the collected polar formatted Fourier data lie approximately on a Cartesian grid. Denote the collected Cartesian grid Fourier data as $\mathrm{G}_c[m,n]$. By first examining the *range-compressed* form of G_c where a 1-D inverse DFT is applied to each column of G_c, i.e.,

$$\mathrm{G}_c[m,v] = \mathrm{DFT}_n^{-1}(\mathrm{G}_c[m,n]), \tag{2.1}$$

we have

$$\widetilde{\mathrm{G}}_c[m,v] = \mathrm{G}_c[m,v]\; e^{j\phi(m)}. \tag{2.2}$$

Ideally, the SAR image, $g[u,v]$, can be formed by applying an additional 1-D inverse DFT on each row of the range-compressed data, giving

$$g[u,v] = \mathrm{DFT}_m^{-1}(\mathrm{G}_c[m,v]). \tag{2.3}$$

However, due to the phase errors, we produce a defocused image, $\tilde{g}[u,v]$, given as

$$\begin{aligned} \tilde{g}[u,v] &= \mathrm{DFT}_m^{-1}(\widetilde{\mathrm{G}}_c[m,v]) \\ &= \mathrm{DFT}_m^{-1}(\mathrm{G}_c[m,v]\; e^{j\phi(m)}) \\ &= g[u,v] \otimes e[u] \end{aligned} \tag{2.4}$$

where $\otimes$ denotes M-point circular convolution and

$$e[u] = \mathrm{DFT}_m^{-1}(e^{j\phi(m)}). \tag{2.5}$$

From Eqn. (2.4), we can see that the defocused image $\tilde{g}[u,v]$ is essentially formed by convolving each row of the perfectly-focused image with a common blurring kernel $e[u]$. Due to the all-pass property of Eqn. (2.2), there exists an inverse function for $e[u]$, denoted as $b[u]$, such that

$$g[u,v] = \tilde{g}[u,v] \otimes b[u]. \tag{2.6}$$

This spatial 1-D phase error model is used by most autofocus algorithms. In summary, although the phase error function, $\phi(m)$, is one dimensional, it has a 2-D effect on the spatial image, due to the nonuniform Fourier data grid. The small-angle assumption assures the data collection is on a nearly Cartesian grid, resulting in a simple 1-D phase error blurring model for the spatial image, as in Eqn. (2.4).

2.1.2 Image Support Constraint

Image support constraint is the other important assumption that MCA relies on. Image support constraint can be translated into requiring the underlying SAR image to have a known region with zero or nearly-zero pixel values (low-return region). The requirement for the known low-return region generally is satisfied by the nulls within the sidelobes of the antenna pattern. In practice, the nulls of the antenna pattern can be identified with extreme accuracy.

The section of terrain that is imaged by a SAR depends on the antenna footprint, which is the region illuminated by the antenna beam with significant energy. Energy collected from outside the antenna footprint is small. This is illustrated in Fig. 2.1. Consequently, the low-return region can be created by acquiring the collected returned signals with sufficiently small sample spacings in both the range and cross range directions, so that the reconstructed image has coverage extending beyond the heavily illuminated portion of the target scene determined by the antenna pattern. Note that the low-return region can also be found from other parts of the image, for example, a body of water which does not reflect electromagnetic waves can also be used as the low-return region if known. However, low-return regions in the nulls of the antenna pattern suffices for all SAR imaging applications.

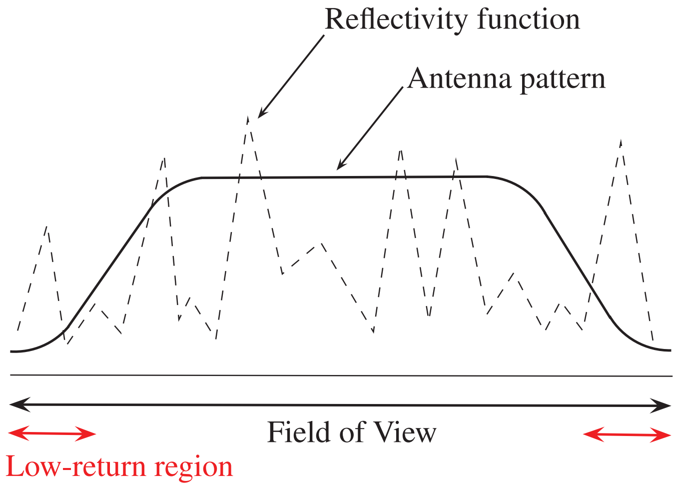

Figure 2.1: Low-return region

2.1.3 MCA Formulation

From the small-angle assumption, MCA transforms the phase errors into an 1-D function in the spatial domain as shown in Eqn. (2.6). This can be reexpressed using matrix notations:

$$\underline{g} = \mathbf{C}(\tilde{g})\,\mathbf{b}, \tag{2.7}$$

where

$$\underline{g} = \mathrm{vec}(g) \tag{2.8}$$

and

$$\mathbf{C}(\tilde{g}) = \begin{bmatrix} \mathbf{H}_1(\tilde{g}) \\ \mathbf{H}_2(\tilde{g}) \\ \vdots \\ \mathbf{H}_N(\tilde{g}) \end{bmatrix}, \quad \mathbf{H}_i(\tilde{g}) = \begin{bmatrix} g[1,i] & g[M,i] & \cdots & g[2,i] \\ g[2,i] & g[1,i] & \cdots & g[3,i] \\ \vdots & \vdots & \ddots & \vdots \\ g[M,i] & g[M-1,i] & \cdots & g[1,i] \end{bmatrix} \tag{2.9}$$

Low-return region corresponds to a known set of indices a such that

$$\underline{g}_a = [\mathbf{C}(\tilde{g})]_a\,\mathbf{b} = \mathbf{0}. \tag{2.10}$$

Equation (2.10) is a set of linear equation that only depends on the SAR measurements, $\tilde{g}$, and MCA finds the autofocus phase compensation vector $\mathbf{b}$ by solving Eqn. (2.10).

2.2 FMCA Restoration Framework

The FMCA reconstruction method assumes there exists a known region in $g[u, v]$ with pixels having nearly zero value and relates the collected Fourier data to this constraint. FMCA expresses this relationship as a set of linear equations and solves for the unknown phase errors directly.

Let $\mathrm{G}_c[k, l]$ be Cartesian-grid Fourier data linearly interpolated from the collected polar Fourier data, $\mathrm{G}[m, n]$ (assuming $\mathrm{G}[m, n]$ is shifted downward to baseband), where $1 \leq k \leq K, 1 \leq l \leq L$ and K, L denotes the extent of coverage of the rectangular Fourier space region to which we wish to interpolate. Using linear interpolation, the Cartesian grid data $\mathrm{G}_c[k, l]$ can be expressed as.

$$\mathrm{G}_c[k, l] = \sum_{m,n} \alpha(k, l, m, n)\mathrm{G}[m, n], \tag{2.11}$$

where $\alpha(k, l, m, n)$ are the interpolation coefficients. In this chapter, for simplicity, we use nearest-neighbor interpolation, which means that $\alpha(k, l, m, n) = 1$ when $\mathrm{G}[m, n]$ is closest to $\mathrm{G}_c[k, l]$ and 0 otherwise. However, in principle, any linear interpolation can be used. The image $g[u, v]$ is reconstructed by using an inverse discrete Fourier transform,

$$g[u, v] = \frac{1}{KL} \sum_{k,l} \mathrm{G}_c[k, l] e^{j2\pi\left(\frac{uk}{K} + \frac{vl}{L}\right)}. \tag{2.12}$$

The region of terrain that is imaged in SAR depends on the antenna pattern. Little energy is collected from outside the antenna main beam. By oversampling in both the range and cross-range directions, in principle we can produce a SAR image that has low-value pixels at the border of the image. However, the unknown phase errors introduced to the collected Fourier data will have the effect of convolving the focused image $g[u, v]$ with an unknown 2-D blurring kernel, so that the energy of $g[u, v]$ may be spread across the whole image plane. Therefore, the image constructed from the phase corrupted data $\tilde{\mathrm{G}}_c[k, l]$ may not contain a low-return region. FMCA compensates the phase errors by forcing the low-return region in the border of the reconstructed image to have nearly zero value. More generally, FMCA applies even if the region known to have low-return is not in the border of the image.

Let $g[u_r, v_r],\ r = 1, 2, \ldots, R$ be the set of pixels that are nearly zero. From Eqn. (3.15), (3.23) and (2.12) we have

$$g[u_r, v_r] = \frac{1}{KL} \sum_{k,l} \sum_{m,n} \alpha(k, l, m, n) \tilde{\mathrm{G}}[m, n]\ e^{-j\phi(m)} e^{j2\pi\left(\frac{u_r k}{K} + \frac{v_r l}{L}\right)} \approx 0 \tag{2.13}$$

In matrix notation, (2.13) can be written as

$$\mathbf{A}\ e^{-j\boldsymbol{\phi}} \approx 0, \tag{2.14}$$

where $\boldsymbol{\phi} = [\phi(1)\ \phi(1) \ldots \phi(M)]^T$ and $\mathbf{A}$ is an R by M matrix with elements

$$\mathrm{A}[m, r] = \frac{1}{KL} \sum_{k,l} \left(\sum_{n} \alpha(k, l, m, n) \tilde{\mathrm{G}}[m, n] \right) e^{j2\pi\left(\frac{u_r k}{K} + \frac{v_r l}{L}\right)} \tag{2.15}$$

where $1 \leq r \leq R, 1 \leq m \leq M$.

Assuming that the values of $g[u_r, v_r]$'s are zero, $e^{-j\boldsymbol{\phi}}$ must be in the null space of $\mathbf{A}$. By carefully selecting the sampling rate and having a sufficiently large low-return region ($R > M - 1$), we can ensure that A has rank $M - 1$ and the phase correction vector $e^{-j\hat{\boldsymbol{\phi}}}$ can be obtained by determining the vector $\mathbf{f}$ spanning the null space of $\mathbf{A}$,

$$\mathbf{f} = \beta e^{-j\boldsymbol{\phi}} \in \mathcal{N}(\mathbf{A}), \tag{2.16}$$

where β is an arbitrary complex constant. We retain only the angular part of $\mathbf{f}$ as our phase estimate

$$\hat{\boldsymbol{\phi}} = -\angle(\mathbf{f}). \tag{2.17}$$

However, when $|g[u_r, v_r]| \neq 0$, due to additive noise or bright reflectors in the antenna sidelobes, we observe that $\mathbf{A}$ has full column rank and we cannot determine $e^{-j\boldsymbol{\phi}}$ using the null space of $\mathbf{A}$. Although $g[u_r, v_r]$ may not have a region that is truly zero, we would like the phase estimate to produce a restored image with minimum energy in the low-return region. In other words, we wish to have a phase estimate $e^{-j\hat{\boldsymbol{\phi}}_{min}}$ such that $\hat{\boldsymbol{\phi}}_{min}$ satisfies

$$\hat{\boldsymbol{\phi}}_{min} = \underset{\mathbf{a}\in\mathbb{R}^M}{\operatorname{argmin}} \|\mathbf{A}\ e^{-j\mathbf{a}}\|_2. \tag{2.18}$$

Equation (2.18) is very challenging to solve, and therefore we adopt the following approximation

$$e^{-j\hat{\boldsymbol{\phi}}_{min}} \approx \mathbf{v} = \underset{\mathbf{a}\in\mathbb{C}^M, \|\mathbf{a}\|_2=1}{\operatorname{argmin}} \|\mathbf{A}\ \mathbf{a}\|_2. \tag{2.19}$$

The solution to the above problem is given by the right singular vector that corresponds to the smallest singular value of $\mathbf{A}$. To ensure that $\mathbf{v}$ has the form of $e^{-j\boldsymbol{\phi}}$ in Eqn. (2.14), the FMCA phase estimator $\hat{\boldsymbol{\phi}}_{FMCA}$ keeps only the angular part of $\mathbf{v}$, resulting in

$$\hat{\boldsymbol{\phi}}_{FMCA} = -\angle(\mathbf{v}). \tag{2.20}$$

2.3 Comparison with MCA

Since FMCA and MCA are designed for the same imaging scenario, it is interesting to compare these autofocus approaches. We have the following result.

Theorem 2.1. As the range of viewing angles approaches zero, MCA is equivalent to FMCA.

Proof. When the SAR operates over exceedingly small viewing angles, the collected polar formatted Fourier data $\tilde{\mathrm{G}}[m,n]$ correspond approximately to a Cartesian format $\tilde{\mathrm{G}}_c[k,l]$, and $\tilde{\mathrm{G}}_c[k,l] = \tilde{\mathrm{G}}[m,n]$ for $k = n, l = m$. The polar-to-Cartesian interpolation can be ignored and the elements of FMCA matrix $\mathbf{A}$ degenerate to

$$\mathrm{A}[m,r] = \frac{1}{MN} \sum_n \tilde{\mathrm{G}}[m,n] e^{j2\pi\left(\frac{u_r m}{M} + \frac{v_r n}{N}\right)}. \tag{2.21}$$

Without loss of generality, we assume $M = N$. Let $\mathbf{W}_M$ be the M point DFT matrix ($\mathbf{W}_M[i,j] \triangleq \frac{1}{\sqrt{M}} e^{-j2\pi(i-1)(j-1)/M}, 1 \leq i,j \leq M$), $\mathbf{W}_M$ is unitary (i.e., $\mathbf{W}_M \mathbf{W}_M^H = I$). We can make the following observation for the FMCA problem (2.14):

$$0 \approx \mathbf{A}\; e^{-j\boldsymbol{\phi}} = \mathbf{A}\; \mathbf{W}_M \mathbf{W}_M^H\; e^{-j\boldsymbol{\phi}} = \mathbf{B}\mathbf{e}, \tag{2.22}$$

where $\mathbf{e} = \mathbf{W}_M\; e^{-j\boldsymbol{\phi}} = \mathrm{DFT}^{-1}(e^{-j\boldsymbol{\phi}})$ and $\mathbf{B} = \mathbf{A}\; \mathbf{W}_M$ is an R by M matrix with elements

$$\mathrm{B}[m,r] = \tilde{g}[\mathrm{mod}(u_r - m, M), v_r]. \tag{2.23}$$

Here $\mathrm{mod}(u_r - m, M)$ denotes $(u_r - m)$ modulo M. Comparing Eqn. (2.23) with (2.9), we can see that the elements of $\mathbf{B}$ are constructed from the rows of $\tilde{g}$ that correspond to the low-return constraint. Since the MCA framework can be stated as solving $0 \approx \mathbf{B}\mathbf{e}$ with constraints on the structure of $\mathbf{e}$ as shown in Section 2.1 [29], we have the desired result. $\square$

Note that MCA also solves $0 \approx \mathbf{B}\mathbf{e}$ by using the following approximation

$$\hat{\mathbf{e}} = \underset{\mathbf{a} \in \mathbb{C}^M, \|\mathbf{a}\|_2 = 1}{\mathrm{argmin}} \|\mathbf{B}\; \mathbf{a}\|_2 \tag{2.24}$$

and produces the phase estimates $\hat{\boldsymbol{\phi}}_{MCA}$ by

$$\hat{\boldsymbol{\phi}}_{MCA} = -\angle(\mathrm{DFT}(\hat{\mathbf{e}})). \tag{2.25}$$

Next, we study the restoration capability of FMCA. FMCA inherits multiple properties from MCA, which we will briefly list here. The derivations are similar to those of MCA [29].

Property 1 (Equivalence of singular values) *Let* $\mathbf{A}$ *be the FMCA data matrix formed from uncorrupted data and* $\tilde{\mathbf{A}}$ *be the FMCA data matrix formed from corrupted data. Then the magnitudes of the singular values of* $\mathbf{A}$ *and* $\tilde{\mathbf{A}}$ *are identical.*

Property 1 is easy to see, since from Eqn. (2.15) we have $\tilde{\mathbf{A}} = \mathbf{A}\text{Diag}(e^{j\boldsymbol{\phi}})$. Observe that

$$\tilde{\mathbf{A}}^H\tilde{\mathbf{A}} = \mathbf{A}^H\text{Diag}(e^{j\boldsymbol{\phi}})^H\text{Diag}(e^{j\boldsymbol{\phi}})\mathbf{A} = \mathbf{A}^H\mathbf{A}, \tag{2.26}$$

and thus $\mathbf{A}$ and $\tilde{\mathbf{A}}$ have singular values with the same magnitudes.

Property 2 (Equivalence of restoration) *Suppose that* $\mathbf{A}$ *(or equivalently* $\tilde{\mathbf{A}}$*) has a distinct smallest absolute singular value. Then applying the FMCA correction filter* $\mathbf{v}$ *and* $\tilde{\mathbf{v}}$ *to* $\mathbf{A}$ *and* $\tilde{\mathbf{A}}$*, respectively, produces the same magnitude restoration where* $\mathbf{v}$ *and* $\tilde{\mathbf{v}}$ *are the minimum right singular vector of* $\mathbf{A}$ *and* $\tilde{\mathbf{A}}$ *respectively, i.e.,*

$$|\mathbf{A}\ \mathbf{v}| = |\tilde{\mathbf{A}}\ \tilde{\mathbf{v}}|. \tag{2.27}$$

To show Property 2, first use Property 1 and the assumption that the smallest absolute singular value of $\mathbf{A}$ and $\tilde{\mathbf{A}}$ is distinct. We have

$$|\tilde{\mathbf{A}}\tilde{\mathbf{v}}| = |\mathbf{A}\text{Diag}(e^{j\boldsymbol{\phi}})\tilde{\mathbf{v}}|. \tag{2.28}$$

Thus, $\mathbf{v} = \beta\text{Diag}(e^{j\boldsymbol{\phi}})\tilde{\mathbf{v}}$, where β is a complex scalar with $|\beta| = 1$. Then we observe that

$$|\tilde{\mathbf{A}}\tilde{\mathbf{v}}| = |\beta^{-1}\mathbf{A}\text{Diag}(e^{j\boldsymbol{\phi}})\text{Diag}(e^{j\boldsymbol{\phi}})^H\mathbf{v}| = |\mathbf{A}\mathbf{v}|, \tag{2.29}$$

and we have the desired result.

Property 2 shows that applying FMCA to the perfectly-focused image or any defocused image produces the same restored image (we are only interested in displaying the image magnitude). In other words, the restoration capability of FMCA does not depend on the phase error function, unlike existing autofocus algorithms where the performance tends to degrade when the phase errors are large and rapidly-varying. However, this result does not imply anything about the quality of the restoration.

2.4 Simulation Results

In this section, we present simulation results for FMCA image restoration for both monostatic and bistatic SAR scenarios. We compare the performance of FMCA with both MCA and PGA. An antenna pattern simulated by the main lobe of a 2-D sinc squared function was applied to the SAR images so that the border of the image had nearly zero pixel magnitudes. The phase errors were independent and identically distributed (*i.i.d.*) across the cross-range coordinate and uniformly distributed between $-\pi$ and π. This phase error model is the worst case scenario and produces the most severe defocusing effects.

2.4.1 Monostatic SAR scenario

In the monostatic SAR scenario, we studied how the range of look angles affects the performance of various autofocus algorithms. To evaluate the performance of reconstruction, we first tested the three autofocus algorithms with images of randomly scattered point targets. The perfectly focused image and the phase corrupted image for a 0.01 degree range of look angles are shown in Fig. 2.2(a) and (b), respectively. The images restored by FMCA, MCA and PGA are shown in Fig. 2.5. In this case, the locations of the collected Fourier data closely resemble a Cartesian grid and all of the algorithms could successfully reconstruct the image. The cross-section of the point

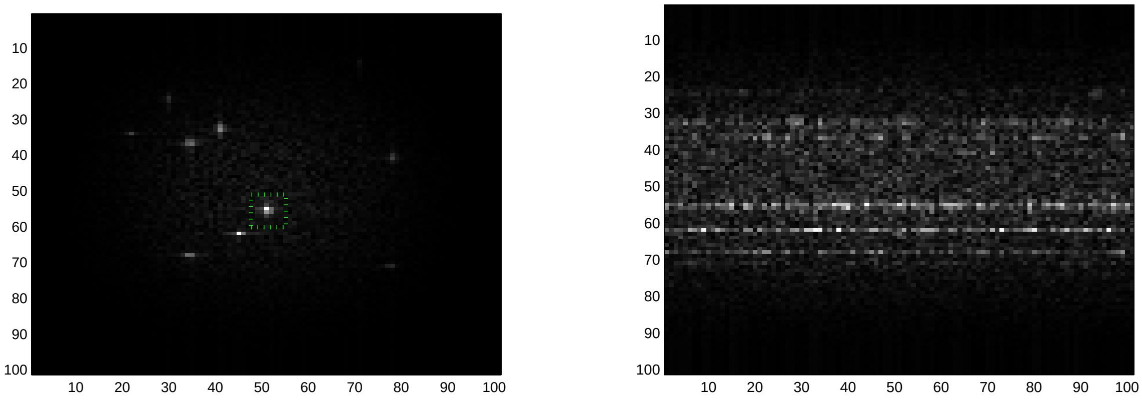

(a)

(b)

Figure 2.2: Simple point target image for 0.01 degree look angle: (a) perfectly-focused image with 2-D sinc-squared antenna pattern applied, the border of the image is assumed to have low return (the cross-section of the point target inside the dotted box is plotted in Fig. 2.8); (b) defocused image produced after applying a white phase error function.

target inside the dotted box in Fig. 2.2(a) is plotted in Fig. 2.8(a). We can see that all three algorithms successfully reconstructed the point target. Figure 2.6 shows the image restoration results for the same point target image but with a 0.1 degree range of look angles. We can see that MCA starts to break down in this case as it depends heavily on the assumption that the collected Fourier data lie on a Cartesian grid. Note that PGA still provides a good reconstruction. The point target cross-section comparison is plotted in Fig. 2.8(b). Note that MCA has more energy diffused outside the point target center. Figure 2.7 shows the image restoration results for a 1 degree range of look angles. The point target cross-section comparison is plotted in Fig. 2.8(c). In this case, the locus of the collected Fourier data can no longer be approximated by a Cartesian grid, and MCA breaks down completely. The performance degradation of PGA is also apparent as the range of look angles becomes wider. The performance of FMCA remains excellent as the range of look angles increases.

Next, we show the image restoration results for a more challenging scenario. A SAR image from Sandia National Laboratory was used as a proxy for the magnitude of a

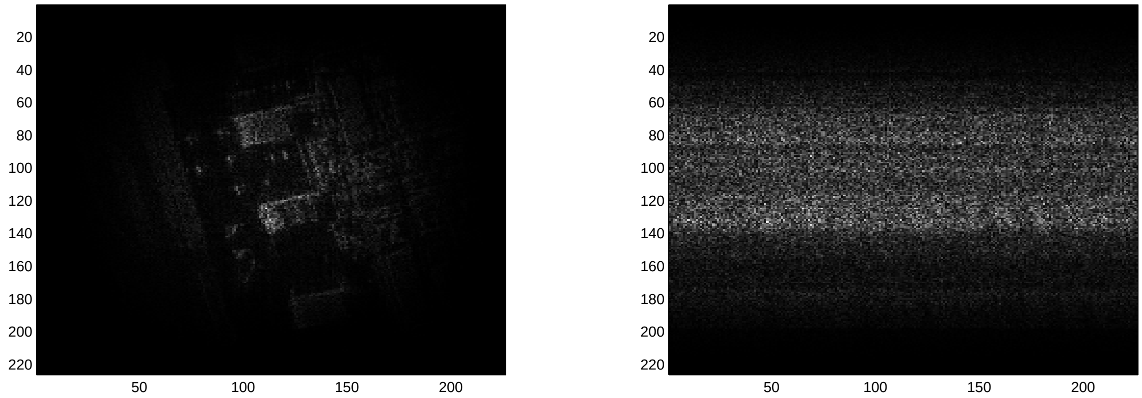

(a) (b)

Figure 2.3: Real SAR image for 0.005 degree look angle: (a) perfectly-focused image with 2-D sinc-squared antenna pattern applied, the border of the image is assumed to have low return; (b) defocused image produced by applying a white phase error function.

SAR scene. Again, we compare FMCA with MCA and PGA under different ranges of look angles. The perfectly focused image and the phase corrupted image for a 0.005 degree range of look angles is shown in Fig. 2.3 and images restored by FMCA, MCA and PGA are shown in Fig. 2.9. Due to the complexity of the real SAR image and by considering a white phase error function, we observe some artifacts in the PGA restoration, but otherwise PGA still produced a recognizable image. MCA performed well in this small look angle case. Figure 2.10 shows the restoration results for a 0.05 degree look angle and Fig. 2.11 shows the restoration results for a 0.5 degree look angle. From these simulations, we observe that while MCA slightly outperformed PGA in the the smallest look angle case in Fig. 2.9, MCA breaks down more quickly when the range of look angles is wider. The performance of FMCA is not affected by the range of look angles. FMCA continued to perform well for even much wider look angles as seen in Fig. 2.12.

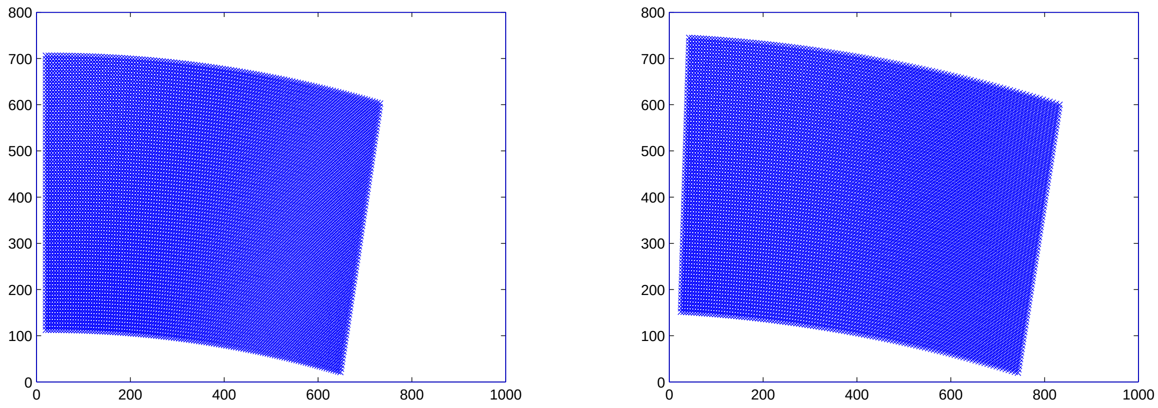

(a) (b)

Figure 2.4: Collected Fourier data pattern for bistatic SAR: (a) example for a stationary transmitter and a moving receiver; (b) example for a moving transmitter and a moving receiver.

2.4.2 Bistatic SAR scenario

Here, we demonstrate the restoration capability of FMCA for bistatic SAR. We experimented with two bistatic SAR scenarios. Scenario 1 assumed a stationary transmitter and a moving receiver; scenario 2 assumed a moving transmitter and a moving receiver with straight-line perpendicular motions. The collected Fourier data pattern for both scenarios is shown in Fig. 2.4. Figure 2.13 shows the autofocus results for scenario 1. Figure 2.14 shows the autofocus results for scenario 2. Notice that FMCA successfully produced a focused image in both scenarios. (Neither MCA nor PGA can be applied directly to the bistatic scenario.)

2.5 Chapter Summary

In this chapter, we developed a new autofocus algorithm, termed Fourier-domain multichannel autofocus (FMCA), which can accommodate both wide-angle monostatic SAR and bistatic SAR scenarios. FMCA was derived within a linear algebraic framework, allowing the phase errors to be corrected in a noniterative fashion. FMCA requires prior knowledge that a region in the underlying scene has zero or nearly-zero pixel values (low-return region). In practice, a low-return region exists in the sidelobes of the antenna pattern. The previously developed MCA approach can be viewed as a special case of FMCA when operating at very small viewing angles. We presented computer simulations to demonstrate the performance of FMCA compared with MCA and PGA for various ranges of look angles, and also considered bistatic SAR scenarios.

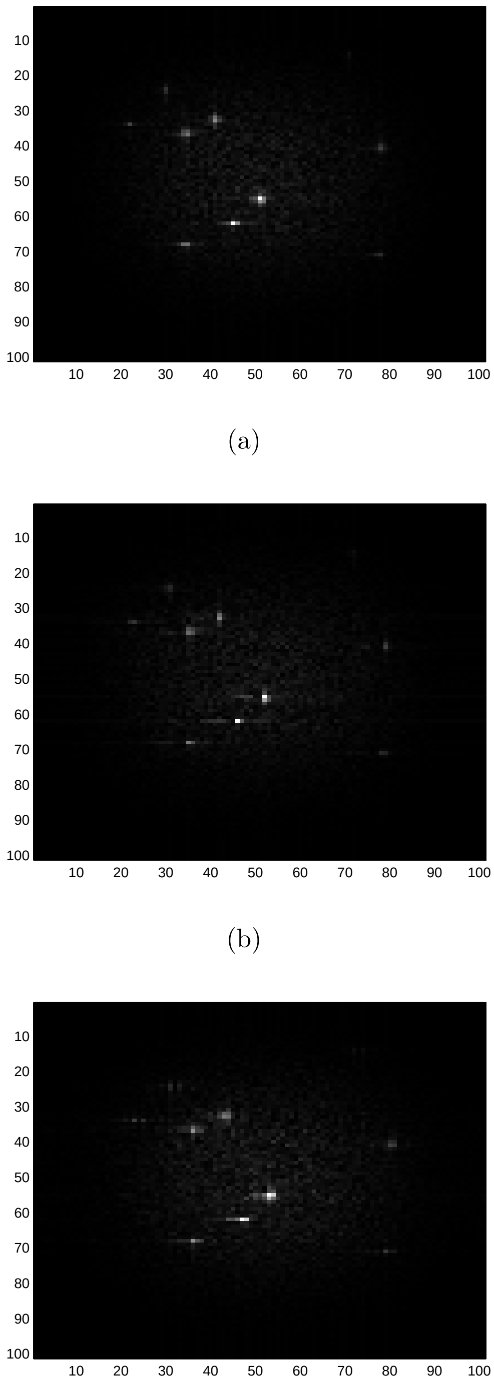

(a)

(b)

(c)

Figure 2.5: Autofocus for the point target image with a 0.01 degree look angle: (a) image restored by FMCA; (b) image restored by MCA; (c) image restored by PGA.

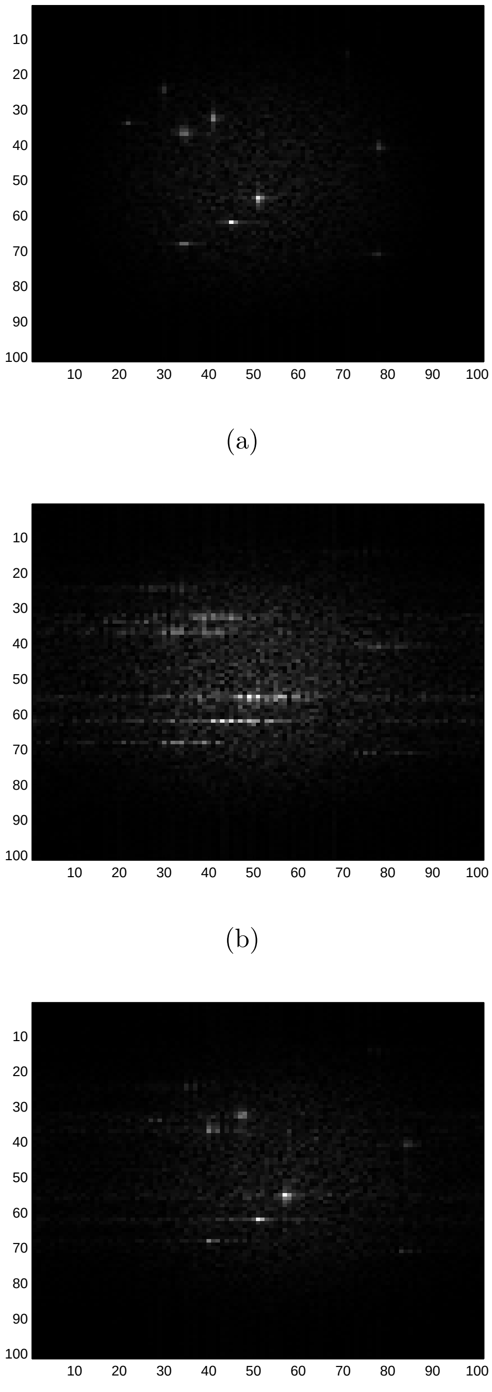

(a)

(b)

(c)

Figure 2.6: Autofocus for the point target image with a 0.1 degree look angle: (a) image restored by FMCA; (b) image restored by MCA; (c) image restored by PGA.

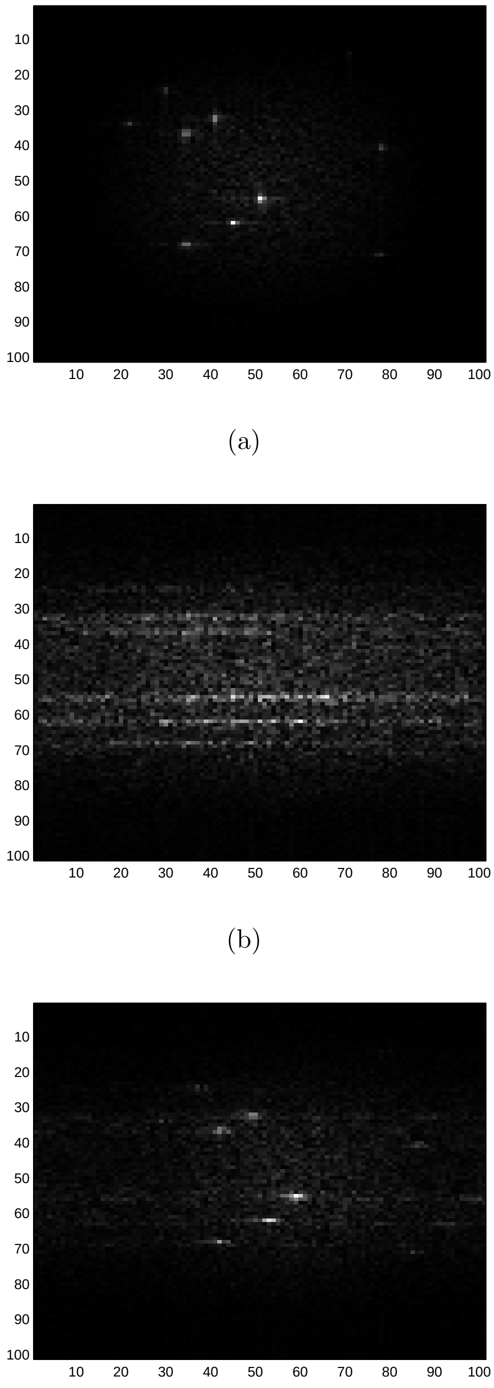

(a)

(b)

(c)

Figure 2.7: Autofocus for the point target image with a 1 degree look angle: (a) image restored by FMCA; (b) image restored by MCA; (c) image restored by PGA.

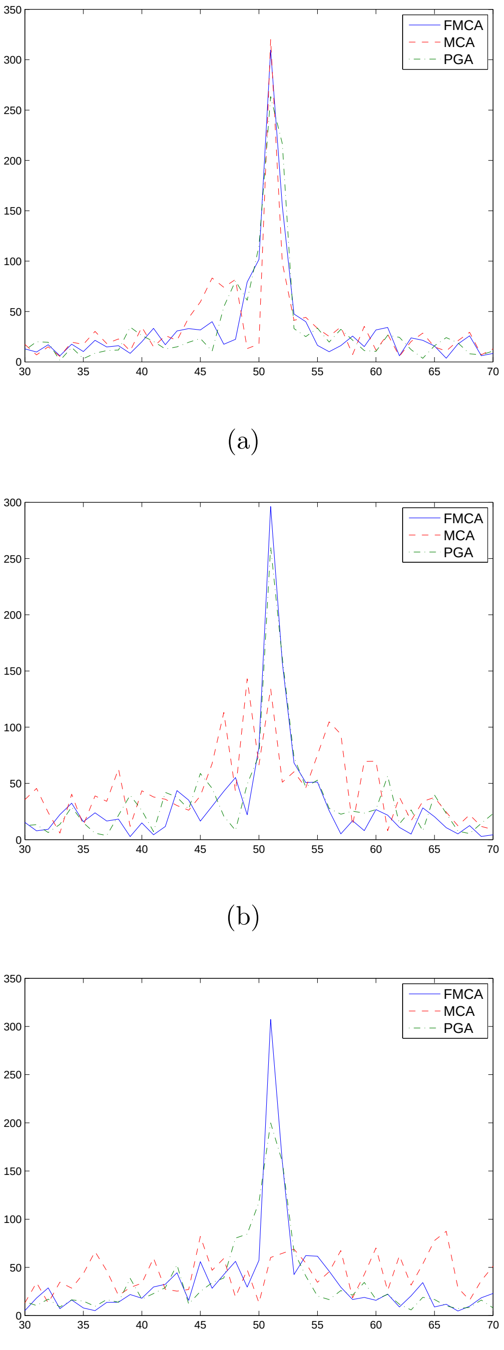

(a)

(b)

(c)

Figure 2.8: Comparison of the point-target cross-sections: (a) for 0.01 degree look angle; (b) for 0.1 degree look angle; (c) for 1 degree look angle.

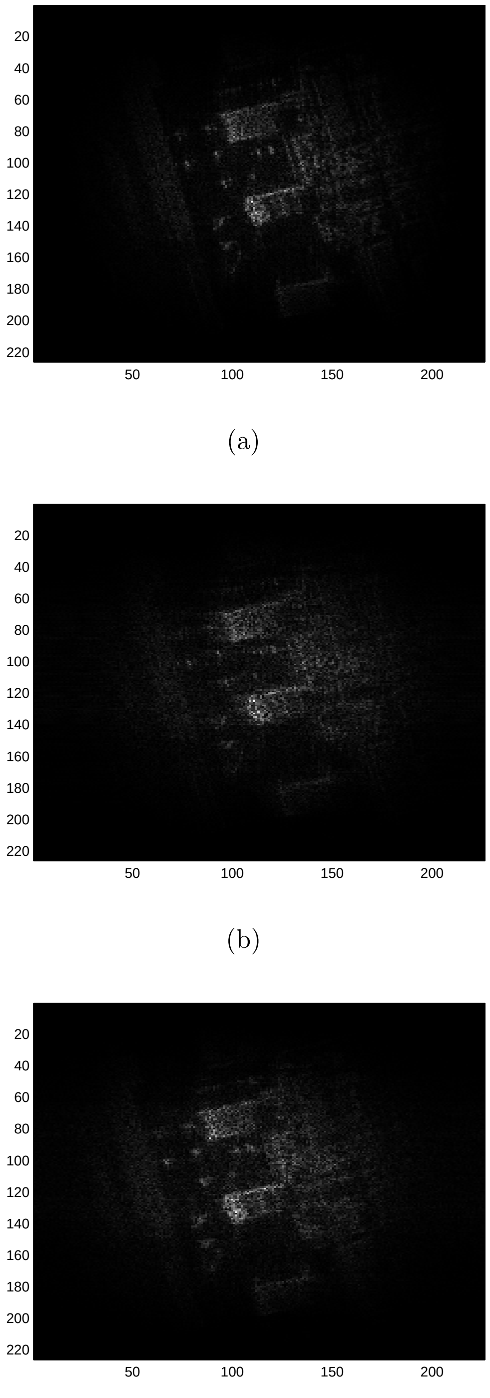

(a)

(b)

(c)

Figure 2.9: Autofocus for the real SAR image with a 0.005 degree look angle: (a) image restored by FMCA; (b) image restored by MCA; (c) image restored by PGA.

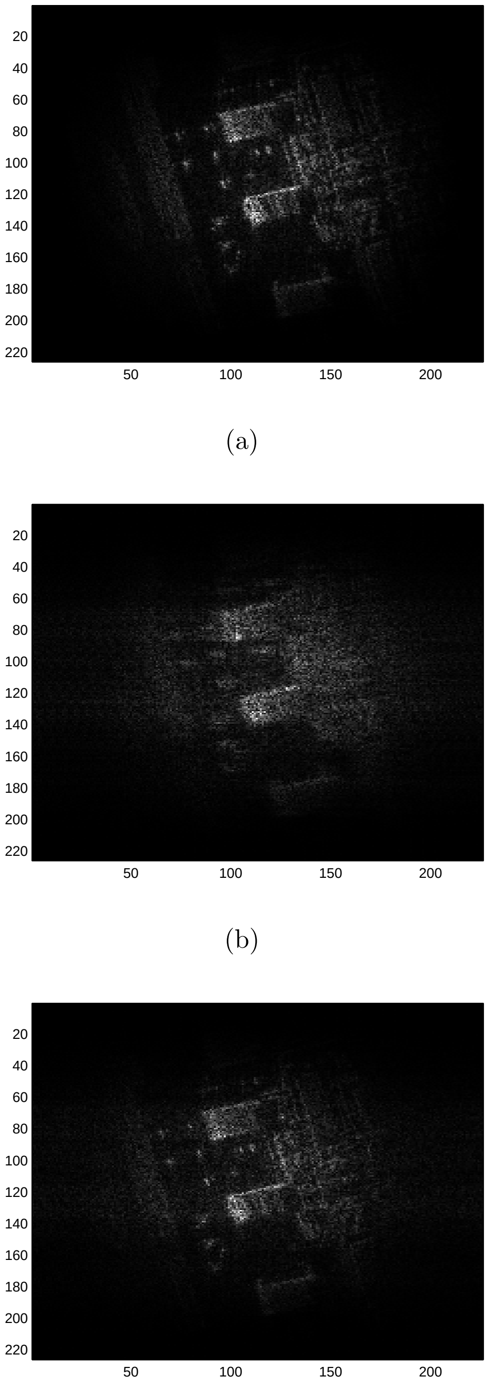

(a)

(b)

(c)

Figure 2.10: Autofocus for the real SAR image with a 0.05 degree look angle: (a) image restored by FMCA; (b) image restored by MCA; (c) image restored by PGA.

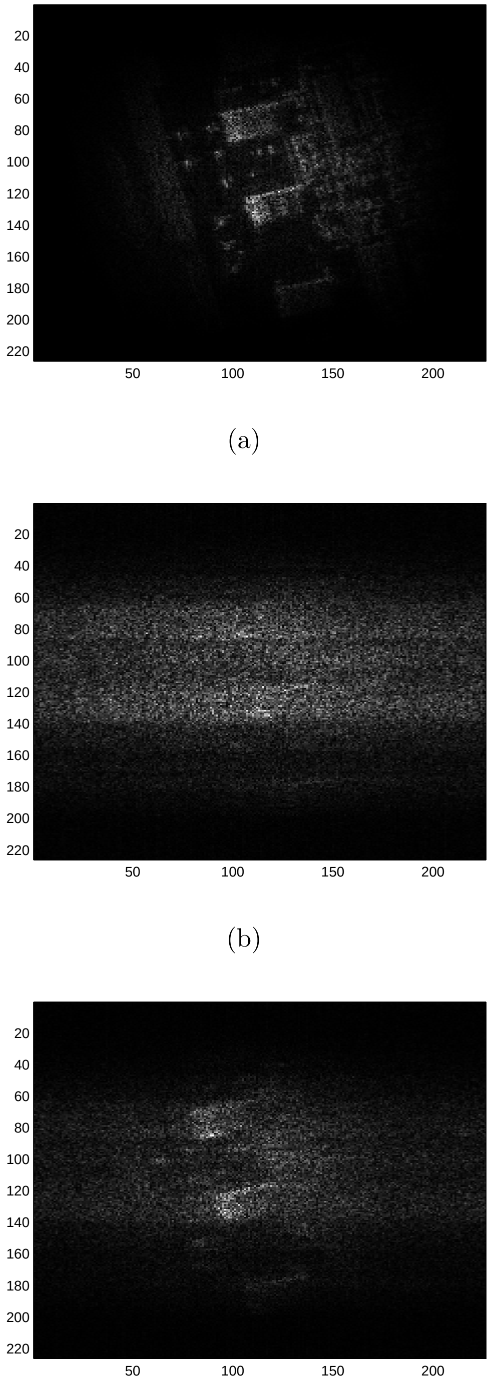

(a)

(b)

(c)

Figure 2.11: Autofocus for the real SAR image with a 0.5 degree look angle: (a) image restored by FMCA; (b) image restored by MCA; (c) image restored by PGA.

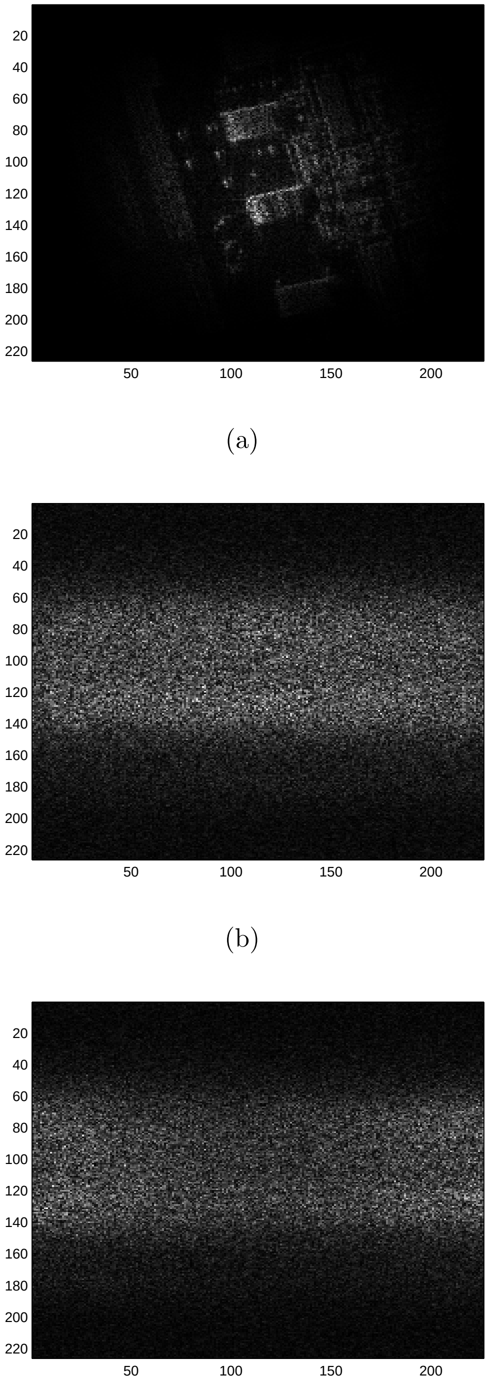

(a)

(b)

(c)

Figure 2.12: Autofocus for the real SAR image with a 5 degree look angle: (a) image restored by FMCA; (b) image restored by MCA; (c) image restored by PGA.

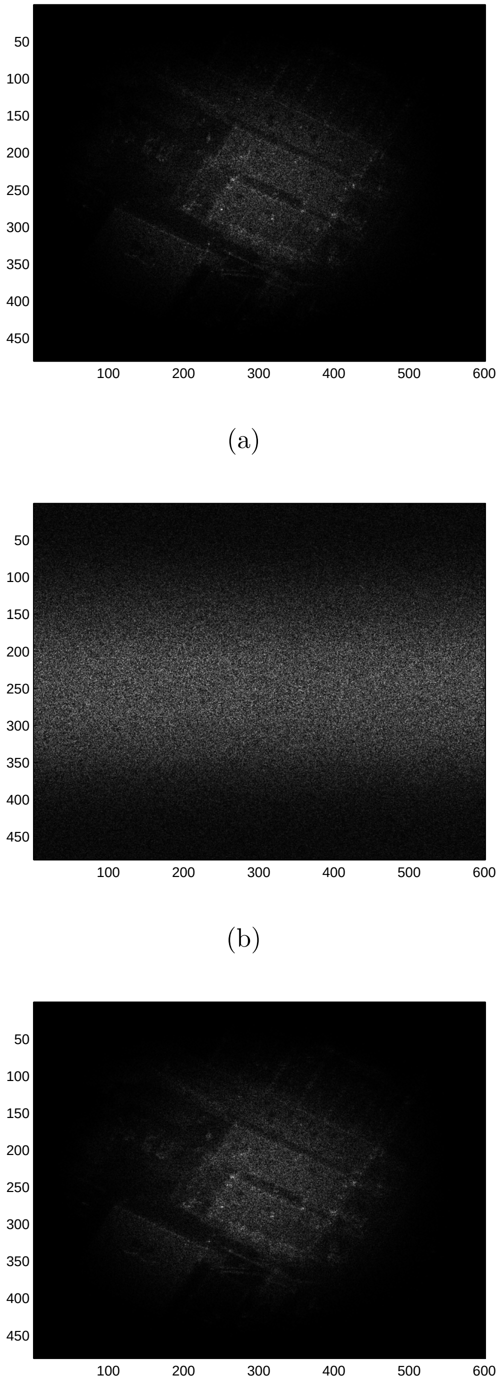

(a)

(b)

(c)

Figure 2.13: Bistatic SAR autofocus for a stationary transmitter and a moving receiver: (a) perfectly-focused image; (b) defocused image produced by applying a white phase error function; (c) image restored by FMCA.

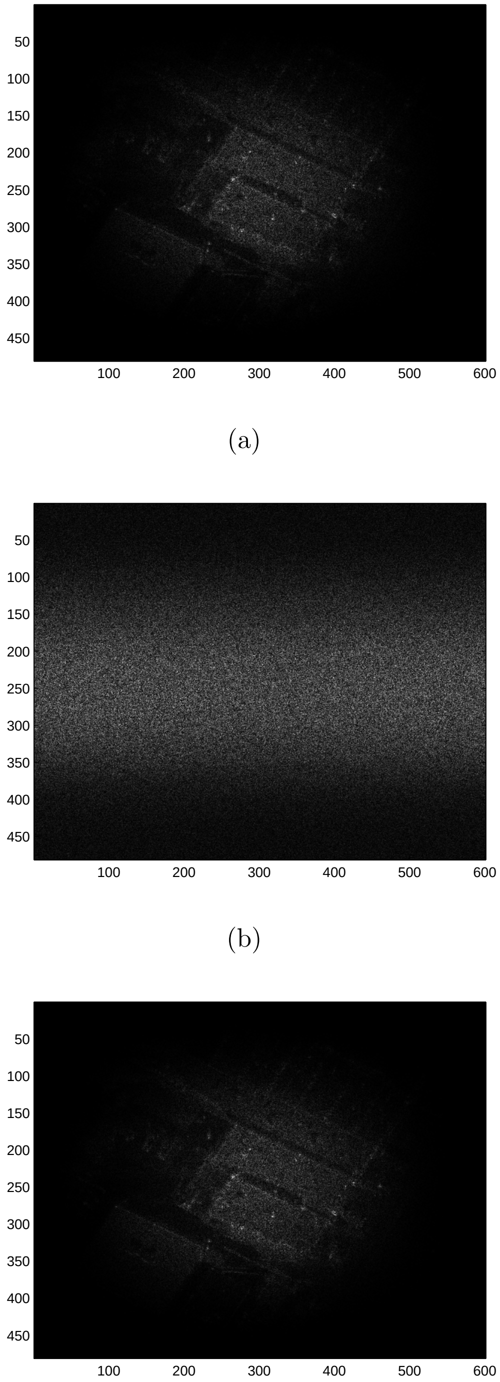

(a)

(b)

(c)

Figure 2.14: Bistatic SAR autofocus for a moving transmitter and a moving receiver: (a) perfectly-focused image; (b) defocused image produced by applying a white phase error function; (c) image restored by FMCA.

CHAPTER 3

SAR Autofocus via Semidefinite Relaxation

At the core of the three state-of-the-art autofocus algorithms, PGA, MCA and FMCA, is the solution to a Constant Modulus Quadratic Program (CMQP) of the following form:

$$\begin{aligned} \min_{\mathbf{x}\in\mathbb{C}^M} \quad & \mathbf{x}^H\mathbf{Q}\mathbf{x} \\ s.t \quad & |\mathbf{x}_i| = 1 \;\; , i = 1, \ldots, M. \end{aligned} \tag{3.1}$$

This problem is known to be NP-hard; thus, the best we can hope for is an approximation. All three algorithms use eigenvalue relaxation to approximate the original CMQP. In this chapter, we propose an alternative approximation based on modern conic optimization known as semidefinite relaxation (SDR). SDR offers a compromise where it provides a more accurate approximation to the CMQP at the cost of complicating the underlying optimization problem.

SDR has recently been applied to many problems in communications and signal processing [33, 34, 35, 36, 37, 38, 39, 40, 41, 42, 43]. Basically, SDR approximates a quadratic problem with a convex optimization problem by first lifting the problem to a higher dimension and then relaxing the nonconvex constraints. To the best of our knowledge, this is the first time that SDR has been applied to the problem of SAR autofocus. This problem formulation is similar to the discrete symbol detection problem in communication systems, which has recently gained considerable attention [34, 35]. However, the feasible set is a continuous constant modulus set as described in

Eqn. (3.1) above, and is not discrete. Some theoretical results on the performance of SDR for the continuous symbol case are given in [44, 45, 46]. Our simulation results suggest that, combined with PGA, MCA and FMCA, SDR is a promising autofocus technique. We note that currently solving SDR requires polynomial time and may not be amenable to online processing. Nonetheless, there may be crucial situations where it is imperative that an image be focused as well as possible, using computationally intensive offline processing.

The organization of this chapter is as follows. We will briefly review the concept of SDR in Section 3.1. Section 3.2 presents the problem formulation for PGA, MCA and FMCA and also discusses how we can improve these existing techniques by using SDR. Simulation results are given in Section 3.3. Finally, we summarize this chapter in Section 3.4.

3.1 Review of Semidefinite Relaxation

In this section, we briefly review the topic of semidefinite programming (SDP) and its application to approximate nonconvex CMQP problems. More details on SDP can be found in [47, 48]. The SDR approximation is described in [36].

3.1.1 Semidefinite Programming

In recent years, there has been considerable progress and development of efficient algorithms for solving a variety of optimization problems. In particular, significant attention has been devoted to SDP, a generalization of classical linear programming to include linear matrix inequalities. The standard form of an SDP is [47, 48]:

$$\begin{aligned} \min \quad & \operatorname{tr}(\mathbf{Q}\mathbf{X}) \\ \text{s. t.} \quad & \operatorname{tr}(\mathbf{A}_i\mathbf{X}) = b_i \ \ , i = 1, \ldots, M \\ & \mathbf{X} \succeq 0, \end{aligned} \tag{3.2}$$

where $\mathbf{Q}$, $\mathbf{A}_i,\ i = 1, \ldots, M$ are the data parameters and $\mathbf{X}$ is the optimization variable. SDP belongs to a class of problems knowns as conic optimization problems whose global optimum can be efficiently found using standard algorithms.

The most promising technique at present to solve small-to-medium-scale SDP is the interior-point (IP) method. There exist off-the-shelf software packages based on IP for solving general SDP [49]. In many problems, it is more computationally efficient to use a customized IP method tailored to the problem of interest (e.g., [35]). Unfortunately, IP methods are not appropriate for large-scale problems, such as the ones addressed in this thesis, because the memory and computational costs of even one IP iteration are too high. In such scenarios, first-order methods, with simple iterations, must be utilized [50, 51]. A classical method is the spectral bundle method developed in [52, 53]. The standard SDP involves real parameters and variables, but can be easily generalized to account for complex values through a change of variables (e.g., [35]), or specifically tailored complex optimization methods.

3.1.2 Constant Modulus Quadratic Programming

One promising application of SDP is in the approximation of the complex Constant Modulus Quadratic Programming (CMQP) problem [36]. In particular, CMQP can be written as

$$(CMQP) \qquad \begin{aligned} \min_{\mathbf{x} \in \mathbb{C}^M} \quad & \mathbf{x}^H \mathbf{Q} \mathbf{x} \\ s.t \quad & |\mathbf{x}_i| = 1 \ \ , i = 1, \ldots, M. \end{aligned} \tag{3.3}$$

It is known that CMQP is NP-hard [45, 54], and thus, for large problem sizes, the best we can hope for is an approximation algorithm.

A natural approximation to CMQP is eigenvalue relaxation (EVR), which can be written as

$$\begin{aligned} (EVR) \qquad & \min_{\mathbf{x}\in\mathbb{C}^M} \quad \mathbf{x}^H\mathbf{Q}\mathbf{x} \\ & s.t \quad \mathbf{x}^H\mathbf{x} = M. \end{aligned} \tag{3.4}$$

The main advantage of EVR is that the problem (EVR) has a simple closed-form solution. Using the variational characterization of singular values, the optimal solution to EVR is the right singular vector of $\mathbf{Q}$ that corresponds to the minimum singular value. Clearly, if this eigenvector satisfies the original $(CMQP)$ constraints, then it is the optimal solution to $(CMQP)$ as well and the relaxation is tight. Otherwise, we can obtain an approximate solution $\tilde{\mathbf{x}}$ by rounding the minimum right singular vector, denoted by $\mathbf{v}$, as

$$\tilde{\mathbf{x}} = e^{j\angle(\mathbf{v})}. \tag{3.5}$$

Recently, a more advanced relaxation scheme, SDR, has been proposed. This relaxation can be derived through Lagrange duality or via a lift-and-relax argument (see exercise 5.39 in [47]). For completeness, we review the latter derivation. For this purpose, we first lift the solution space of $(CMQP)$ from vectors to positive semidefinite matrices to obtain

$$\begin{aligned} (CMQP') \qquad & \min_{\mathbf{X}\in\mathbb{C}^{M\times M}} \quad \mathrm{tr}(\mathbf{Q}\mathbf{X}) \\ & s.t \quad \mathbf{X}_{ii} = 1 \ \ , i = 1, \ldots, M \\ & \qquad\quad \mathbf{X} \succeq 0 \\ & \qquad\quad \mathrm{rank}(\mathbf{X}) = 1. \end{aligned} \tag{3.6}$$

Problems $(CMQP)$ and $(CMQP')$ are equivalent since the solution to $(CMQP')$, $\mathbf{X}$, can be expressed as $\mathbf{X} = \mathbf{x}\mathbf{x}^H$ with $|\mathbf{x}_i| = 1,\ i = 1, \ldots, M$. This follows because $\mathbf{X}$

is a rank-1 positive semidefinite matrix. Problem $(CMQP')$ has a nonconvex feasible set due to the rank-1 constraint and cannot be solved efficiently. Instead, we relax the feasible set of $(CMQP')$ to obtain the revised problem (SDR):

$$\begin{aligned} (SDR) \qquad & \min_{\mathbf{X}\in\mathbb{C}^{M\times M}} && \mathrm{tr}(\mathbf{QX}) \\ & s.t && \mathbf{X}_{ii} = 1 \ \ , i = 1, \ldots, M \\ & && \mathbf{X} \succeq 0. \end{aligned} \tag{3.7}$$

The above optimization problem is a relaxation of $(CMQP')$ and is a SDP with $\mathbf{A}_i = \mathrm{Diag}(\mathbf{e}_i)$ where $\mathbf{e}_i$ is the ith column of the identity matrix and $b_i = 1$ for all i. Thus, it can be efficiently solved as explained above.

Just like the EVR approach, the SDR must be complemented with an additional rounding scheme which uses its solution to generate an approximate feasible solution to $(CMQP)$. Let $\hat{\mathbf{X}}$ be the solution of (SDR). If $\mathrm{rank}(\hat{\mathbf{X}}) = 1$, then $\hat{\mathbf{X}} = \hat{\mathbf{x}}\hat{\mathbf{x}}^H$ is an optimal solution to $(CMQP)$, and the $(CMQP)$ problem is solved exactly. Otherwise, we can use $\hat{\mathbf{X}}$ to obtain a feasible approximate solution to $(CMQP)$. There are several methods we might employ. Here we focus on the randomization method [45]. Let $\hat{\mathbf{X}} = \hat{\mathbf{V}}\hat{\mathbf{V}}^H$ where $\hat{\mathbf{V}} = [\hat{\mathbf{v}}_1, \ldots, \hat{\mathbf{v}}_n]$ is a square-root factor of $\hat{\mathbf{X}}$. Because we relax the rank-1 constraint for $\hat{\mathbf{X}}$, n may be greater than 1. The randomization method generates M_{rand} complex gaussian vectors $\mathbf{u}_1, \mathbf{u}_2, \ldots, \mathbf{u}_{M_{rand}}$ that are independent with zero mean and covariance $\mathbf{I}$. It then computes $\mathbf{y}_i = \angle(\hat{\mathbf{V}}\mathbf{u}_i), i = 1, \ldots, M_{rand}$ and approximates a feasible solution, $\tilde{\mathbf{x}}$, to $(CMQP)$ as

$$\tilde{\mathbf{x}} = \underset{\mathbf{y}_1,\ldots,\mathbf{y}_{M_{rand}}}{\operatorname{argmin}} \ \mathbf{y}_i^H \mathbf{Q} \mathbf{y}_i. \tag{3.8}$$

The quality of the randomization method is discussed in [45].

3.1.3 Approximation Quality

We now briefly discuss the approximation quality of SDR. For this purpose, we first express (EVR) as the following equivalent SDP:

$$\begin{aligned}
(EV) \quad \min_{\mathbf{X}\in\mathbb{C}^{M\times M}} \quad & \mathrm{tr}(\mathbf{QX}) \\
s.t \quad & \mathrm{tr}(\mathbf{X}) = M \\
& \mathbf{X} \succeq 0 \\
& \mathrm{rank}(\mathbf{X}) = 1.
\end{aligned} \tag{3.9}$$

The comparison of SDR with EVR is summarized in the following theorem.

Theorem 3.1. *Let v_p^*, v_{sdr}^* and v_{ev}^* represents the optimal objective function values found for problems $(CMQP)$, (SDR) and (EV), respectively. Then*

$$v_p^* \geq v_{sdr}^* \geq v_{ev}^*. \tag{3.10}$$

Proof. First, we have shown that (SDR) is a relaxation of $(CMQP)$. This immediately gives us

$$v_p^* \geq v_{sdr}^*. \tag{3.11}$$

To show the second inequality, we note that (EV) is equivalent to the following problem:

$$\begin{aligned}
(EVR) \quad \min\nolimits_{\mathbf{X}\in\mathbb{C}^{M\times M}} \quad & \mathrm{tr}(\mathbf{QX}) \\
s.t \quad & \mathrm{tr}(\mathbf{X}) = M \\
& \mathbf{X} \succeq 0.
\end{aligned} \tag{3.12}$$

This is easily proved by showing that (EVR) is both a lower bound and an upper bound for (EV); thus it is tight. On the other hand, (EVR) can be viewed as a relaxation of

(SDR) by relaxing the $\mathbf{X}_{ii} = 1, \forall i$ constraint to $\mathrm{tr}(\mathbf{X}) = M$, and therefore

$$v^*_{sdr} \geq (EVR) = v^*_{ev}. \tag{3.13}$$

□

The above result shows that in terms of objective function value, SDR is a tighter relaxation than the natural EVR approach. However, it is important to emphasize that these results do not provide any guarantees on the quality of the solution itself.

Another result, due to So et al. [45], provides quality assurance for approximating a certain form of CMQP using SDR. Their result states that SDR plus randomization is a $\frac{\pi}{4}$-approximation algorithm for CMQP with $\mathbf{Q}$ in (3.3) that is negative semidefinite, i.e.,

$$v^*_p \geq \mathrm{E}[\mathbf{y}^H \mathbf{Q} \mathbf{y}] \geq \frac{\pi}{4} v^*_p, \tag{3.14}$$

where $\mathbf{y} = \angle(\hat{\mathbf{V}}\mathbf{u})$ and $\mathbf{u}$ is a normally distributed complex vector. Other theoretical studies are included in [55, 56, 57, 58].

3.2 Autofocus in Synthetic Aperture Radar

In this section we briefly review the formulation of the SAR autofocus problem solution using the PGA, MCA and FMCA approaches. The main message of this section is that all of these approaches lead to a CMQP problem. Previous work has approximated this problem using the EVR approach, and we propose to enhance the performance using the SDR technique described above.

As explained in the introduction chapter, a challenge in SAR imaging is that in order to correctly demodulate the returned signal, the two-way travel time of the transmitted signal must be known. In practice, due to unknown signal delays resulting from inaccurate range measurements or signal propagation effects, the polar-format Fourier data is contaminated with unknown phase errors that cause the reconstructed image to suffer distortion. The measurements at a given look angle suffer from the same unknown delay, and, under a narrow-band assumption, their unknown phase is constant. The delays, and their associated phases, change between different look angles. This results in the following error model

$$\tilde{\mathrm{G}}[m,n] = \mathrm{G}[m,n]\, e^{j\phi(m)} + \mathrm{W}[m,n], \tag{3.15}$$

where $\phi(m) \in \mathbb{R}, m = 1, 2, \ldots, M$ are unknown phases, and $\mathrm{W}[m,n]$ represents additive noise [5].

SAR reconstruction amounts to estimating the speckle image of $r(x,y)$ given the observations $\tilde{\mathbf{G}}$. Note that even without unknown phases, SAR reconstruction produces a speckle image that is similar to $|r(x,y)|$ but not identical. Moreover, as the additive noise increases, the quality of the speckle image degrades. The goal of SAR autofocus is to recover this speckle image (and not the true reflectivity function) in the presence of unknown phases. In this chapter, we will address this problem using a natural approach that first estimates the unknown phases, compensates for them and finally reconstructs the speckle image using classical techniques.

3.2.1 Phase Gradient Autofocus

PGA is the autofocus method most widely employed in practice. It is motivated by considering a scenario where each row of g contains only a single point reflector located at the center of the row. These reflectors are modeled as mutually *i.i.d.* zero-mean complex Gaussian random variables with variance σ_a^2, whereas the surrounding clutter is represented by *i.i.d.* zero-mean complex Gaussian random variables with variance σ_n^2. Let $\tilde{\mathbf{G}}_{rc}$ denote the range-compressed data, defined as $\tilde{\mathbf{G}}$ after undergoing a 1-D inverse Fourier transform in the n-dimension. Then, the rows of $\tilde{\mathbf{G}}_{rc}$ are *i.i.d.* realizations of a zero mean complex Gaussian vector with covariance

$$\sigma_a^2 \mathbf{x}\mathbf{x}^H + \sigma_n^2 \mathbf{I}, \tag{3.16}$$

where $\mathbf{x} = e^{j\boldsymbol{\phi}}$ is the phase vector ($\boldsymbol{\phi} = [\phi(1), \phi(2), \cdots, \phi(M)]^T$) which satisfies $|\mathbf{x}_i| = 1$ for $i = 1, 2, \cdots, M$.

PGA estimates $\mathbf{x}$ using a maximum likelihood approach. After simple algebraic manipulations, the problem reduces to

$$(P - PGA) \quad e^{j\hat{\boldsymbol{\phi}}_{PGA}} = \operatorname*{argmax}_{\mathbf{x}:|\mathbf{x}_i|=1} \mathbf{x}^H \tilde{\mathbf{G}}_{rc}^T (\tilde{\mathbf{G}}_{rc}^T)^H \mathbf{x}, \tag{3.17}$$

It is easy to see that $(P - PGA)$ is a CMQP with $\mathbf{Q} = -\tilde{\mathbf{G}}_{rc}^T (\tilde{\mathbf{G}}_{rc}^T)^H$. The original PGA technique [16] proposed to approximate Eqn. (3.17) using EVR (see Section 3.1). In the sequel, we will show that a better approximation can be obtained using our proposed SDR through an increase in computational cost.

For completeness, we note that the above scheme is not the full PGA algorithm, but is its core step. The full algorithm is an iterative technique where at each iteration the algorithm first preprocesses the obtained phase-compensated image so that it can be more accurately described by the assumed point target model. Then the phase errors are estimated by using Eqn. (3.17) and a refined image is constructed. For a complete description of the full PGA algorithm, see [5]. Also, note that in practice a simpler PGA algorithm is commonly used where the phase difference between adjacent pulses is estimated. This method can be shown to be a special case of the maximum-likelihood technique presented above.

3.2.2 Multichannel Autofocus

An alternative image model was recently proposed by Morrison et al. [29]. The autofocus algorithm they developed is called Multichannel Autofocus (MCA). The MCA reconstruction method assumes that there is a known region in the image that consists of nearly zero-valued pixels, i.e., $g[u_r, v_r] \approx 0$ for $r = 1, \cdots, R$. This prior knowledge can be inferred by using the low-return region of the antenna pattern [29]. Using this knowledge and "reverse engineering," MCA searches for the phases that will result in a reconstructed image with

$$|\hat{g}[u_r, v_r]| \approx 0 \quad \text{for} \quad r = 1, \cdots, R. \tag{3.18}$$

For simplicity, MCA assumes that the range of look angles is small enough so that $\tilde{\mathbf{G}}$ can be well approximated by a Cartesian grid. Therefore, the polar-to-Cartesian interpolation process can be ignored in the image reconstruction process and Eqn. (3.18) reduces to solving

$$\frac{1}{MN} \sum_{m,n} \tilde{\mathrm{G}}[m,n] \; e^{-j\phi(m)} e^{j2\pi\left(\frac{u_r m}{K} + \frac{v_r n}{L}\right)} \approx 0 \tag{3.19}$$

for $\phi(1), \phi(1), \cdots, \phi(M)$ and for $r = 1, 2, \ldots, R$. Using vector notation, the autofocus problem reduces to finding a vector $\mathbf{x} \in \mathbb{C}^M$ such that

$$\mathrm{A}\mathbf{x} = 0, \quad |\mathbf{x}_i| = 1, \quad i = 1, 2, \cdots, M, \tag{3.20}$$

where $\mathbf{A}$ is an R by M matrix with elements

$$\mathbf{A}[m, r] \;\; = \;\; \frac{1}{MN} \sum_{n} \tilde{\mathrm{G}}[m,n] e^{j2\pi\left(\frac{u_r m}{M} + \frac{v_r n}{N}\right)}. \tag{3.21}$$

A naive approach to this problem is to try solving this system of equations exactly. In practice, the measurements are noisy and the approximately zero-valued pixels are not exactly zero. Instead, requiring that the low-return region has minimum energy leads to the following optimization problem

$$(P - MCA) \quad e^{j\hat{\boldsymbol{\phi}}_{MCA}} = \underset{\mathbf{x}:|\mathbf{x}_i|=1}{\operatorname{argmin}} \|\mathbf{A}\,\mathbf{x}\|^2. \tag{3.22}$$

Thus, the MCA approach reduces to solving a standard CMQP with $\mathbf{Q} = \mathbf{A}^H\mathbf{A}$. In the original MCA paper [29], an approximate solution was proposed using an EVR approach. A better approximation can be obtained using our proposed SDR through an increase in computational cost.

For completeness, we note that the original MCA derivation used a more general framework with arbitrary basis functions, and worked in the spatial domain rather than the Fourier domain. The SDR method can be applied equally well in that framework.

3.2.3 Fourier-domain Multichannel Autofocus

Only on rare occasions does SAR operate over a range of look angles spanning a small fraction of one degree. MCA breaks down quickly as the range of look angles becomes larger [30]. FMCA is a generalization of MCA that recognizes that the collected Fourier data is in polar format and the interpolation process cannot be ignored. FMCA requires that the polar-to-Cartesian interpolation be *linear* to preserve the linear structure of the inverse problem. In practice, linear interpolation is almost always used, for example see [5]. With linear interpolation, the Cartesian grided data, denoted by $\mathrm{G}_c[k,l]$, can be expressed as.

$$\mathrm{G}_c[k,l] = \sum_{m,n} \alpha(k,l,m,n)\mathrm{G}[m,n], \tag{3.23}$$

where $\alpha(k,l,m,n)$ are the interpolation coefficients. In this chapter we used a nearest-neighbor interpolation for simplicity. Thus $\alpha(k,l,m,n) = 1$ when $\mathrm{G}_p[m,n]$ is closest to $G_c[k,l]$ and 0 otherwise. In principle, any linear interpolation can be used and accommodated within this framework. Assuming $g[u_r, v_r]$ are nearly zero, and together with Eqn. (3.23), (3.19) and (3.15), FMCA formulates the autofocus problem as the solution to

$$\frac{1}{KL}\sum_{k,l}\sum_{m,n}\alpha(k,l,m,n)\tilde{G}[m,n]\; e^{-j\phi(m)}e^{j2\pi\left(\frac{u_r k}{K}+\frac{v_r l}{L}\right)} \approx 0 \tag{3.24}$$

for all $r = 1, 2, \ldots, R$. Similar to MCA, the FMCA problem reduces to finding a vector $\mathbf{x}$ such that

$$\mathbf{B}\mathbf{x} = 0, \quad |\mathbf{x}_i| = 1, \quad i = 1, 2, \cdots, M \tag{3.25}$$

where $\mathbf{B}$ is an R by M matrix with elements

$$B[m,r] = \frac{1}{KL}\sum_{k,l}\left(\sum_{n}\alpha(k,l,m,n)\tilde{G}[m,n]\right)\; e^{j2\pi\left(\frac{u_r k}{K}+\frac{v_r l}{L}\right)}. \tag{3.26}$$

In practice, it is more reasonable to assume that the low-return region has small energy. Therefore, FMCA attempts to solve the following optimization problem:

$$(P - FMCA) \quad e^{j\hat{\boldsymbol{\phi}}_{FMCA}} = \underset{\mathbf{x}:|\mathbf{x}_i|=1}{\operatorname{argmin}}\ \|\mathbf{B}\ \mathbf{x}\|^2. \tag{3.27}$$

Thus the FMCA approach reduces to solving a standard CMQP with $\mathbf{Q} = \mathbf{B}^H\mathbf{B}$. In the original FMCA method [59, 60], an approximate solution was proposed using an EVR approach. In the next section, we will demonstrate that a better approximation can be obtained using the SDR technique in exchange for an increase in computational cost.

3.3 Simulation Results

In this section, we provide a few illustrative numerical examples showing the advantages of the SDR approach in comparison with existing autofocus algorithms, as measured by the MSE of the phase estimates and the SNR of the image restoration. We examine narrow and wide ranges of look angles, as well as the bistatic scenario. In this section we denote PGA-SDR, MCA-SDR and FMCA-SDR as the algorithms using SDR to approximate $(P-PGA)$ in Eqn. (3.17), $(P-MCA)$ in Eqn. (3.22) and $(P-FMCA)$ in Eqn. (3.27), respectively.

3.3.1 SAR Simulator

In order to test the different algorithms, we built a SAR simulator which generated a target complex reflectivity matrix g and its observations $\tilde{\mathbf{G}}$. The amplitudes of g were taken from a real SAR image obtained from Sandia National Laboratory, and the phases, following [29], were chosen as *i.i.d.* with uniform distribution. This reflectivity matrix was multiplied by a 2-D antenna pattern, and then a 2-D discrete Fourier transform (DFT) was applied. The resulting Fourier matrix was then linearly interpolated to polar coordinates described by $(F_x[m,n], F_y[m,n]),\ m = 1,\cdots,M,\ n = 1,\cdots,M$ to obtain the $M \times N$ polar format data $\mathbf{G}$. The set $m = 1\cdots,M$ comprises the look angles adopted in each simulation, and the set $n = 1\cdots,M$ was chosen so that the resulting polar coordinates were circumscribed by the Cartesian grid of the reflectivity Fourier matrix. Finally, the noisy and phase-corrupted observations $\tilde{\mathbf{G}}$ were simulated as expressed in Eqn. (3.15).

Our simulator employed two antenna patterns: a trapezoidal pattern with unit gain over 90 percent of the image and linearly increasing attenuation to γ, $0 < \gamma < 1$, at the edge of the image; and a 2-D sinc-squared pattern with 95 percent of the mainlobe covering the image. Our simulator generated a white phase error where each $\phi(m)$ was independent and uniformly distributed between $-\pi$ and π.

The signal-to-noise-ration (SNR) for the additive noise is defined as:

$$\mathrm{SNR} = 20\log_{10}\left(\frac{1}{\sigma_n MN}\sum_{m,n}|\tilde{\mathrm{G}}[m,n]|\right). \tag{3.28}$$

To evaluate the performance of various image restoration method, we used the output SNR metric, SNR_{out}, defined as:

$$\text{SNR}_{out} = 20 \log_{10} \frac{\|\text{vec}(g)\|_2}{\|(|\text{vec}(g)| - |\text{vec}(\hat{g})|)\|_2}, \tag{3.29}$$

where $\hat{g}$ is the reconstructed image. SNR_{out} measures the pixel-wise magnitude difference between the reconstructed image $\hat{g}$ and the perfectly focused image g. A higher SNR_{out} value corresponds roughly to a better restoration.

3.3.2 Reconstruction Experiments

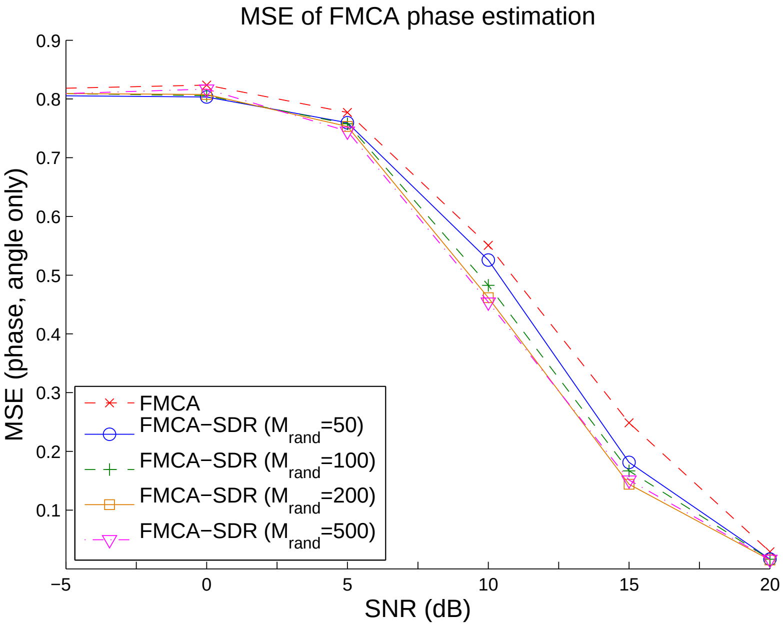

Figure 3.1: Mean Square Error of the FMCA and FMCA-SDR phase estimation (with $M_{rand} = 50, , 100, 200, 500$ number of randomization).

Before we show the results for the image restoration, we first compare the MSE of the phase error estimates produced by FMCA and FMCA-SDR with different number of randomizations (M_{rand}=50,100,200,500). The simulation settings are as follows. This simulation assumed a narrow range of look angles scenario, so MCA is equal to FMCA

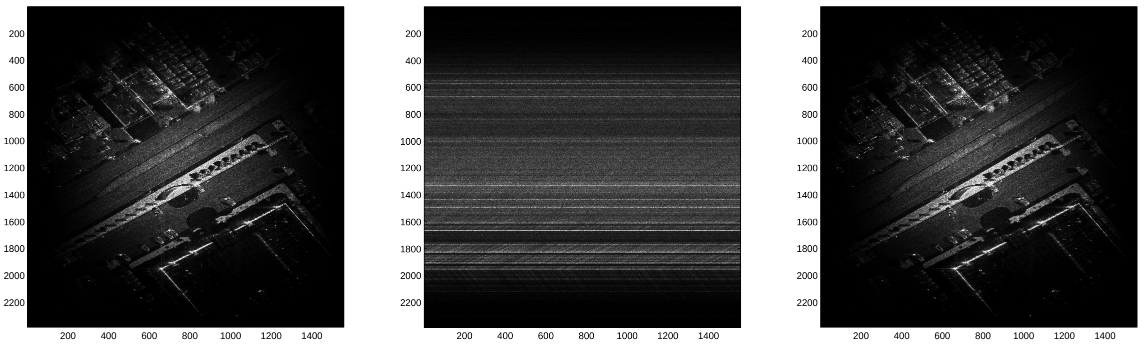

(a) (b) (c)

Figure 3.2: Example of MCA-SDR restoration using an actual size image of 2385 by 1557: (a) perfectly focused image, where a 2-D sinc-squared antenna pattern is applied; (b) defocused image produced by applying a white phase error function; (c) image restored by MCA-SDR.

in this case. We used Fig. 3.3 (a) as the input image and applied a rectangular antenna pattern. The rectangular antenna pattern has unit gain over most of the image and linearly attenuates at the edge of the image. The image is corrupted by a white phase error function. The Monte-Carlo simulation result is shown in Fig. 3.1. From the plot, we see that FMCA-SDR always outperforms FMCA. Furthermore, increasing the number of randomizations in FMCA-SDR does not improve the performance by much. For this particular simulation, the reconstructed image was noticeably blurry for SNR¡10dB.

Now we demonstrate the performance of image restoration using SDR. We first compare image restoration using PGA-SDR and PGA. This is shown in Fig. 3.3. Figure 3.3 (a) is the focused image with added noise SNR = 5 dB. Figure 3.3 (b) shows the image corrupted by a smooth phase error function, (c) shows the image restored by PGA-SDR and (d) shows the image restored by PGA.

Next, we test image restoration under the MCA/FMCA framework. In the case of small look angles, the collected Fourier data is well approximated as lying on a Cartesian grid and FMCA is equivalent to MCA. Thus, in this part we only present the simulation

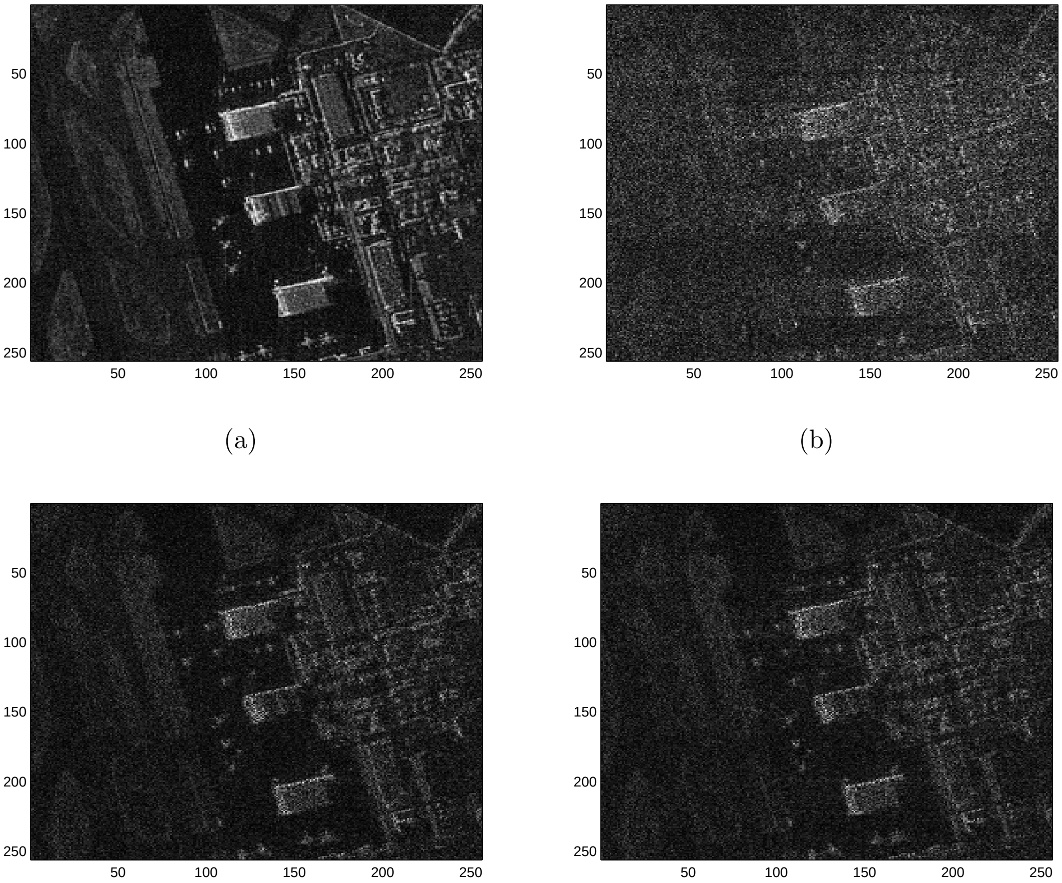

(a) (b)

(c) (d)

Figure 3.3: Comparison of PGA-SDR and PGA image restoration: (a) perfectly focused image with added complex gaussian noise (SNR = 5 dB); (b) defocused image produced by applying a smooth phase error function; (c) PGA-SDR restoration ($\text{SNR}_{out} = 5.06$ dB); (d) PGA restoration ($\text{SNR}_{out} = 4.53$ dB).

results for MCA-SDR and MCA. Figure 3.2 presents an experiment using an actual size SAR image (2385 by 1557). Figure 3.2(a) shows the uncorrupted image where a 2-D sinc-squared antenna pattern is applied. The field of view equals 95 percent of the mainlobe of the sinc-squared antenna pattern, i.e., the image is cropped within the nulls of the antenna pattern, so that there is a very large (but not infinite) attenuation at the edges of the image. Figure 3.2(b) shows a defocused image produced by applying a white phase error function. The problem size for this simulation is $M = 1557$. After obtaining a solution for (SDR) using the spectral-bundle method, MCA-SDR used randomization with $M_{rand} = 200$ to find the phase estimates and reconstruct the image. The MCA-SDR restoration is shown in Fig. 3.2(c).

The goal of the next simulation was to evaluate the robustness of MCA-SDR with respect to the low-return assumption. We used the focused image in Fig. 3.8(a) with a trapezoidal antenna pattern applied. The trapezoidal antenna pattern had an attenuation of $\gamma = 10^{-0.5}$ at the edge of the image. The defocused image is shown in Fig. 3.8(b). The MCA reconstruction using SDR is presented in Fig. 3.8(c), and the reconstruction using EVR is shown in Fig. 3.8(d). It is clear that SDR produced a better visual result. This improvement is also apparent in the output SNR where EVR resulted in 5.65dB and SDR in 8.43dB. The comparison of SNR$_{out}$ between EVR and SDR as a function of varying attenuation γ in the low-return region is shown in Fig. 3.4.

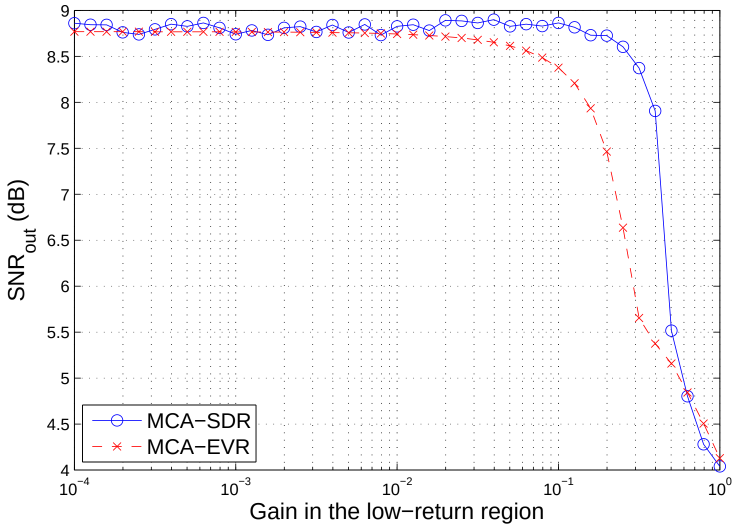

Figure 3.4: Comparison of MCA-SDR and MCA-EVR image restoration, measured by SNR$_{out}$, as a function of attenuation γ in the low-return region.

Figure 3.9 compares the performance of MCA-SDR with existing autofocus techniques. Figure 3.9(a) shows a perfectly focused image with a rectangular antenna pattern applied (the gain at the edge is 10^{-4} in this experiment). To model system noise, a complex gaussian noise with signal-to-noise-ratio SNR equal to 40 dB was added to the defocused image. The defocused image formed with white phase error corruption is shown in Fig. 3.9(b). Figure 3.9(c) shows the MCA-SDR restoration assuming the first two and last two column to be the low-return region. The restoration of MCA is shown in Fig. 3.9(d) with the same low-return region assumption in part (c). Image restored by sharpness maximizing autofocus algorithm using entropy metric is shown in Fig. 3.9(e). And the PGA restoration is shown in Fig. 3.9(f).

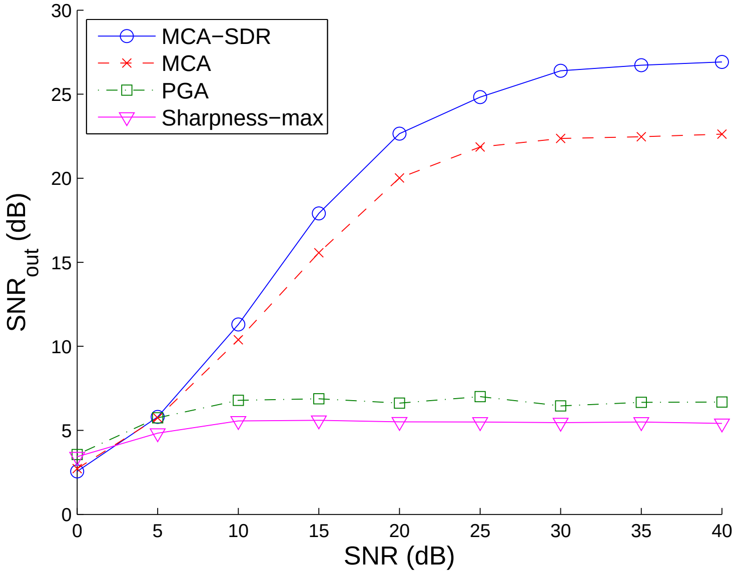

Figure 3.5: Comparison of MCA-SDR with existing autofocus approaches.

Figure 3.5 presents results of a Marte Carlo simulation comparing MCA-SDR with existing autofocus algorithms under varying levels of additive noise in the uncorrupted image. Ten trials were conducted for each SNR level, where in each trial a noisy focused image was first generated and then the defocused image was formed by applying a white phase corruption. Four autofocus algorithms (MCA-SDR, MCA, PGA, Sharpness-maximization) were applied to each defocused image and the result is evaluated by SNR$_{out}$. Plot of the average SNR$_{out}$ verses different SNR is shown in Fig. 3.5. The plot shows that at high input SNR (SNR $>$ 10 dB), MCA-SDR outperformed MCA and other autofocus methods.

When the range of look angles is wide ($>$ 3 degree) only FMCA is capable of producing a focused image while MCA and PGA methods breaks down due to the fact that the phase error can no longer be approximated by an 1-D function as shown in (2.4). Thus, in the next part we only show the result of FMCA when compared with SDR approach. In the FMCA simulation, we adopted the following scenario: the SAR collected data over 36 degree look angles, the radar transmitted 1500 pulses ($M = 1500$) and the receiver provided 800 samples per single pulse ($N = 800$). This simulation used the focused image in Fig. 3.10(a), a white phase error function (defocused image shown in Fig. 3.10(b)), a 2-D sinc-squared antenna pattern, and input SNR with value 14.2 dB. The FMCA reconstruction using SDR is presented in Fig. 3.10(c) and the reconstruction using EVR is shown in Fig. 3.10(d). As before, it is easy to see the visual image enhancement due to the use of SDR. In order to demonstrate the effect of input SNR on restoration quality, Fig. 3.6 presents the output versus input SNRs for a 50 by 50 ”toy” image collected on a polar grid with a 2 degree range of look angles. As expected, at high input SNR both EVR and SDR succeed in estimating the unknown phases, but the advantage of SDR is significant in cases with medium input SNR where the low-return region assumption is inexact.

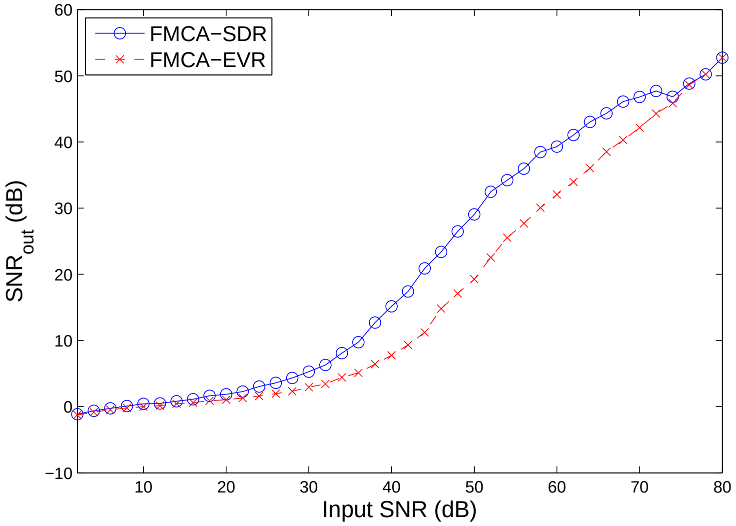

Figure 3.6: Comparison of FMCA-SDR and FMCA-EVR image restoration, measured by SNR$_{out}$.

We also report the results of an additional FMCA simulation conducted for a bistatic SAR system. We considered a bistatic SAR scenario where a moving transmitter and a moving receiver traverse a straight-line trajectory, perpendicular to each other. The specific parameters were as follows: 2000 transmitted linear FM pulses (bandwidth to center frequency ratio equal to 0.7027) over a 55.31 degree range of look angles. The receiver collected reflected signals over a 44.71 degree range of look angles. The collected Fourier data pattern for this bistatic SAR scenario is shown in Fig. 3.7. The focused image with a 2-D sinc-squared antenna pattern applied and input SNR equal to 50dB is shown in Fig. 3.11 (a). The defocused image, corrupted by a white phase error, is shown in Fig. 3.11 (b). The images restored by FMCA-SDR and FMCA-EVR are shown in Fig. 3.11 (c) and Fig. 3.11 (d), respectively. Here too, the advantage of SDR over EVR is apparent.

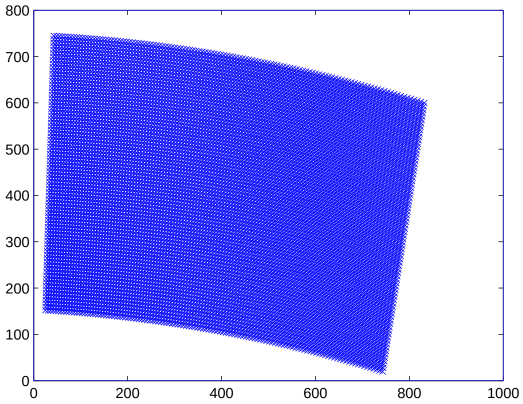

Figure 3.7: Collected Fourier data pattern for Bistatic SAR.

In all of the simulations reported above we implemented SDR via the bundle method [52]. To give a rough idea of its computational cost, the run time for the EVR simulation with Fig. 3.10(a) as input required less than 30 minutes on a HP Z200 (Quad 2.66 GHz) PC with 8GB of RAM, while SDR required about 24 hours.

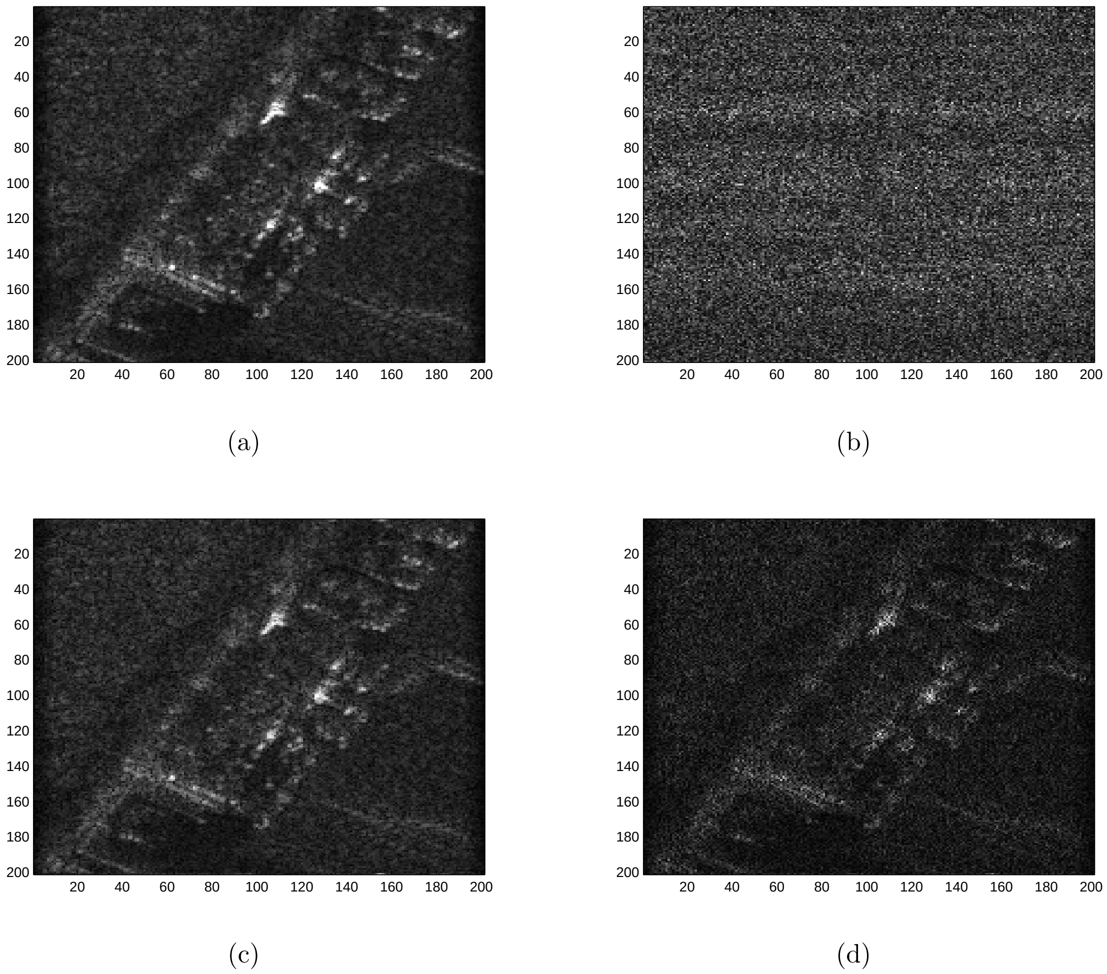

(a) (b) (c) (d)

Figure 3.8: Experiments evaluating the robustness of MCA-SDR and MCA as a function of the attenuation in the low-return region: (a) perfectly focused image, where a trapezoidal antenna pattern is applied; (b) defocused image produced by applying a white phase error function; (c) image restored by MCA-SDR ($\text{SNR}_{out} = 8.43$ dB); (d) image restored by MCA-EVR ($\text{SNR}_{out} = 5.65$ dB).

3.4 Chapter Summary

In this chapter, we proposed to use semidefinite relaxation (SDR) to improve three state-of-the-art SAR autofocus algorithms, namely Phase Gradient Autofocus (PGA), Multichannel Autofocus (MCA) and Fourier-domain Multichannel Autofocus (FMCA). We first recognized that, although PGA, MCA and FMCA are developed based on different models and assumptions, they all attempt to find a solution to a constant modulus quadratic program (CMQP). CMQP is known to be NP-hard. PGA, MCA and FMCA all, either implicitly or explicitly, use eigenvalue relaxation to approximate the CMQP. We proposed to use SDR to approximate the CMQP arising in each of the three algorithms. Experimental results showed that SDR provided promising image restoration advantages over existing methods, especially for MCA and FMCA. Although solving autofocus problem using the new method is more computationally expensive, there may be crucial situations where it is imperative that an image be focused as well as possible, using computationally intensive off-line processing.

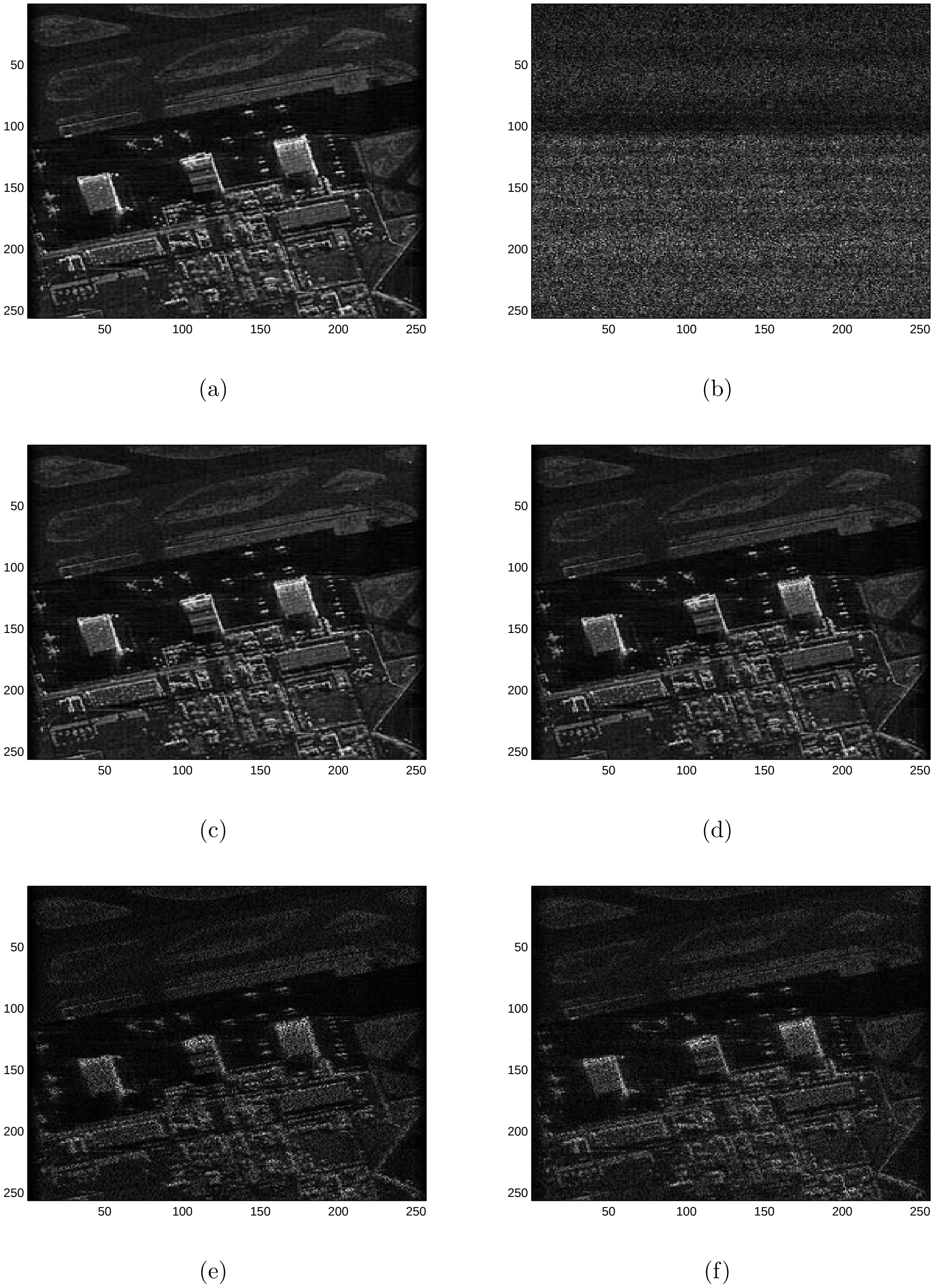

(a)

(b)

(c)

(d)

(e)

(f)

Figure 3.9: Comparison of MCA-SDR with existing autofocus approaches: (a) perfectly focused image with added complex gaussian noise (SNR = 40 dB) and applied square antenna pattern; (b) defocused image produced by applying a white phase error function; (c) MCA-SDR restoration ($\text{SNR}_{out} = 30.80$ dB); (d) MCA restoration ($\text{SNR}_{out} = 20.40$ dB); (e) Sharp-maximization restoration ($\text{SNR}_{out} = 5.49$ dB); (f) PGA restoration ($\text{SNR}_{out} = 5.84$ dB).

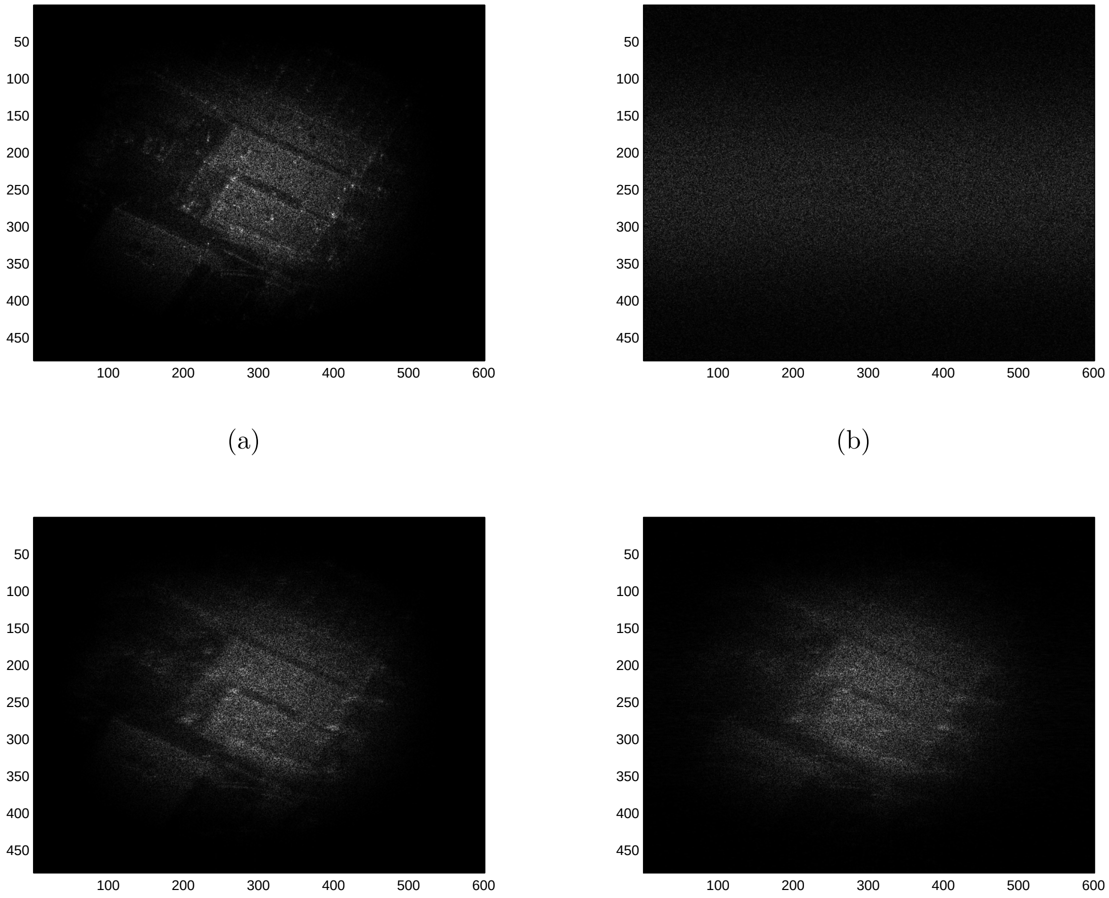

(a) (b)

(c) (d)

Figure 3.10: Image restoration of FMCA-SDR and FMCA-EVR for wide-angle SAR autofocus: (a) perfectly focused image with added complex gaussian noise and applied 2-D sinc-squared antenna pattern; (b) defocused image produced by applying a white phase error function; (c) FMCA-SDR restoration ($\text{SNR}_{out} = 3.87$ dB); (d) FMCA-EVR restoration ($\text{SNR}_{out} = 3.88$ dB).

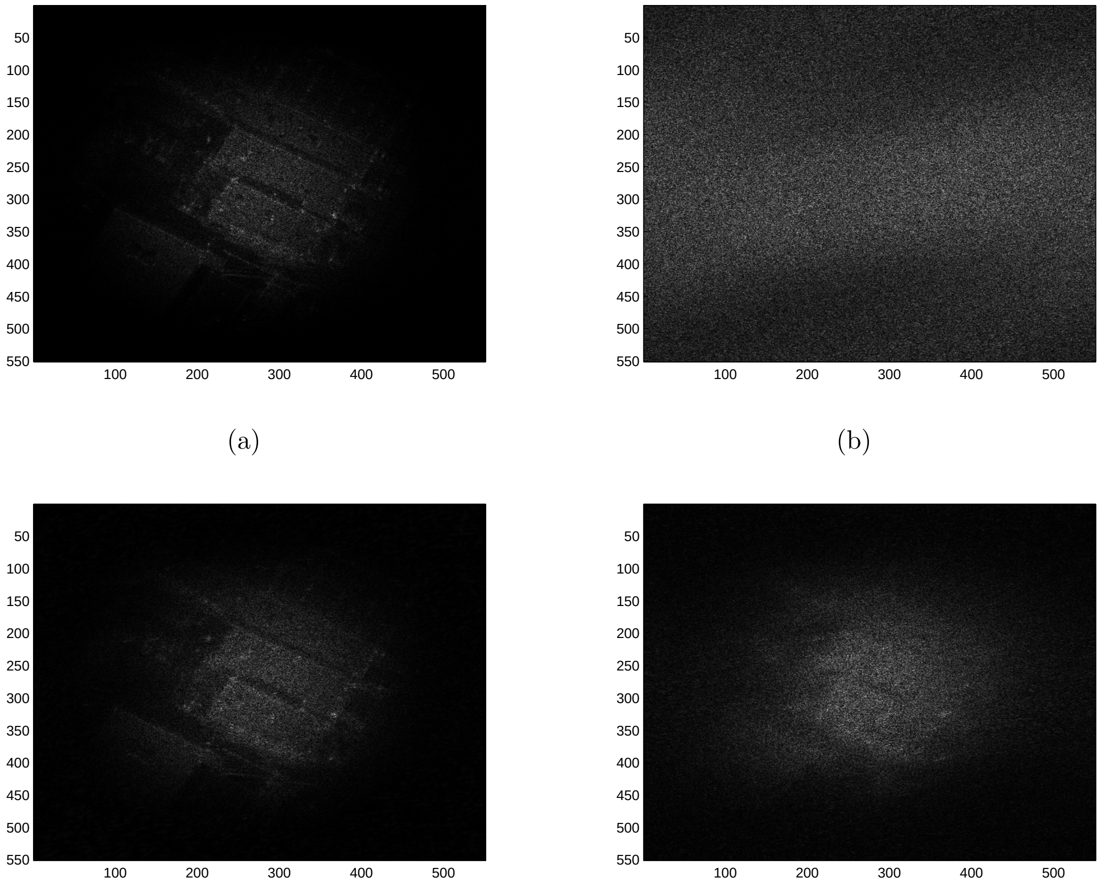

(a) (b)

(c) (d)

Figure 3.11: Comparison of FMCA-SDR and FMCA for bistatic SAR autofocus: (a) perfectly focused image with added complex Gaussian noise and applied 2-D sinc-squared antenna pattern; (b) defocused image produced by applying a white phase error function; (c) FMCA-SDR restoration ($\text{SNR}_{out} = 4.88$ dB); (d) FMCA restoration ($\text{SNR}_{out} = 3.16$ dB).

CHAPTER 4

SAR Autofocus based on a Bilinear Model

In this chapter, we propose a novel autofocus reconstruction algorithm that is based on a bilinear parametric model. Following [61, 62, 63, 64], we consider a standard linear model for the reflectivity function using a finite vector $\boldsymbol{\theta}$ of unknown parameters. On the other hand, similar to [29, 59, 60], we propose a linear model for the SAR acquisition system involving a vector of unknown phase distortions $\boldsymbol{\gamma}$. Together, we obtain a bilinear model involving the unknown parameters $\{\boldsymbol{\theta}, \boldsymbol{\gamma}\}$ contaminated by additive noise. We analyze the conditions for identifiability and solvability of the problem in the noiseless case, and then derive a novel maximum likelihood autofocus (MLA) method to deal with noisy observations.

MLA can be interpreted as a generalization of MCA to a larger class of models and a wider range of look angles. In the simplest setting, namely an impulse reflectivity model with a known support constraint and a small range of look angles, MCA coincides with MLA. However, our results show that MCA's FMCA extension is suboptimal in comparison with MLA. The latter requires weaker identifiability conditions, and small error analysis reveals that it is significantly less sensitive to noise. Furthermore, MLA is more general from the standpoint that it does not require the existence of a prior low-return region. In some sense, FMCA may be considered more robust as it does not rely on any explicit parametric reflectivity model. However, the numerical simulation results presented in [59, 60] are based on a special case of our model, and we present numerical evidence that MLA is superior to FMCA also under mismatched models. From a computational cost perspective, MCA, FMCA and MLA are very similar. At their core, is the solution to a constant modulus quadratic program (CMQP) and can be approximated by methods discussed in Chapter 3.

The organization of this chapter is as follows. In Section 4.1 we introduce the proposed bilinear problem formulation. In Section 4.2, we discuss the conditions for perfect reconstruction in the noiseless case. In Section 4.3, we derive MLA and discuss its implementation. In Section 4.4, we compare MLA with FMCA through their small error analysis. Simulation results are presented in Section 4.5 and concluding remarks are provided in Section 4.6.

4.1 Problem Formulation

In this section, we present a parametric bilinear model for the SAR autofocus problem.

4.1.1 SAR Reflectivity Function Model

SAR systems image a continuous target reflectivity function denoted by $r(x, y)$. Most reconstruction methods assume a finite parametric model for $r(x, y)$. This parametric model can be mathematically described as

$$r(x,y) = \sum_{i=1}^{D} \theta_i \, h_i(x,y). \tag{4.1}$$

where $\boldsymbol{\theta} = [\theta_1, \cdots, \theta_D]^T$ is a complex valued parameter vector of dimension D and $h_i(x, y)$ for $i = 1, \cdots, D$ are known complex valued functions. Common physical models that can be characterized by Eqn. (4.1) include:

(A) Impulse model: $r(x, y)$ is decomposed into D resolution cells, each with size $dx \times dy$,

where dx and dy are two known constants determined by the SAR radar specification. Any two point reflectors within a resolution cell cannot be well-resolved. With this framework, one way of approximating a SAR system is to use a discrete model where a single complex number is assigned to each resolution cell. This complex number, denoted by θ_i, represents the sum of the point reflectors' reflectivities within a resolution cell and can be simply viewed as an impulse located at the center of the cell. This leads to the following definition:

$$h_i(x,y) = \delta\left(x - u_i\, dx,\, y - v_i\, dy\right), \tag{4.2}$$

where $\delta(\cdot)$ denotes the standard dirac delta function, and u_i and v_i are the spatial indices for the ith resolution cell.

(B) Sampling model: In this model, $\boldsymbol{\theta}$ represents discrete samples of $r(x,y)$, and the $h_i(x,y)$ represent the sampling kernel. A typical assumption in this model is a band-limited reflectivity function which involves a finite number of parameters. Previous works that use this model include [61, 62, 63].

(C) Discrete speckle model: In this model, SAR imaging is viewed as a statistical inverse problem and it is recognized that it is possible to reconstruct only a speckle version of $r(x,y)$. Here, Eqn. (4.1) can be interpreted as an approximate model for the speckle image [5, 6].

(D) Additional prior information: Additional linear constraints may be incorporated into the model if prior information about the underlying scene is known. For example, previous work assumed knowledge of a zero (or low) valued region in the underlying scene [29, 59, 60]. Such information corresponds to elements in $\boldsymbol{\theta}$ with known zero values. Alternatively, this can be translated into a linear model of reduced dimension (smaller value of D).

4.1.2 SAR Acquisition Model

Under the far-field assumption and using a narrow-band transmitted waveform, the collected SAR data, denoted by $\mathrm{G}[m,n]$, can be modeled as the Fourier transform of $r(x,y)$ evaluated at non-uniform frequency locations $(F_x[m,n], F_y[m,n])$ for $m = 1,\cdots,M$ and $n = 1,\cdots,N$:

$$\mathrm{G}[m,n] = \int\int r(x,y) e^{-j2\pi\left(F_x[m,n]\,x + F_y[m,n]\,y\right)} dxdy. \tag{4.3}$$

Substituting Eqn. (4.3) back into our parametric model for the reflectivity function yields

$$\mathrm{G}[m,n] = \sum_i \theta_i \int\int h_i(x,y)\, e^{-j2\pi\left(F_x[m,n]\,x + F_y[m,n]\,y\right)} dxdy. \tag{4.4}$$

Using vector notation

$$\mathbf{g} = \mathrm{vec}(\mathbf{G}), \tag{4.5}$$

there is a simple linear relation between $\boldsymbol{\theta}$ and $\mathbf{g}$ which can be expressed as

$$\mathbf{g} = \mathbf{L}\boldsymbol{\theta} \tag{4.6}$$

where $\mathbf{L}$ is a $MN \times D$ matrix with elements:

$$\mathrm{L}[k,l] = \int\int h_i(x,y)\, e^{-j2\pi(F_x[a,b]\,x + F_y[a,b]\,y)} dxdy,$$

$$a = \lfloor l/N \rfloor, b = \mathrm{mod}(l,N),\ i = \lfloor k/V \rfloor \cdot V + \mathrm{mod}(k,V) \tag{4.7}$$

where $\lfloor\cdot\rfloor$ denotes "integer part of," and $\mathrm{mod}(l,N)$ denotes "l modulo N."

Conventional SAR reconstruction amounts to inversion of this linear transformation to reconstruct $\boldsymbol{\theta}$ as

$$\hat{\boldsymbol{\theta}} = \mathbf{L}^{\dagger}\mathbf{g}. \tag{4.8}$$

In the special case of model *(A)* and when SAR operates across a narrow range of look angles, F_x, F_y can be well approximated as a Cartesian grid, thus the matrix $\mathbf{L}$ is simply a DFT matrix and inversion is performed using an efficient Fast Fourier Transform (FFT) [29]. Otherwise, it is common to approximate this pseudo-inversion via interpolation to a uniform Cartesian grid, followed by FFT.

The above SAR model is too idealistic for practical systems. We now extend the model and introduce signal distortion and noise. Specifically, a more realistic observation model is

$$\tilde{\mathrm{G}}[m,n] = \mathrm{G}[m,n]\, e^{j\phi[m,n]} + \mathrm{N}[m,n] \tag{4.9}$$

where $\phi[m,n]$ are autofocus phase distortions and $\mathrm{N}[m,n]$ represents additive noise. The phase distortions result from inaccurate range measurements or unknown signal propagation delays. The polar-format Fourier data is contaminated with unknown phase errors that cause the reconstructed image to suffer distortion. The measurements at a given look angle suffer from the same unknown delay, and, under a narrow-band assumption, this corresponds to an unknown phase. The delays, and their associated phases, change between different look angles. Thus, following [5], we let

$$\phi[m,n] = \phi(m), \qquad m = 1, \cdots, M. \tag{4.10}$$

In addition, without loss of generality, we define

$$\phi(M) = 0 \tag{4.11}$$

and focus on estimating $\phi(1), \cdots, \phi(M-1)$, as we are only interested in the phase differences (PGA in [20] is also based on this approach). The additive noise samples $\mathrm{N}[m,n]$ are assumed to be independent, zero mean, complex normal random variables with variance σ_n^2.

In vector notation, we obtain the following model

$$\tilde{\mathbf{g}} = \mathbf{R}(\boldsymbol{\gamma})\mathbf{L}\boldsymbol{\theta} + \mathbf{n}, \tag{4.12}$$

where $\boldsymbol{\gamma} = [e^{j\boldsymbol{\phi}};\ 1],\ \mathbf{n} = \text{vec}(\mathbf{N})$ and

$$\mathbf{R}(\boldsymbol{\gamma}) = \text{Diag}\Big(\big[\underbrace{\gamma_1, \ldots, \gamma_1}_{\text{N terms}}, \ldots, \underbrace{\gamma_{M-1}, \ldots, \gamma_{M-1}}_{\text{N terms}}, \underbrace{1, \ldots, 1}_{\text{N terms}}\big]\Big). \tag{4.13}$$

Define Γ as the space where $\boldsymbol{\gamma}$ lies, i.e.,

$$\Gamma = \{\boldsymbol{\gamma} : \gamma_M = 1,\ |\gamma_i| = 1,\ i = 1, \cdots, M-1\}, \tag{4.14}$$

Then the SAR autofocus problem can be summarized as: Find $\boldsymbol{\theta}$ (and the nuisance parameters $\boldsymbol{\gamma} \in \Gamma$) using the observations $\tilde{\mathbf{g}}$.

For completeness, we note that a more accurate problem formulation would treat the magnitudes and phases of the complex variables separately. Specifically, other work models the magnitudes and phases of the reflectivity function differently [65], but our goal is only to reconstruct the magnitude information for display [6]. For simplicity and tractability, we use a joint model and estimate both magnitude and phase together. Future work will pursue the more advanced formulation.

4.2 Noiseless Case

The autofocus problem is difficult due to the nonlinear coupling between the unknown reflectivity parameters $\boldsymbol{\theta}$ and the unknown autofocus phases $\boldsymbol{\phi}$. Even if we parameterize the phases via $\boldsymbol{\gamma}$ (rather than the more complicated $\boldsymbol{\phi}$ characterization), there is a bilinear coupling between $\boldsymbol{\theta}$ and $\boldsymbol{\gamma}$. Therefore, in order to understand when can this coupling be resolved, we begin by considering the problem in the noiseless case, i.e., $\mathbf{n} = \mathbf{0}$.

4.2.1 Perfect Reconstruction

Theorem 4.1. In the noiseless case and when $\mathbf{L}$ has full column rank, perfect reconstruction of $\boldsymbol{\gamma}$ and $\boldsymbol{\theta}$ from $\tilde{\mathbf{g}}$ is possible if and only if there is a unique vector $\hat{\boldsymbol{\gamma}}$ such that

$$\hat{\boldsymbol{\gamma}} \in \Gamma \cap \mathcal{N}\big((\mathbf{I} - \mathbf{L}\mathbf{L}^{\dagger})\tilde{\mathbf{Y}}\big) \tag{4.15}$$

where

$$\tilde{\mathbf{Y}} = \begin{bmatrix} \tilde{\mathbf{g}}_{1\dots N} & \mathbf{0} & \cdots & \mathbf{0} \\ \mathbf{0} & \tilde{\mathbf{g}}_{N+1\dots 2N} & \cdots & \mathbf{0} \\ \vdots & \vdots & \ddots & \vdots \\ \mathbf{0} & \mathbf{0} & \cdots & \tilde{\mathbf{g}}_{MN-N+1\dots MN} \end{bmatrix}. \tag{4.16}$$

In this case, $\hat{\boldsymbol{\gamma}} = \boldsymbol{\gamma}$ and

$$\boldsymbol{\theta} = \mathbf{L}^{\dagger}\mathbf{R}(\hat{\boldsymbol{\gamma}})^{-1}\tilde{\mathbf{g}}. \tag{4.17}$$

Proof. Our first step is to decouple $\boldsymbol{\gamma}$ and $\boldsymbol{\theta}$ from Eqn. (4.12). This is done by first recognizing that when $\mathbf{L}$ has full column rank, we can write

$$\boldsymbol{\theta} = \mathbf{L}^{\dagger}\mathbf{R}(\boldsymbol{\gamma})^{-1}\tilde{\mathbf{g}}. \tag{4.18}$$

Substituting Eqn. (4.18) back into Eqn. (4.12), we have

$$\Big(\mathbf{I} - \mathbf{R}(\boldsymbol{\gamma})\mathbf{L}\mathbf{L}^{\dagger}\mathbf{R}(\boldsymbol{\gamma})^{-1}\Big)\tilde{\mathbf{g}} = \mathbf{0} \tag{4.19}$$

or

$$\Big(\mathbf{I} - \mathbf{L}\mathbf{L}^{\dagger}\Big)\mathbf{R}(\boldsymbol{\gamma})^{-1}\tilde{\mathbf{g}} = \mathbf{0}. \tag{4.20}$$

We can rewrite Eqn. (4.20) to explicitly bring out $\boldsymbol{\gamma}$ as

$$\left(\mathbf{I} - \mathbf{L}\mathbf{L}^{\dagger}\right) \tilde{\mathbf{Y}}\boldsymbol{\gamma} = \mathbf{0} \tag{4.21}$$

where $\tilde{\mathbf{Y}}$ is defined in Eqn. (4.16). Together with the requirement $\hat{\gamma} \in \Gamma$ this yields the required condition. □

In practice, our noiseless autofocus algorithm takes $\tilde{\mathbf{Y}}$ as an input and searches for $\hat{\gamma}$ that satisfies Eqn. (4.15). This search is difficult due to the nonconvex set Γ. We propose to relax it, and choose $\hat{\gamma}$ as any properly normalized vector in $\mathcal{N}\big((\mathbf{I} - \mathbf{L}\mathbf{L}^{\dagger})\tilde{\mathbf{Y}}\big)$ rounded to Γ.

4.2.2 Comparison to Previous Methods

We now compare Theorem 4.1 with its competing MCA and FMCA methods. The latter are also based on the noiseless model

$$\tilde{\mathbf{g}} = \mathbf{R}(\boldsymbol{\gamma})\mathbf{L}\boldsymbol{\theta}, \tag{4.22}$$

and it is *a priori* known that some of the elements of $\boldsymbol{\theta}$ are zero valued, i.e.,

$$\boldsymbol{\theta}_a = \mathbf{0}, \tag{4.23}$$

where a is a known set of indices. FMCA searches for a vector $\hat{\boldsymbol{\gamma}} \in \Gamma$ such that the reconstruction satisfies Eqn. (4.23), i.e.,

$$[\mathbf{L}^{\dagger}\mathbf{R}(\hat{\boldsymbol{\gamma}})^{-1}\tilde{\mathbf{g}}]_a = \mathbf{0}. \tag{4.24}$$

In terms of $\tilde{\mathbf{Y}}$ and Γ, the condition for the perfect reconstruction of Eqn. (4.22) is equivalent to requiring a unique vector $\hat{\boldsymbol{\gamma}}$ such that

$$\hat{\boldsymbol{\gamma}} \in \Gamma \cap \mathcal{N}([\mathbf{L}^{\dagger}]_a \tilde{\mathbf{Y}}). \tag{4.25}$$

In our proposed parametric model, the prior information of the set a corresponds to a reduced model. More specifically, let $\bar{a}$ denote the complement of a so that $a \cap \bar{a} = \emptyset,\ \ a \cup \bar{a} = \{1, \cdots, D\}$, and we can partition $\mathbf{L}$ into

$$\mathbf{L} = [\mathbf{L}^{\bar{a}}\ \mathbf{L}^{a}]. \tag{4.26}$$

This gives us the effective model

$$\tilde{\mathbf{g}} = \mathbf{R}(\boldsymbol{\gamma})\mathbf{L}^{\bar{a}}\boldsymbol{\theta}_{\bar{a}}. \tag{4.27}$$

Its necessary and sufficient reconstruction condition is a unique vector satisfying

$$\hat{\boldsymbol{\gamma}} \in \Gamma \cap \mathcal{N}\big((\mathbf{I} - [\mathbf{L}^{\bar{a}}][\mathbf{L}^{\bar{a}}]^{\dagger})\tilde{\mathbf{Y}}\big). \tag{4.28}$$

The following theorem compares these conditions in the noiseless case.

Theorem 4.2. If $\mathbf{L}$ is full column rank (as required for reconstruction in the focused case) then

$$\mathcal{N}\big((\mathbf{I} - [\mathbf{L}^{\bar{a}}][\mathbf{L}^{\bar{a}}]^{\dagger})\tilde{\mathbf{Y}}\big) \subset \mathcal{N}([\mathbf{L}^{\dagger}]_a \tilde{\mathbf{Y}}). \tag{4.29}$$

If $\mathbf{L}$ is also invertible, then conditions (4.25) and (4.28) are equivalent since

$$\mathcal{N}\big((\mathbf{I} - [\mathbf{L}^{\bar{a}}][\mathbf{L}^{\bar{a}}]^{\dagger})\tilde{\mathbf{Y}}\big) = \mathcal{N}([\mathbf{L}^{\dagger}]_a \tilde{\mathbf{Y}}). \tag{4.30}$$

Proof. First, let $\mathbf{s} \in \mathcal{N}\big((\mathbf{I} - [\mathbf{L}^{\bar{a}}][\mathbf{L}^{\bar{a}}]^{\dagger})\tilde{\mathbf{Y}}\big)$ so that $\big(\mathbf{I} - \mathbf{L}^{\bar{a}}[\mathbf{L}^{\bar{a}}]^{\dagger}\big)\tilde{\mathbf{Y}}\mathbf{s} = 0$. This implies that $\tilde{\mathbf{Y}}\mathbf{s}$ is in the column space of $\mathbf{L}^{\bar{a}}$ and therefore there exists a vector $\mathbf{z}$ such that $\tilde{\mathbf{Y}}\mathbf{s} = \mathbf{L}^{\bar{a}}\mathbf{z} = \mathbf{L}[\mathbf{z}; \mathbf{0}]$. We have

$$[\mathbf{L}^{\dagger}]_a \tilde{\mathbf{Y}}\mathbf{s} = [\mathbf{L}^{\dagger}]_a \mathbf{L}[\mathbf{z}; \mathbf{0}] = [\mathbf{L}^{\dagger}\mathbf{L}[\mathbf{z}; \mathbf{0}]]_a = [\mathbf{z}; \mathbf{0}]_a = \mathbf{0}, \tag{4.31}$$

so $\mathbf{s} \in \mathcal{N}([\mathbf{L}^{\dagger}]_a \tilde{\mathbf{Y}})$ and we have the desired result.

On the other hand, assume $\mathbf{L}$ is also invertible, so that $\mathbf{L}^{\dagger} = \mathbf{L}^{-1}$. Let $\mathbf{v} \in \mathcal{N}([\mathbf{L}^{-1}]_a \tilde{\mathbf{Y}})$ and $\boldsymbol{\theta}' = \mathbf{L}^{-1}\tilde{\mathbf{Y}}\mathbf{v}$. Since $[\mathbf{L}^{-1}]_a \tilde{\mathbf{Y}}\mathbf{v} = \mathbf{0}$, we have $\boldsymbol{\theta}'_a = \mathbf{0}$ and $\tilde{\mathbf{Y}}\mathbf{v} = \mathbf{L}^{\bar{a}}\boldsymbol{\theta}'_{\bar{a}}$. Now, we have

$$\begin{aligned}
\big(\mathbf{I} - [\mathbf{L}^{\bar{a}}][\mathbf{L}^{\bar{a}}]^{\dagger}\big)\tilde{\mathbf{Y}}\mathbf{v} &= \tilde{\mathbf{Y}}\mathbf{v} - \mathbf{L}^{\bar{a}}([\mathbf{L}^{\bar{a}}]^H[\mathbf{L}^{\bar{a}}])^{-1}[\mathbf{L}^{\bar{a}}]^H\tilde{\mathbf{Y}}\mathbf{v} \\
&= \mathbf{L}^{\bar{a}}\boldsymbol{\theta}'_{\bar{a}} - \mathbf{L}^{\bar{a}}([\mathbf{L}^{\bar{a}}]^H\mathbf{L}^{\bar{a}})^{-1}[\mathbf{L}^{\bar{a}}]^H\mathbf{L}^{\bar{a}}\boldsymbol{\theta}'_{\bar{a}} \\
&= \mathbf{0},
\end{aligned} \tag{4.32}$$

so $\mathbf{v} \in \mathcal{N}\big((\mathbf{I} - [\mathbf{L}^{\bar{a}}][\mathbf{L}^{\bar{a}}]^{\dagger})\tilde{\mathbf{Y}}\big)$.

□

Thus, MCA is optimal in the noiseless case in the sense that it is equivalent to Theorem 4.1. Indeed, in MCA the matrix $\mathbf{L}$ is a square, invertible and unitary DFT matrix. On the other hand, its generalization to non-square matrices via FMCA is suboptimal and requires a condition which is too strong. Therefore, we interpret Theorem 4.1 as the correct extension of MCA to non-square matrices and generalized parametric models with or without low-return regions.

4.3 Maximum Likelihood Estimation

The previous section addressed conditions and methods for perfect reconstruction in the noiseless case. In practice, the measurements are also corrupted by additive noise as expressed in Eqn. (4.12). We now assume that the conditions in Theorem 4.1 hold so that the problem is solvable and we extend the previous results to the noisy case based on a maximum likelihood (ML) framework.

ML is the classical statistical method for estimating deterministic unknown parameters. In the presence of Gaussian noise (e.g. thermal receiver noise), the method reduces to nonlinear least-squares estimation. Its main advantage is that it is known to minimize the mean squared error among all unbiased estimators in low noise conditions, i.e., small error analysis shows that ML attains the Cramer-Rao bound (CRB) on the estimation error. Specifically, we define the MLA estimator as the solution to

$$\begin{aligned}[\hat{\boldsymbol{\gamma}}_{ML}, \hat{\boldsymbol{\theta}}_{ML}] &= \underset{\boldsymbol{\gamma}\in\Gamma,\boldsymbol{\theta}}{\operatorname{argmin}} \left\| \tilde{\mathbf{g}} - \mathbf{R}(\boldsymbol{\gamma})\mathbf{L}\boldsymbol{\theta} \right\|^2 \\ &= \underset{\boldsymbol{\gamma}\in\Gamma,\boldsymbol{\theta}}{\operatorname{argmin}} \left\| \mathbf{R}^{-1}(\boldsymbol{\gamma})\tilde{\mathbf{g}} - \mathbf{L}\boldsymbol{\theta} \right\|^2, \qquad (4.33)\end{aligned}$$

where we have used the invariance of the norm to unitary transformation. Now, we can easily solve for $\hat{\boldsymbol{\theta}}_{ML}$

$$\hat{\boldsymbol{\theta}}_{ML} = \mathbf{L}^{\dagger}\mathbf{R}^{-1}(\boldsymbol{\gamma})\tilde{\mathbf{g}}. \qquad (4.34)$$

Substitute Eqn. (4.34) back into Eqn. (4.33), we have

$$\begin{aligned}\hat{\boldsymbol{\gamma}}_{ML} &= \underset{\boldsymbol{\gamma}\in\Gamma}{\operatorname{argmin}} \left\| \left(\mathbf{I} - \mathbf{L}\mathbf{L}^{\dagger}\right) \mathbf{R}^{-1}(\boldsymbol{\gamma})\tilde{\mathbf{g}} \right\|^2 \qquad (4.35) \\ &= \underset{\boldsymbol{\gamma}\in\Gamma}{\operatorname{argmin}} \left\| \left(\mathbf{I} - \mathbf{L}\mathbf{L}^{\dagger}\right) \tilde{\mathbf{Y}}\boldsymbol{\gamma} \right\|^2 \qquad (4.36)\end{aligned}$$

where we have used the notation in Eqn. (4.16). As discussed in Chapter 3, this problem is a constant modulus quadratic programming (CMQP), which is generally NP-hard, but can be approximated well under suitable conditions.

4.3.1 Comparison to Previous Methods

The previous MCA and FMCA methods also recognized that the measurements may be noisy and proposed to approximate Eqn. (4.24) via minimizing the energy in the low-return region of the reconstructed image, i.e.,

$$\begin{aligned}\hat{\boldsymbol{\gamma}}_{FMCA} &= \underset{\boldsymbol{\gamma}\in\Gamma}{\operatorname{argmin}} \left\| [\mathbf{L}^{\dagger}]_a \mathbf{R}^{-1}(\boldsymbol{\gamma})\tilde{\mathbf{g}} \right\|^2 \\ &= \underset{\boldsymbol{\gamma}\in\Gamma}{\operatorname{argmin}} \left\| [\mathbf{L}^{\dagger}]_a \tilde{\mathbf{Y}}\boldsymbol{\gamma} \right\|^2 . \end{aligned} \tag{4.37}$$

Similar to MLA, this is a NP-hard CMQP optimization problem, but can be approximated using methods discussed in Chapter 3.

Comparing Eqn. (4.36) with the reduced model $\mathbf{L}^{\bar{a}}$ to Eqn. (4.37), it is easy to see the similarity between MLA and FMCA. However, it is interesting to note the different interpretations: FMCA uses the Euclidean norm in an attempt to minimize energy, whereas MLA chooses this norm due to the Gaussian noise. In this sense, MLA is easier to generalize to other scenarios involving different noise characteristics, e.g., correlated noise or non-Gaussian noise. In principle, the MLA methodology can also be applied to other more complicated parametric models as proposed in [66, 67, 68, 69].

4.4 Small Error Analysis

In this section, we provide small error analysis for the FMCA and MLA methods. We define the real-valued parameter vector as

$$\boldsymbol{\xi} = [\boldsymbol{\phi},\ \mathrm{Re}\{\boldsymbol{\theta}^T\},\ \mathrm{Im}\{\boldsymbol{\theta}^T\}]^T, \tag{4.38}$$

where $\boldsymbol{\phi} = [\phi(1), \cdots,\ \phi(M-1)]^T$ are the autofocus phases (recall that we assumed $\phi(M) = 0$). We denote by subscripts *TRUE*, *ML* and *FMCA* the true parameters, their MLA estimates and their FMCA, MCA estimates, respectively. For simplicity, we parameterize the unknown phases using $\boldsymbol{\phi}$ instead of $\boldsymbol{\gamma}$. Furthermore, we concentrate on estimating the autofocus phase errors, $\boldsymbol{\phi}$, while treating $\boldsymbol{\theta}$ as nuisance parameters.

We begin with the discussion of the fundamental performance bound for the parameter estimation under Eqn. (4.12). The Cramer Rao bound (CRB) is a classical lower bound on the MSE of estimated parameters generated by any unbiased estimator. The CRB for the variance of the estimation error for $\boldsymbol{\xi}$ under the Gaussian model described by Eqn. (4.12) is as follows [70]:
For any unbiased estimator $\hat{\xi}_i$,

$$\mathrm{var}[\hat{\xi}_i - \xi_i] \geq [\mathbf{F}^{-1}(\boldsymbol{\xi})]_{ii}, \tag{4.39}$$

where $\mathbf{F}(\xi)$ is the Fisher information (FI) matrix described by

$$\mathbf{F}(\boldsymbol{\xi}) = \frac{2}{\sigma_n^2}\mathrm{Re}\left\{\mathbf{J}(\boldsymbol{\xi}_{\scriptscriptstyle TRUE})^H \mathbf{J}(\boldsymbol{\xi}_{\scriptscriptstyle TRUE})\right\}. \tag{4.40}$$

where $\mathbf{J}(\boldsymbol{\xi})$ is the Jacobian matrix defined as

$$\mathbf{J}(\boldsymbol{\xi}_{\scriptscriptstyle TRUE}) = \left[j\mathbf{Y}_2\mathrm{Diag}\left(e^{j\boldsymbol{\phi}_{\scriptscriptstyle TRUE}}\right),\ \mathbf{R}\left([e^{j\boldsymbol{\phi}_{\scriptscriptstyle TRUE}};1]\right)\mathbf{L},\ j\mathbf{R}\left([e^{j\boldsymbol{\phi}_{\scriptscriptstyle TRUE}};1]\right)\mathbf{L}\right], \tag{4.41}$$

with

$$\mathbf{Y} = \begin{bmatrix} e^{j\phi_{\scriptscriptstyle TRUE}(1)}\mathbf{g}_{1\ldots N} & \mathbf{0} & \cdots & \mathbf{0} \\ \mathbf{0} & e^{j\phi_{\scriptscriptstyle TRUE}(2)}\mathbf{g}_{N+1\ldots 2N} & \cdots & \mathbf{0} \\ \vdots & \vdots & \ddots & \vdots \\ \mathbf{0} & \mathbf{0} & \cdots & \mathbf{g}_{MN-N+1\ldots MN} \end{bmatrix}, \tag{4.42}$$

and $\mathbf{Y}_2$ is a matrix comprising the first to the $(M-1)$th columns of $\mathbf{Y}$.

It is a well known result that the maximum likelihood based estimator MLA attains the CRB for $\boldsymbol{\xi}$ estimation at small noise. Since FMCA and MCA only sought to estimate $\boldsymbol{\phi}$ and provide no performance guarantee for the $\boldsymbol{\theta}$ estimates, we only analyze the MSE for the MLA, FMCA and MCA phase estimator. Let $\hat{\boldsymbol{\phi}}_{ML} \in \mathbb{R}^{M-1}$ denote the MLA phase estimates for $\phi(1), \cdots, \phi(M-1)$, we can easily obtain the following:

$$\mathrm{E}\left[\left(\hat{\boldsymbol{\phi}}_{ML} - \phi_{TRUE}\right)\left(\hat{\boldsymbol{\phi}}_{ML} - \phi_{TRUE}\right)^T\right] \approx [\mathbf{F}^{-1}(\boldsymbol{\xi})]_{1:M-1,\,1:M-1}, \tag{4.43}$$

which is the top left part of the inverse FI matrix. For completeness, a short derivation of Eqn. (4.43) is included in the appendix.

Next, we analyze the MSE of the FMCA and MCA phase estimates. Recall that the FMCA and MCA estimator solves the following nonlinear least-equares problem,

$$\hat{\boldsymbol{\phi}}_{FMCA} = \underset{\boldsymbol{\phi} \in \mathbb{R}^{M-1}}{\operatorname{argmin}} \|\mathbf{f}(\boldsymbol{\phi})\|_2 \tag{4.44}$$

where

$$\mathbf{f}(\boldsymbol{\phi}) = [\mathbf{L}^{\dagger}]_a \left(\tilde{\mathbf{Y}}\, [e^{-j\boldsymbol{\phi}};\, 1]\right). \tag{4.45}$$

Its small error analysis consists of approximating $\mathbf{f}(\boldsymbol{\phi})$ by a first-order Taylor series expansion about the true parameters,

$$\mathbf{f}(\boldsymbol{\phi}) \approx \mathbf{f}(\boldsymbol{\phi}_{TRUE}) + \tilde{\mathbf{J}}_{\mathbf{f}}(\boldsymbol{\phi}_{TRUE})(\boldsymbol{\phi} - \boldsymbol{\phi}_{TRUE}), \tag{4.46}$$

where

$$\tilde{\mathbf{J}}_{\mathbf{f}}(\boldsymbol{\phi}_{TRUE}) = -j\ [\mathbf{L}^{\dagger}]_a \tilde{\mathbf{Y}}_2\ \mathrm{Diag}\left(e^{-j\boldsymbol{\phi}_{TRUE}}\right) \tag{4.47}$$

is the Jacobian matrix and $\tilde{\mathbf{Y}}_2$ is a matrix comprising the first to the $(M-1)$th columns of $\tilde{\mathbf{Y}}$. Consequently, the estimate (4.44) is approximated by

$$\hat{\boldsymbol{\phi}}_{FMCA} \approx \underset{\boldsymbol{\phi} \in \mathbb{R}^{M}}{\operatorname{argmin}} \|\mathbf{q} + \tilde{\mathbf{J}}_{\mathbf{f}}(\boldsymbol{\phi}_{TRUE})\boldsymbol{\phi}\|^2, \tag{4.48}$$

where

$$\begin{aligned}\mathbf{q} &= [\mathbf{L}^{\dagger}]_a \tilde{\mathbf{Y}}\,[e^{-j\boldsymbol{\phi}_{TRUE}};\, 1] - \tilde{\mathbf{J}}_{\mathbf{f}}(\boldsymbol{\phi}_{TRUE})\boldsymbol{\phi}_{TRUE} \\ &= [\mathbf{L}^{\dagger}]_a \mathbf{R}\left([e^{-j\boldsymbol{\phi}_{TRUE}};\, 1]\right)\tilde{\mathbf{g}} - \tilde{\mathbf{J}}_{\mathbf{f}}(\boldsymbol{\phi}_{TRUE})\boldsymbol{\phi}_{TRUE}. \end{aligned} \tag{4.49}$$

Since $\mathbf{q}$ and $\tilde{\mathbf{J}}_{\mathbf{f}}(\boldsymbol{\phi}_{TRUE})$ are complex-valued and $\boldsymbol{\phi}$ is real-valued, the solution is

$$\hat{\boldsymbol{\phi}}_{FMCA} \approx -\left[\mathrm{Re}\left\{\tilde{\mathbf{J}}_{\mathbf{f}}^{H}(\boldsymbol{\phi}_{TRUE})\tilde{\mathbf{J}}_{\mathbf{f}}(\boldsymbol{\phi}_{TRUE})\right\}\right]^{-1}\mathrm{Re}\{\tilde{\mathbf{J}}_{\mathbf{f}}^{H}(\boldsymbol{\phi}_{TRUE})\mathbf{q}\}. \tag{4.50}$$

Substituting Eqn. (4.49) into Eqn. (4.50) yields

$$\hat{\boldsymbol{\phi}}_{FMCA} - \hat{\boldsymbol{\phi}}_{TRUE} = -\mathbf{A}^{-1}\mathbf{b}, \tag{4.51}$$

where

$$\mathbf{A} = \mathrm{Re}\left\{\tilde{\mathbf{J}}_{\mathbf{f}}^{H}(\boldsymbol{\phi}_{TRUE})\tilde{\mathbf{J}}_{\mathbf{f}}(\boldsymbol{\phi}_{TRUE})\right\} \tag{4.52}$$

$$\mathbf{b} = \mathrm{Re}\left\{\tilde{\mathbf{J}}_{\mathbf{f}}^{H}(\boldsymbol{\phi}_{TRUE})[\mathbf{L}^{\dagger}]_a \mathbf{R}\left([e^{-j\boldsymbol{\phi}_{TRUE}};\, 1]\right)\tilde{\mathbf{g}}\right\}. \tag{4.53}$$

Next, we will try to simplify Eqn. (4.51). First, by explicitly writing out the signal term and the random noise term for $\tilde{\mathbf{Y}}$:

$$\tilde{\mathbf{Y}} = \mathbf{Y} + \mathbf{W}, \tag{4.54}$$

where

$$\mathbf{W} == \begin{bmatrix} \mathbf{n}_{1\ldots N} & \mathbf{0} & \cdots & \mathbf{0} \\ \mathbf{0} & \mathbf{n}_{N+1\ldots 2N} & \cdots & \mathbf{0} \\ \vdots & \vdots & \ddots & \vdots \\ \mathbf{0} & \mathbf{0} & \cdots & \mathbf{n}_{MN-N+1\ldots MN} \end{bmatrix}, \tag{4.55}$$

and observing that the low-return region constraint ensures that

$$[\mathbf{L}^{\dagger}]_a \mathbf{R}\left([e^{-j\boldsymbol{\phi}_{TRUE}};\ 1]\right)\mathbf{g} = \mathbf{0}, \tag{4.56}$$

equation (4.51) is reduced to

$$\hat{\boldsymbol{\phi}}_{FMCA} - \boldsymbol{\phi}_{TRUE} \ \approx\ -\left[\mathrm{Re}\left\{\mathbf{J}_{\mathbf{f}}(\boldsymbol{\phi}_{TRUE})^H \mathbf{J}_{\mathbf{f}}(\boldsymbol{\phi}_{TRUE})\right\}\right]^{-1}\left(\underline{\mathbf{J}}_{\mathbf{Y}} + \underline{\mathbf{J}}_{\mathbf{W}}\right)^T \underline{\mathbf{L}}\ \underline{\mathbf{W}}, \tag{4.57}$$

where

$$\begin{aligned}
\underline{\mathbf{W}} &= \begin{bmatrix} \mathrm{Re}\{\mathbf{W}\ [e^{-j\boldsymbol{\phi}_{TRUE}};\ 1]\} \\ \mathrm{Im}\{\mathbf{W}\ [e^{-j\boldsymbol{\phi}_{TRUE}};\ 1]\} \end{bmatrix} \\
\underline{\mathbf{L}} &= \begin{bmatrix} \mathrm{Re}\{[\mathbf{L}^{\dagger}]_a\} & -\mathrm{Im}\{[\mathbf{L}^{\dagger}]_a\} \\ \mathrm{Im}\{[\mathbf{L}^{\dagger}]_a\} & \mathrm{Re}\{[\mathbf{L}^{\dagger}]_a\} \end{bmatrix} \\
\underline{\mathbf{J}}_{\mathbf{Y}} &= \begin{bmatrix} \mathrm{Re}\{-j\ [\mathbf{L}^{\dagger}]_a \mathbf{Y}_2\ \mathrm{Diag}\left(e^{-j\boldsymbol{\phi}_{TRUE}}\right)\} \\ \mathrm{Im}\{-j\ [\mathbf{L}^{\dagger}]_a \mathbf{Y}_2\ \mathrm{Diag}\left(e^{-j\boldsymbol{\phi}_{TRUE}}\right)\} \end{bmatrix} \\
\underline{\mathbf{J}}_{\mathbf{W}} &= \begin{bmatrix} \mathrm{Re}\{-j\ [\mathbf{L}^{\dagger}]_a \mathbf{W}_2\ \mathrm{Diag}\left(e^{-j\boldsymbol{\phi}_{TRUE}}\right)\} \\ \mathrm{Im}\{-j\ [\mathbf{L}^{\dagger}]_a \mathbf{W}_2\ \mathrm{Diag}\left(e^{-j\boldsymbol{\phi}_{TRUE}}\right)\} \end{bmatrix},
\end{aligned} \tag{4.58}$$

and $\mathbf{W}_2$ is the first to $(M-1)$th columns of $\mathbf{W}$. By ignoring the second order noise term, Eqn. (4.57) can be further approximated as

$$\hat{\boldsymbol{\phi}}_{FMCA} - \boldsymbol{\phi}_{TRUE} \ \approx\ -\left[\mathrm{Re}\left\{\mathbf{J}_{\mathbf{f}}(\boldsymbol{\phi}_{TRUE})^H \mathbf{J}_{\mathbf{f}}(\boldsymbol{\phi}_{TRUE})\right\}\right]^{-1} \underline{\mathbf{J}}_{\mathbf{Y}}^T \underline{\mathbf{L}}\ \underline{\mathbf{W}}. \tag{4.59}$$

Next step is to simplify the inverse matrix term in Eqn. (4.59) where it can be expressed as:

$$\begin{aligned}
&\left[\mathrm{Re}\left\{\mathbf{J_f}(\boldsymbol{\phi}_{\scriptscriptstyle TRUE})^H \mathbf{J_f}(\boldsymbol{\phi}_{\scriptscriptstyle TRUE})\right\}\right]^{-1} \\
&= \Big[\mathrm{Re}\left\{\mathbf{J}_{\mathbf{Y}}^H \mathbf{J}_{\mathbf{Y}}\right\} + \mathrm{Re}\left\{\mathbf{J}_{\mathbf{Y}}^H \mathbf{J}_{\mathbf{W}} + \mathbf{J}_{\mathbf{W}}^H \mathbf{J}_{\mathbf{Y}} + \mathbf{J}_{\mathbf{W}}^H \mathbf{J}_{\mathbf{W}}\right\}\Big]^{-1},
\end{aligned} \tag{4.60}$$

where

$$\begin{aligned}
\mathbf{J}_{\mathbf{Y}} &= -j\ [\mathbf{L}^{\dagger}]_a \mathbf{Y}_2\ \mathrm{Diag}\left(e^{-j\boldsymbol{\phi}_{\scriptscriptstyle TRUE}}\right) \\
\mathbf{J}_{\mathbf{W}} &= -j\ [\mathbf{L}^{\dagger}]_a \mathbf{W}_2\ \mathrm{Diag}\left(e^{-j\boldsymbol{\phi}_{\scriptscriptstyle TRUE}}\right).
\end{aligned} \tag{4.61}$$

Since we are assuming small noise for the MSE analysis, i.e., small $\mathbf{W}$, it is well known that Eqn. (4.60) can be approximated by the following:

$$\begin{aligned}
&\left[\mathrm{Re}\left\{\mathbf{J_f}(\boldsymbol{\phi}_{\scriptscriptstyle TRUE})^H \mathbf{J_f}(\boldsymbol{\phi}_{\scriptscriptstyle TRUE})\right\}\right]^{-1} \\
&\approx \Big[\mathrm{Re}\left\{\mathbf{J}_{\mathbf{Y}}^H \mathbf{J}_{\mathbf{Y}}\right\}\Big]^{-1} - \Bigg(\Big[\mathrm{Re}\left\{\mathbf{J}_{\mathbf{Y}}^H \mathbf{J}_{\mathbf{Y}}\right\}\Big]^{-1} \cdot \\
&\quad \Big[\mathrm{Re}\left\{\mathbf{J}_{\mathbf{Y}}^H \mathbf{J}_{\mathbf{W}} + \mathbf{J}_{\mathbf{W}}^H \mathbf{J}_{\mathbf{Y}} + \mathbf{J}_{\mathbf{W}}^H \mathbf{J}_{\mathbf{W}}\right\}\Big]\Big[\mathrm{Re}\left\{\mathbf{J}_{\mathbf{Y}}^H \mathbf{J}_{\mathbf{Y}}\right\}\Big]^{-1}\Bigg).
\end{aligned} \tag{4.62}$$

By further approximate Eqn. (4.59) using Eqn. (4.62) and ignoring second order noise term, we obtain

$$\hat{\boldsymbol{\phi}}_{\scriptscriptstyle FMCA} - \boldsymbol{\phi}_{\scriptscriptstyle TRUE} \ \approx\ \Big[\mathrm{Re}\left\{\mathbf{J}_{\mathbf{Y}}^H \mathbf{J}_{\mathbf{Y}}\right\}\Big]^{-1} \underline{\mathbf{J}}_{\mathbf{Y}}^T \underline{\mathbf{L}}\ \underline{\mathbf{W}}. \tag{4.63}$$

And finally, we have

$$\begin{aligned}
&\mathrm{E}\left[\left(\hat{\boldsymbol{\phi}}_{\scriptscriptstyle FMCA}-\boldsymbol{\phi}_{\scriptscriptstyle TRUE}\right)\left(\hat{\boldsymbol{\phi}}_{\scriptscriptstyle FMCA}-\boldsymbol{\phi}_{\scriptscriptstyle TRUE}\right)^{T}\right] \\
&\approx \mathrm{E}\left[\left[\mathrm{Re}\left\{\mathbf{J}_{\mathbf{Y}}^{H}\mathbf{J}_{\mathbf{Y}}\right\}\right]^{-1}\underline{\mathbf{J}}_{\mathbf{Y}}^{T}\underline{\mathbf{L}}\;\underline{\mathbf{W}}\;\underline{\mathbf{W}}^{T}\underline{\mathbf{L}}^{T}\underline{\mathbf{J}}_{\mathbf{Y}}\left[\mathrm{Re}\left\{\mathbf{J}_{\mathbf{Y}}^{H}\mathbf{J}_{\mathbf{Y}}\right\}\right]^{-1}\right] \\
&= \left[\mathrm{Re}\left\{\mathbf{J}_{\mathbf{Y}}^{H}\mathbf{J}_{\mathbf{Y}}\right\}\right]^{-1}\underline{\mathbf{J}}_{\mathbf{Y}}^{T}\underline{\mathbf{L}}\;\mathrm{E}\left[\underline{\mathbf{W}}\;\underline{\mathbf{W}}^{T}\right]\underline{\mathbf{L}}^{T}\underline{\mathbf{J}}_{\mathbf{Y}}\left[\mathrm{Re}\left\{\mathbf{J}_{\mathbf{Y}}^{H}\mathbf{J}_{\mathbf{Y}}\right\}\right]^{-1} \\
&= \frac{\sigma_n^2}{2}\cdot\left[\mathrm{Re}\left\{\mathbf{J}_{\mathbf{Y}}^{H}\mathbf{J}_{\mathbf{Y}}\right\}\right]^{-1}\underline{\mathbf{J}}_{\mathbf{Y}}^{T}\underline{\mathbf{L}}\;\underline{\mathbf{L}}^{T}\underline{\mathbf{J}}_{\mathbf{Y}}\left[\mathrm{Re}\left\{\mathbf{J}_{\mathbf{Y}}^{H}\mathbf{J}_{\mathbf{Y}}\right\}\right]^{-1}.
\end{aligned} \tag{4.64}$$

Now, we can compare the MSE of MLA phase estimation in Eqn. (4.43), which is also the CRB, with the MSE of FMCA phase estimation in Eqn. (4.64). The errors are plotted in Fig. 4.1 where it is easy to see that FMCA is significantly more sensitive to noise. We validated this small error analysis using Monte-Carlo simulation of the estimators. The setup for this simulation was: $\boldsymbol{\theta}$ was a $D = 100$ dimensional random uniformly distributed complex vector, $\boldsymbol{\phi}$ was independent and uniformly distributed between $-\pi$ and π except for $\phi_M = 0$. Sampling matrix $\mathbf{L}$ was generated by using an imaging scenario where the SAR operated across a 1 degree look angle and transmitted 15 pulses (M = 15). The receiver provided 15 samples per single pulse (N = 15). We applied a rectangular antenna pattern on $\boldsymbol{\theta}$ so that it was known a priori that $\theta_a = 0$ for $a = \{1, \cdots, 10,\ 91, \cdots, 100\}$. The additive noise was complex gaussian with signal-to-noise-ration (SNR) defined as

$$\mathrm{SNR} = 20\log_{10}\left(\frac{1}{\sigma_n MN}\sum_{m,n}|\tilde{\mathrm{G}}[m,n]|\right). \tag{4.65}$$

The experimental results plotted in Fig. 4.1 used SDR to solve both the MLA and FMCA phase estimation problems described by Eqn. (4.36) and Eqn. (4.37), respectively.

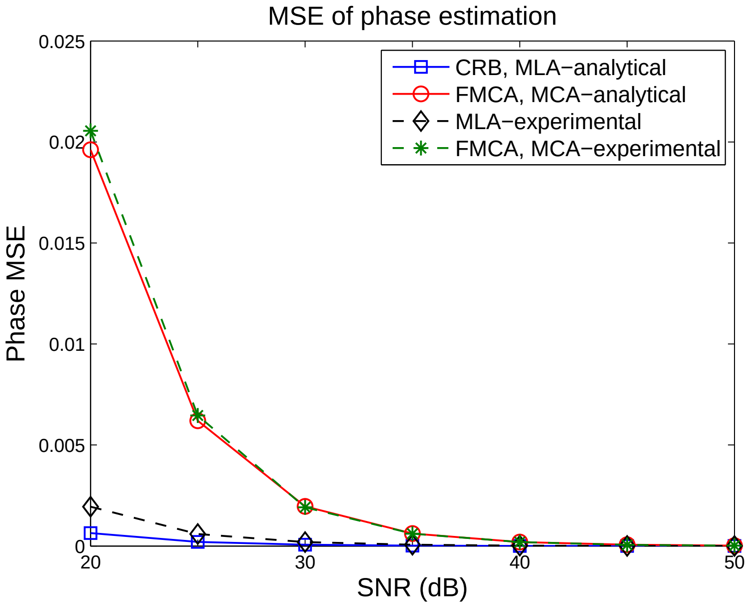

Figure 4.1: MSE for MLA phase estimation compared with FMCA and MCA phase estimation under small noise (y axis shows $\frac{1}{M-1}\sum_i(\hat{\phi}(i) - \phi_{TRUE}(i))^2$).

4.5 Simulation Results

In this section, we present numerical results to illustrate the advantages of our proposed methods in realistic SAR systems.

4.5.1 SAR Simulator

In order to test the different algorithms, we built a SAR simulator based on the bilinear model described in Section 4.1. The amplitudes of $\boldsymbol{\theta}$ were taken from actual SAR images, whereas the phases of $\boldsymbol{\theta}$ were independently generated according to to a uniform distribution between $-\pi$ and π (not to be confused with the autofocus phase error). We adopted the impulse model with $dx = dy = 1$ for our simulation. The nuisance autofocus phases were also independently generated according to a uniform distribution. Note that this distribution is known to be the most challenging phase corruption. Subsequent figures present the magnitude of the complex reconstructed reflectivity functions (which are the magnitudes of $\boldsymbol{\theta}$ in the impulse model).

4.5.2 Performance of MLA

First we start with showing the full strength of MLA by comparing it with PGA and sharpness-maximization methods. Hereafter, MLA was implemented with SDR using the interior-point method developed in [35]. A SAR image, shown in Fig. 4.2(a), was obtained from Sandia National Laboratory. We examined two scenarios: in the first scenario, the hypothetical SAR operated across a 0.2 degree look angle which falls into the small-angle category; in the second scenario, the SAR radar operated across a 2 degree look angle. For both scenarios the radar transmitted 50 pulses ($M = 50$) and the receiver provided 50 samples per single pulse ($N = 50$). No prior information about the image was used by the MLA estimator, i.e., MLA considered the image to be arbitrary. For the sharpness maximization method, we used negative entropy as the sharpness metric. The perfectly focused image with additive noise of SNR=10dB is shown in Fig. 4.2(a). Because no low-return region can be found, FMCA can not be applied here. Phase corrupted image is shown 4.2(b).

Image restoration for the first scenario is shown in Fig. 4.4. The MLA reconstructed image for SNR=10dB is shown in Fig. 4.4(a) with a phase MSE of 0.0108. The MLA reconstructed image for SNR=5dB is shown in Fig. 4.4(b) with a phase MSE of 0.0771. The PGA image restoration for SNR=10dB and SNR=5dB are shown in Figs. 4.4(c) and (d), respectively. The sharpness maximization method image restoration for SNR=10dB and SNR=5dB are shown in Figs. 4.4(e) and (f) with phase MSE 0.8837 and 0.9153, respectively. Note that, since PGA only produces a reconstructed image, no phase MSE is computed.

Image restoration for the second scenario is shown in Fig. 4.5. The MLA reconstructed image for SNR=10dB is shown in Fig. 4.5(a) with a phase MSE of 0.0148. The MLA reconstructed image for SNR=5dB is shown in Fig. 4.5(b) with a phase MSE of 0.1728. The PGA image restoration for SNR=10dB and SNR=5dB are shown in Figs. 4.5(c) and (d), respectively. The sharpness maximization method image restoration for

SNR=10dB and SNR=5dB are shown in Figs. 4.5(e) and (f) with phase MSE 0.7815 and 0.9346, respectively.

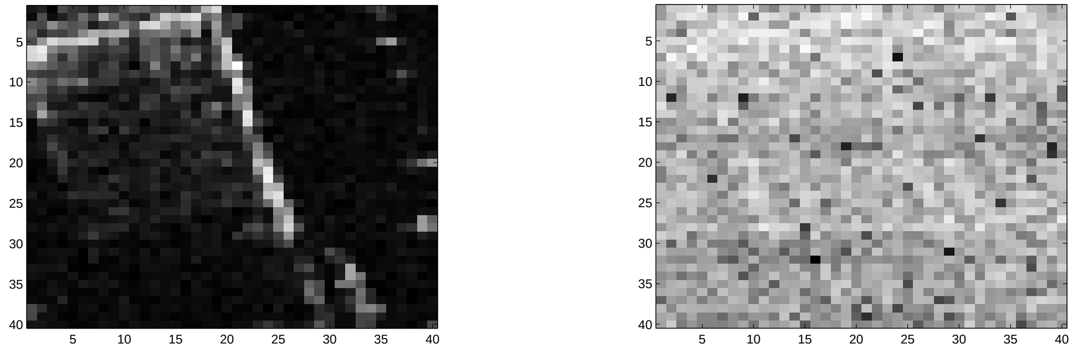

(a)

(b)

Figure 4.2: SAR image with SNR=10dB: (a) Focused image; (b) defocused image using an *i.i.d.* phase error.

4.5.3 Comparison of MLA with FMCA

In the next set of experiments, we compared MLA with FMCA. We adopted a SAR scenario with a wide range of look angles, which is more challenging than the narrow range of look angles considered earlier. We used a SAR image obtained from the MSTAR SAR database [71]. The focused image is shown in Fig. 4.6(a). We applied a rectangular antenna pattern to the image so that the first and last column were zero, i.e., a known index set a that indexes the low-return region was known *a priori* to FMCA so that $\theta_a = 0$. For MLA, the set a effectively reduced the dimension for $\boldsymbol{\theta}$. Note that knowledge of the antenna pattern (low-return region) is required only by FMCA, not MLA. We adopted an imaging scenario where the radar was collecting data across 6 degrees and the radar transmitted 80 pulses ($M = 80$) and the receiver provided 80 samples per single pulse ($N = 80$). The phase corrupted image is shown in Fig. 4.6(b). The images restored by MLA for SNR=10dB and SNR=5dB are shown in Figs. 4.6(c) and (d) with phase MSE equal to 0.3697 and 0.5521, respectively. The

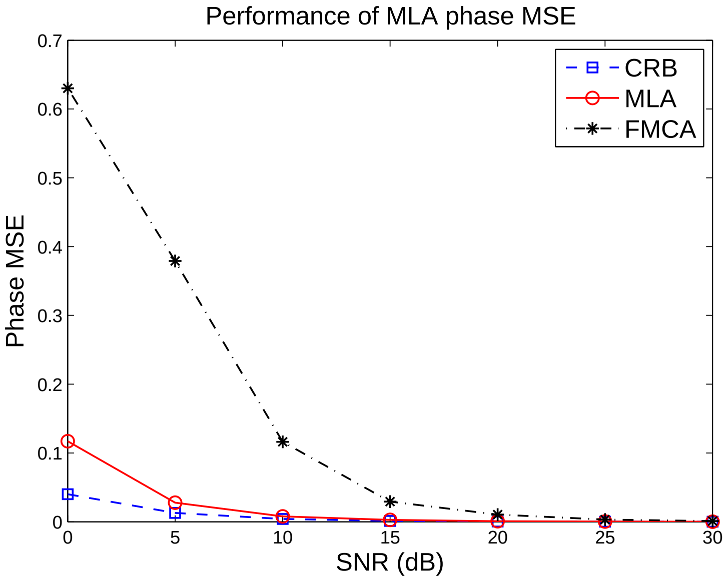

Figure 4.3: Phase MSE of MLA compared with FMCA and CRB.

images restored by FMCA for SNR=10dB and SNR=5dB are shown in Figs. 4.6(e) and (f) with phase MSE equal to 0.6690 and 0.8723, respectively.

Next, Figure 4.3 shows a Monte-Carlo simulation for the phase MSE of MLA compared with FMCA and the Cramer-Rao bound (CRB). A 10×10 toy image was used in this part of the simulations with SAR collecting data across 10 degree look angles and the radar transmitted 15 pulses ($M = 15$) and the receiver provided 15 samples per single pulse ($N = 15$).

4.5.4 Robustness Against Model Mismatching

In this last set of experiments, we examine the robustness of MLA against model mismatching. MLA is derived from the proposed parametric model and we have analytically and experimentally demonstrated its advantages under the proposed model. However, FMCA does not explicitly assume such a model and it is important to investigate the performance of MLA when there is a model mismatch. We continue with a similar setup and the estimators are implemented as before. However, the SAR simulator no longer uses the naive impulse basis functions in (4.2) but replaces them with more realistic functions:

$$h_i(x, y) = k\left(x - u_i,\ y - v_i\right). \tag{4.66}$$

This has the effect of further corrupting the collected Fourier data in the following way:

$$\mathrm{G}'[m, n] = \mathrm{G}[m, n] \cdot \mathrm{K}(F_x[m, n], F_y[m, n]), \tag{4.67}$$

where G' denote the actual collected data and K denotes the Fourier transform of the kernel function k. The autofocus algorithms are not aware of this setup and mistakenly compute $\mathbf{L}$ using the model in (4.2).

First, we adopted a rectangular kernel

$$k(x, y) = \begin{cases} 1 & , |x| < 1 \text{ and } |y| < 1 \\ 0 & , \text{otherwise} \end{cases}. \tag{4.68}$$

This illustrates a model where there is a constant reflectivity within a resolution cell instead of an impulse located at the center of the cell. The focused image formed using the exact model and mismatched model is shown in Figs. 4.7(a) and (b), respectively. The image restored by MLA and FMCA for the model mismatched image are shown in Figs. 4.7(c) and (d), respectively. The autofocus phase error was an *i.i.d.* function and SNR=5dB.

Second, we adopted a 2-D Gaussian kernel with

$$k(x, y) = e^{-\left(\frac{x^2}{2} + \frac{y^2}{2}\right)}, \tag{4.69}$$

This illustrates a model where the sum of reflectivity within a resolution cell also affects neighboring cells. The focused image formed by the exact and mismatched models are shown in Figs. 4.8(a) and (b), respectively. The image restored by MLA and FMCA for the model mismatched data are shown in Figs. 4.8(c) and (d), respectively. The autofocus phase error was an *i.i.d.* function and SNR=5dB.

From the above simulations we can see that MLA can outperform FMCA even when there is model mismatching.

4.6 Chapter Summary

In this Chapter, we considered the problem of SAR autofocus based on a bilinear parametric model. We derived the MLA framework and compared it to previous methods. Under simplistic conditions, MLA coincides with the successful MCA technique. In more realistic conditions, MLA outperforms FMCA, and is applicable to a broader class of scenarios.

4.7 Appendix

Here we will analyze the MSE for the MLA estimator in the small noise case. Recall from Eqn. (4.33) that the MLA estimator is the following

$$\hat{\boldsymbol{\xi}}_{ML} = \underset{\boldsymbol{\xi}\in[\mathbb{R}^{2D+M-1}]}{\operatorname{argmin}} \left\|\mathbf{m}(\boldsymbol{\xi})\right\|_2 \tag{4.70}$$

where

$$\mathbf{m}(\boldsymbol{\xi}) = \mathbf{R}(\boldsymbol{\gamma}_{TRUE})\mathbf{L}\boldsymbol{\theta}_{TRUE} - \mathbf{R}(\boldsymbol{\gamma})\mathbf{L}\boldsymbol{\theta} + \mathbf{n}. \tag{4.71}$$

Assuming small noise and approximate $\mathbf{m}(\boldsymbol{\xi})$ by first order Taylor expansion around $\boldsymbol{\xi}_{TRUE}$:

$$\mathbf{m}(\boldsymbol{\xi}) \;\approx\; \mathbf{m}(\boldsymbol{\xi}_{TRUE}) + \mathbf{J}(\boldsymbol{\xi}_{TRUE})(\boldsymbol{\xi} - \boldsymbol{\xi}_{TRUE}) \tag{4.72}$$

where $\mathbf{J}(\boldsymbol{\xi}_{TRUE})$ is the Jacobian matrix described by equation (4.47). Using Eqn. (4.72), the MLA estimator can be approximated by

$$\begin{aligned}\hat{\boldsymbol{\xi}}_{ML} &\approx \underset{\boldsymbol{\xi}\in[\mathbb{R}^{2D+M-1}]}{\operatorname{argmin}} \|\mathbf{y} + \mathbf{J}(\boldsymbol{\xi}_{TRUE})\boldsymbol{\xi}\|_2 \\ &= -\mathbf{J}^{\dagger}(\boldsymbol{\xi}_{TRUE})\,\mathbf{y} \qquad (4.73)\end{aligned}$$

where

$$\mathbf{y} = \mathbf{m}(\boldsymbol{\xi}_{TRUE}) - \mathbf{J}(\boldsymbol{\xi}_{TRUE})\boldsymbol{\xi}_{TRUE}. \qquad (4.74)$$

Substitute Eqn. (4.74) back into Eqn. (4.73) and we have

$$\begin{aligned}&\hat{\boldsymbol{\xi}}_{ML} - \boldsymbol{\xi}_{TRUE} \;\approx\; -\mathbf{J}^{\dagger}(\boldsymbol{\xi}_{TRUE})\mathbf{m}(\boldsymbol{\xi}_{TRUE}) \\ \Rightarrow &\hat{\boldsymbol{\xi}}_{ML} - \boldsymbol{\xi}_{TRUE} \approx -\mathbf{J}^{\dagger}(\boldsymbol{\xi}_{TRUE})\Big(\mathbf{R}(\boldsymbol{\gamma}_{TRUE})\mathbf{L}\boldsymbol{\theta}_{TRUE} - \mathbf{R}(\boldsymbol{\gamma}_{TRUE})\mathbf{L}\boldsymbol{\theta}_{TRUE} + \mathbf{n}\Big). \\ \Rightarrow &\hat{\boldsymbol{\xi}}_{ML} - \boldsymbol{\xi}_{TRUE} \approx -\mathbf{J}^{\dagger}(\boldsymbol{\xi}_{TRUE})\,\mathbf{n}. \qquad (4.75)\end{aligned}$$

First step is to transform the complex number MSE expression in Eqn. (4.75) into a real number expression. Let

$$\underline{\mathbf{J}}(\boldsymbol{\xi}) = \begin{bmatrix} \mathrm{Re}\{\mathbf{J}(\boldsymbol{\xi})\} \\ \mathrm{Im}\{\mathbf{J}(\boldsymbol{\xi})\} \end{bmatrix}, \quad \underline{\mathbf{n}} = \begin{bmatrix} \mathrm{Re}\{\mathbf{n}\} \\ \mathrm{Im}\{\mathbf{n}\} \end{bmatrix} \qquad (4.76)$$

and we have

$$\begin{aligned}\mathrm{E}\left[\left(\hat{\boldsymbol{\xi}}_{ML} - \boldsymbol{\xi}_{TRUE}\right)\left(\hat{\boldsymbol{\xi}}_{ML} - \boldsymbol{\xi}_{TRUE}\right)^T\right] &\approx \mathrm{E}\left[\underline{\mathbf{J}}^{\dagger}(\boldsymbol{\xi}_{TRUE})\underline{\mathbf{n}}\underline{\mathbf{n}}^T\underline{\mathbf{J}}^{\dagger}(\boldsymbol{\xi}_{TRUE})^T\right] \\ &\approx \underline{\mathbf{J}}^{\dagger}(\boldsymbol{\xi}_{TRUE})\mathrm{E}\left[\underline{\mathbf{n}}\underline{\mathbf{n}}^T\right]\underline{\mathbf{J}}^{\dagger}(\boldsymbol{\xi}_{TRUE})^T \qquad (4.77)\end{aligned}$$

Since

$$\mathrm{E}\left[\mathrm{Re}\{\mathbf{n}\}\mathrm{Re}\{\mathbf{n}\}^T\right] = \mathrm{E}\left[\mathrm{Im}\{\mathbf{n}\}\mathrm{Im}\{\mathbf{n}\}^T\right] = \frac{\sigma_n^2}{2}\cdot\mathbf{I}$$
$$\mathrm{E}\left[\mathrm{Re}\{\mathbf{n}\}\mathrm{Im}\{\mathbf{n}\}^T\right] = \mathrm{E}\left[\mathrm{Im}\{\mathbf{n}\}\mathrm{Re}\{\mathbf{n}\}^T\right] = \mathbf{0}, \tag{4.78}$$

equation (4.77) is qual to

$$\mathrm{E}\left[\left(\hat{\boldsymbol{\xi}}_{ML}-\boldsymbol{\xi}_{TRUE}\right)\left(\hat{\boldsymbol{\xi}}_{ML}-\boldsymbol{\xi}_{TRUE}\right)^T\right]$$
$$\frac{\sigma_n^2}{2}\cdot \approx \left[\underline{\mathbf{J}}(\boldsymbol{\xi}_{TRUE})^T\underline{\mathbf{J}}(\boldsymbol{\xi}_{TRUE})\right]^{\dagger}\underline{\mathbf{J}}(\boldsymbol{\xi}_{TRUE})^T\underline{\mathbf{J}}(\boldsymbol{\xi}_{TRUE})[\underline{\mathbf{J}}(\boldsymbol{\xi}_{TRUE})^T\underline{\mathbf{J}}(\boldsymbol{\xi}_{TRUE})]^{\dagger} \tag{4.79}$$

From problem formulation, $\underline{\mathbf{J}}(\boldsymbol{\xi}_{TRUE})^T\underline{\mathbf{J}}(\boldsymbol{\xi}_{TRUE})$ is non-singular. Thus,

$$\left[\underline{\mathbf{J}}(\boldsymbol{\xi}_{TRUE})^T\underline{\mathbf{J}}(\boldsymbol{\xi}_{TRUE})\right]^{\dagger} = \left[\underline{\mathbf{J}}(\boldsymbol{\xi}_{TRUE})^T\underline{\mathbf{J}}(\boldsymbol{\xi}_{TRUE})\right]^{-1}. \tag{4.80}$$

Equation (4.79) continues as

$$\mathrm{E}\left[\left(\hat{\boldsymbol{\xi}}_{ML}-\boldsymbol{\xi}_{TRUE}\right)\left(\hat{\boldsymbol{\xi}}_{ML}-\boldsymbol{\xi}_{TRUE}\right)^T\right] \approx \frac{\sigma_n^2}{2}\cdot\left[\underline{\mathbf{J}}(\boldsymbol{\xi}_{TRUE})^T\underline{\mathbf{J}}(\boldsymbol{\xi}_{TRUE})\right]^{-1}. \tag{4.81}$$

Note that

$$\underline{\mathbf{J}}(\boldsymbol{\xi}_{TRUE})^T\underline{\mathbf{J}}(\boldsymbol{\xi}_{TRUE}) = \mathrm{Re}\left\{\mathbf{J}(\boldsymbol{\xi}_{TRUE})^H\mathbf{J}(\boldsymbol{\xi}_{TRUE})\right\}, \tag{4.82}$$

and we have the following desired expression for the MLA phase MSE

$$\mathrm{E}\left[\left(\hat{\boldsymbol{\xi}}_{ML}-\boldsymbol{\xi}_{TRUE}\right)\left(\hat{\boldsymbol{\xi}}_{ML}-\boldsymbol{\xi}_{TRUE}\right)^T\right] \approx \frac{\sigma_n^2}{2}\cdot\left[\mathrm{Re}\left\{\mathbf{J}(\boldsymbol{\xi}_{TRUE})^H\mathbf{J}(\boldsymbol{\xi}_{TRUE})\right\}\right]^{-1}. \tag{4.83}$$

Since

$$\hat{\boldsymbol{\phi}}_{ML}-\boldsymbol{\phi}_{TRUE} = \mathbf{D}\ \left(\hat{\boldsymbol{\xi}}_{ML}-\boldsymbol{\xi}_{TRUE}\right) \tag{4.84}$$

where

$$\mathbf{D} = \begin{bmatrix} \mathbf{I}_{M-1} & \mathbf{0} \\ \mathbf{0} & \mathbf{0} \end{bmatrix}, \tag{4.85}$$

we have

$$\begin{aligned} \mathrm{E}\left[\left(\hat{\boldsymbol{\phi}}_{\scriptscriptstyle ML} - \boldsymbol{\phi}_{\scriptscriptstyle TRUE}\right)\left(\hat{\boldsymbol{\phi}}_{\scriptscriptstyle ML} - \boldsymbol{\phi}_{\scriptscriptstyle TRUE}\right)^T\right] &\approx \frac{\sigma_n^2}{2} \cdot \mathbf{D}\left[\mathrm{Re}\left\{\mathbf{J}(\boldsymbol{\xi}_{\scriptscriptstyle TRUE})^H \mathbf{J}(\boldsymbol{\xi}_{\scriptscriptstyle TRUE})\right\}\right]^{-1}\mathbf{D} \\ &= \frac{\sigma_n^2}{2} \cdot \left[\mathrm{Re}\left\{\mathbf{J}(\boldsymbol{\xi}_{\scriptscriptstyle TRUE})^H \mathbf{J}(\boldsymbol{\xi}_{\scriptscriptstyle TRUE})\right\}\right]^{-1}_{1:M-1,1:M-1} \end{aligned} \tag{4.86}$$

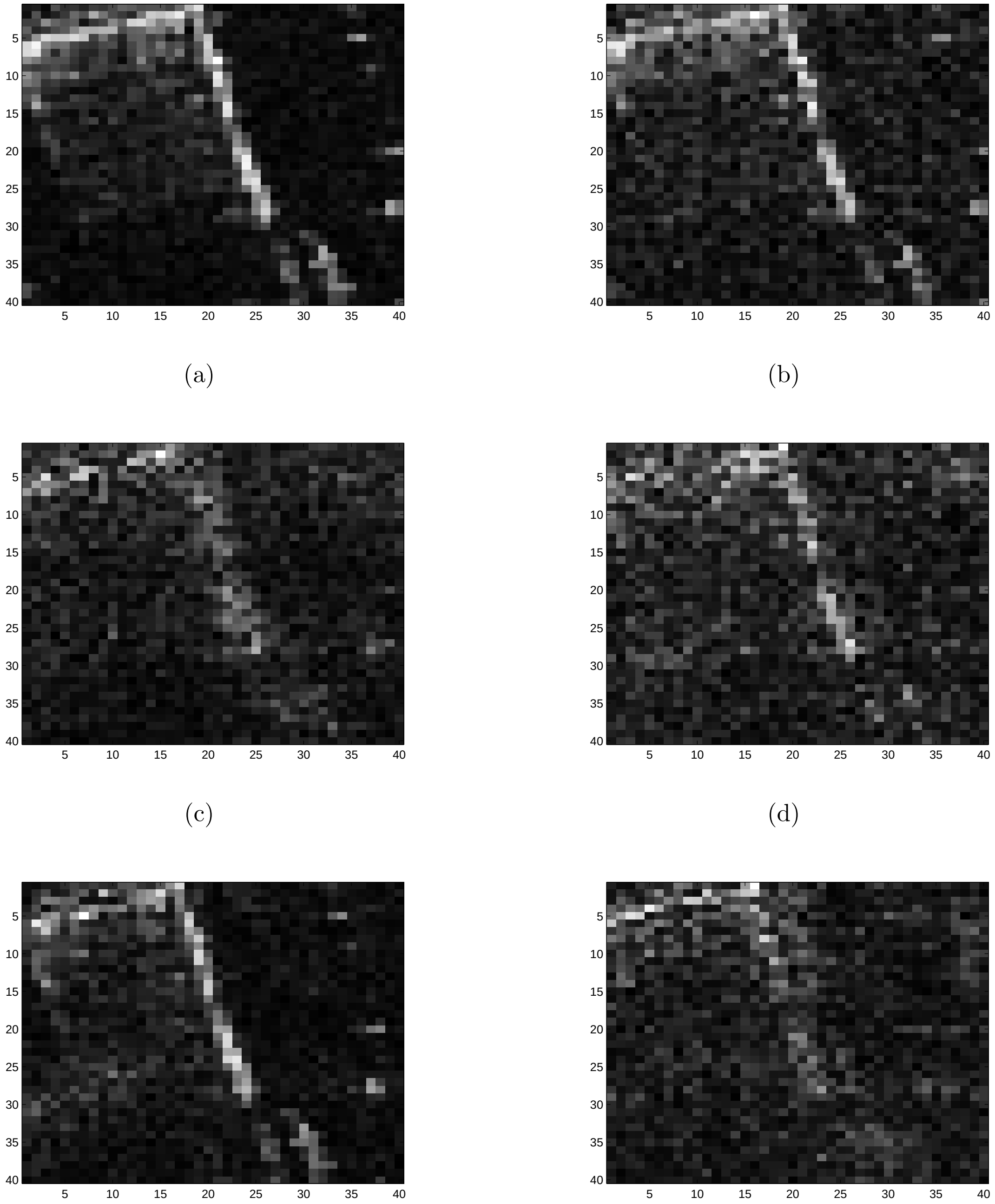

(a) (b)

(c) (d)

(e) (f)

Figure 4.4: Image restoration for 0.2 degree look angle: (a) MLA restoration for SNR=10dB (phase MSE=0.0108); (b) MLA restoration for SNR=5dB (phase MSE=0.0771); (c) PGA restoration for SNR=10dB; (d) PGA restoration for SNR=5dB; (e) Sharpness maximization restoration for SNR=10dB (phase MSE=0.8837); (f) Sharpness maximization restoration for SNR=5dB (phase MSE=0.9153).

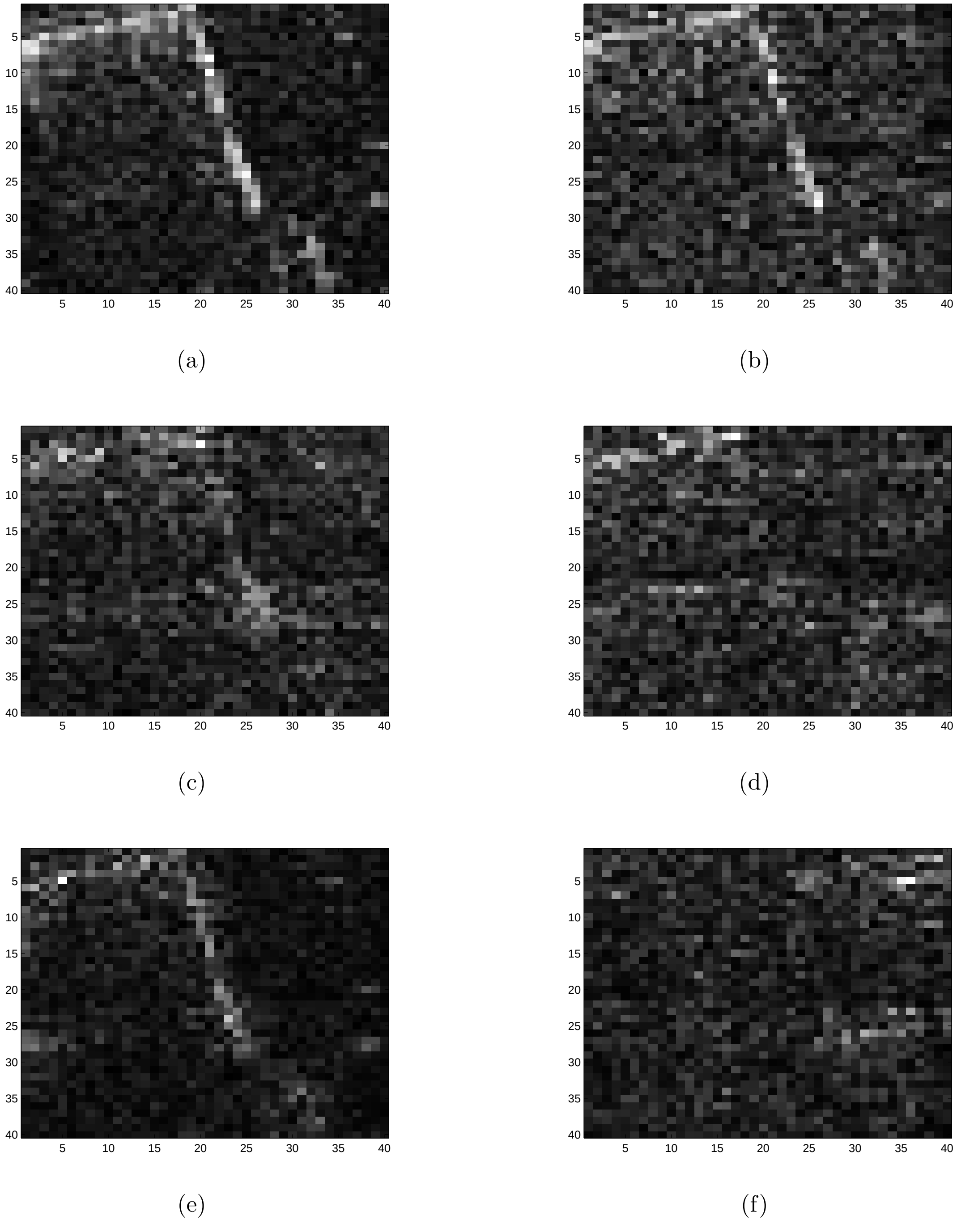

(a) (b)

(c) (d)

(e) (f)

Figure 4.5: Image restoration for 2 degree look angle: (a) MLA restoration for SNR=10dB (phase MSE=0.0148); (b) MLA restoration for SNR=5dB (phase MSE=0.1728); (c) PGA restoration for SNR=10dB; (d) PGA restoration for SNR=5dB; (e) Sharpness maximization restoration for SNR=10dB (phase MSE=0.7815); (f) Sharpness maximization restoration for SNR=5dB (phase MSE=0.9346).

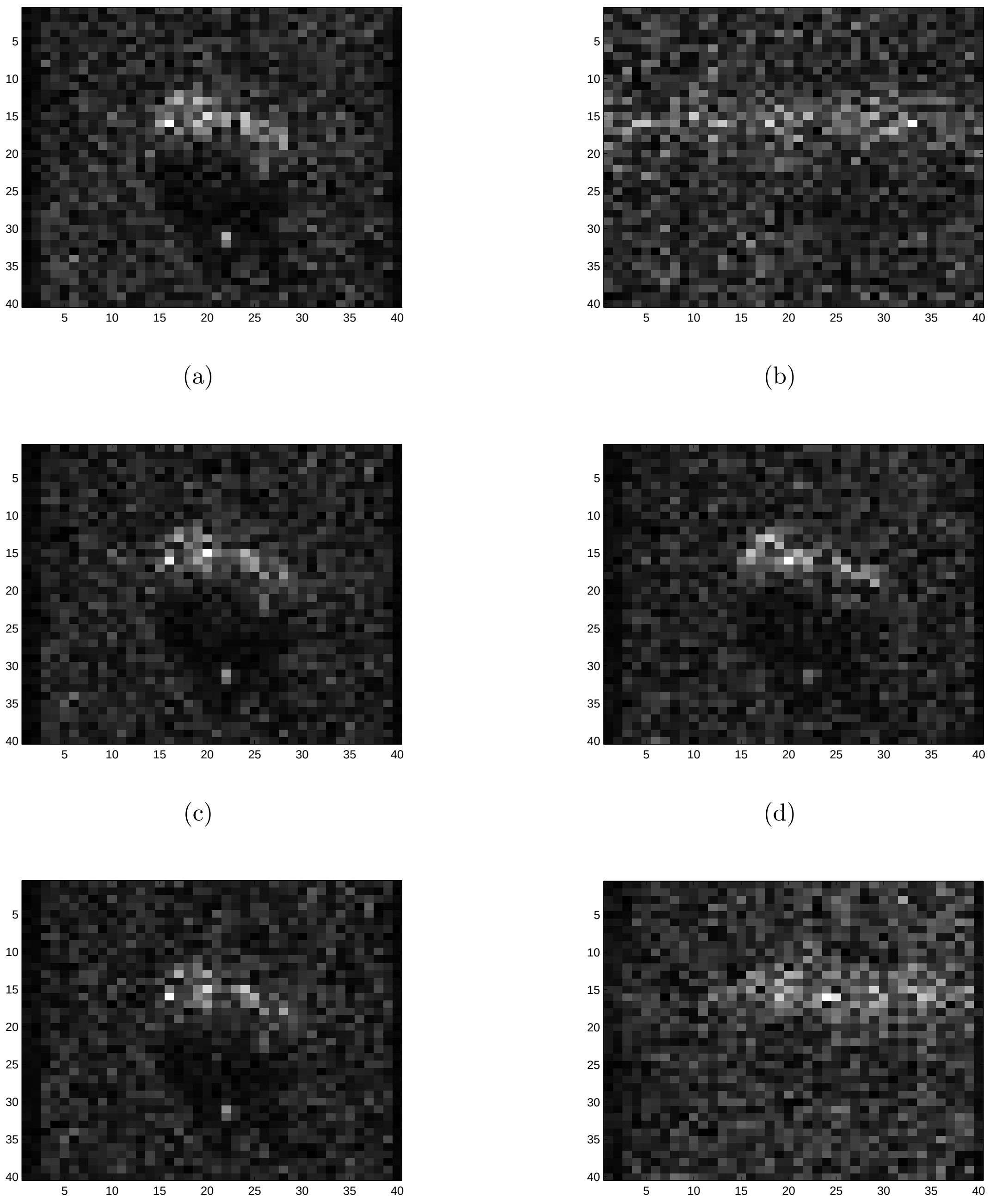

(a) (b) (c) (d) (e) (f)

Figure 4.6: Image restoration using MLA and FMCA: (a) Focused image with SNR=5dB; (b) corrupted image using an *i.i.d.* phase error function and SNR=5dB; (c) MLA restoration for SNR=10dB (phase MSE=0.3697); (d) MLA restoration for SNR=5dB (phase MSE=0.5521); (e) FMCA restoration for SNR=10dB (phase MSE=0.6690); (f) FMCA restoration for SNR=5dB (phase MSE=0.8723).

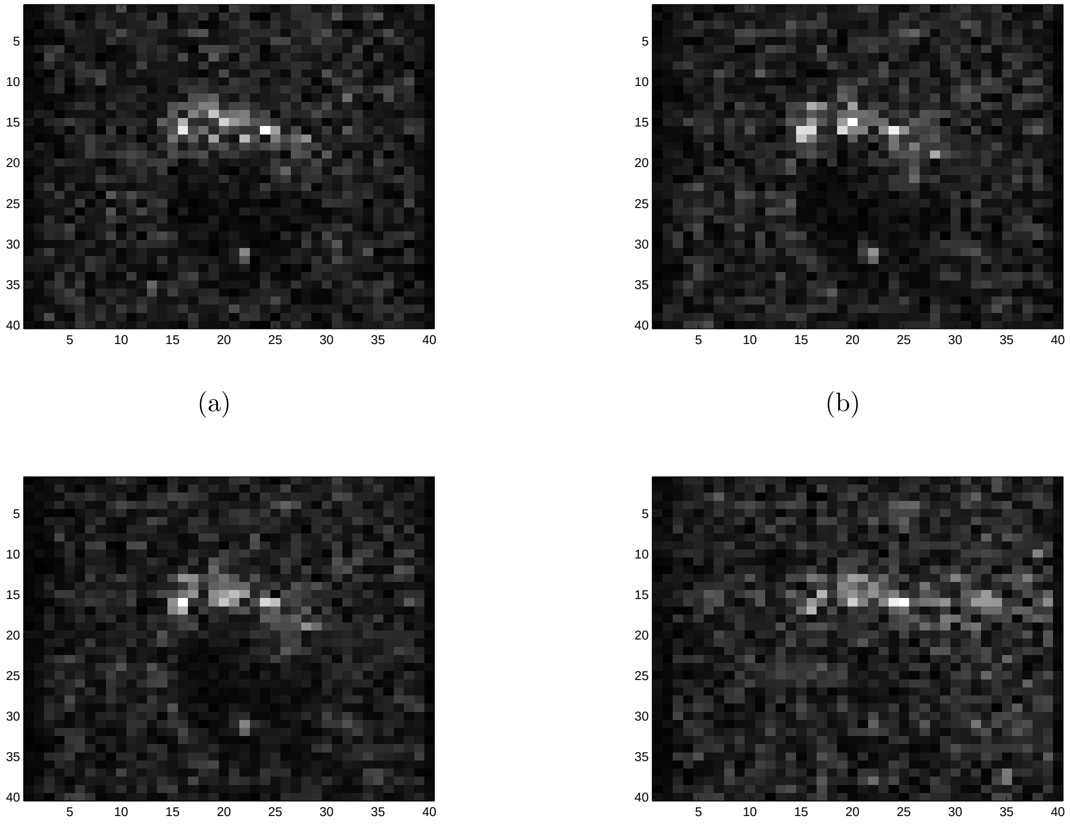

(a) (b)

(c) (d)

Figure 4.7: Model mismatching using rectangular kernel (SNR=5dB): (a) Focused image using exact model; (b) Focused image using mismatched model; (c) MLA restoration (phase MSE=0.2973); (d) FMCA restoration (phase MSE=0.8572).

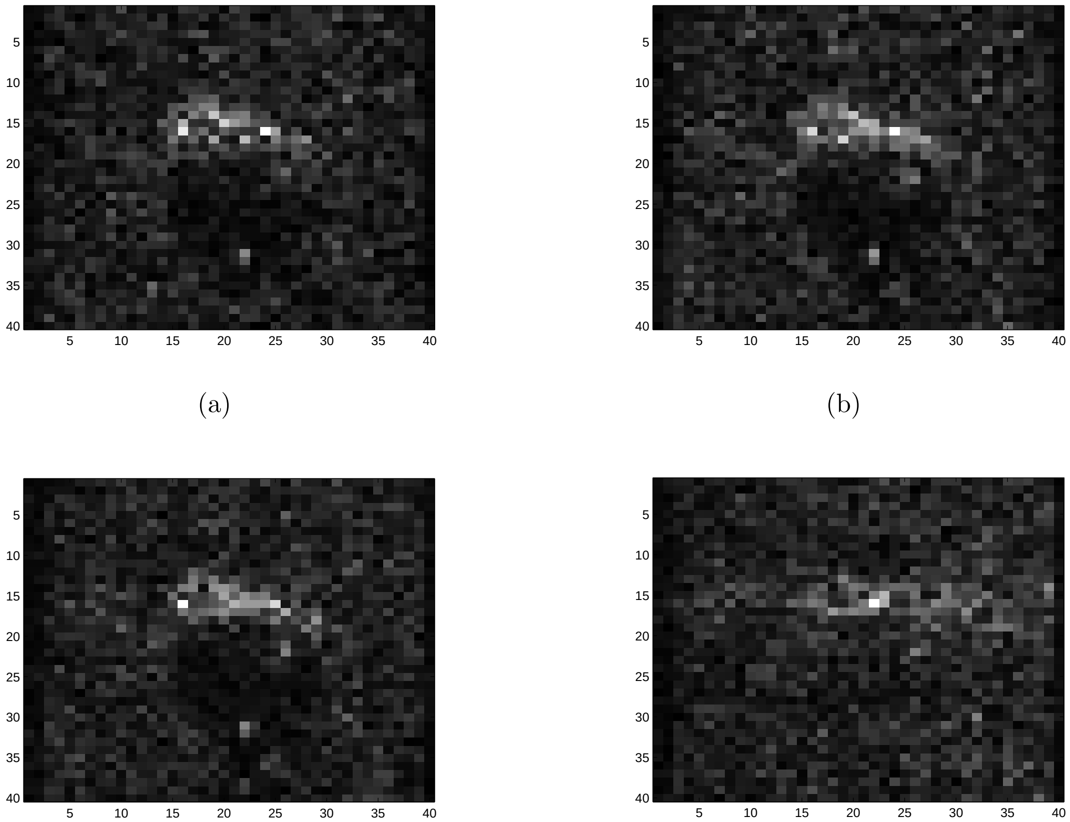

(a)

(b)

(c)

(d)

Figure 4.8: Model mismatching using gaussian kernel (SNR=5dB): (a) Focused image using exact model; (b) Focused image using mismatched model; (c) MLA restoration (phase MSE=0.3205); (d) FMCA restoration (phase MSE=0.7237).

CHAPTER 5

Conclusion and Future Research

In this chapter, we conclude this thesis by summarizing our contributions and proposing future research directions.

5.1 Summary of Contributions

This thesis addressed the autofocus problem in spotlight-mode synthetic aperture radar imaging. The autofocus problem arises from the unavoidable demodulation timing errors in the radar receiver, which comes from inaccurate range measurements or signal propagation effects. The timing errors add phase distortions to the acquired Fourier data, which cause the reconstructed image to suffer distortion, sometimes so severe that the image is completely unrecognizable. The goal is to apply signal processing techniques to compensate for the imperfections of a physical system that would otherwise require expensive hardware improvements. For this purpose, we studied the autofocus problem using a linear algebraic framework. A linear model can be used to accurately characterize a SAR system and autofocus problem when we assume invariance of reflectivity and the transmission of a narrow bandwidth signal. This encompasses a high resolution version of SAR imaging that operates with a high center frequency (often 10 GHz or above). In such scenarios, the autofocus problem becomes extremely important, because a timing error corresponding to even a small fraction of a wavelength can cause the reconstructed image to suffer severe distortion.

SAR autofocus is in general an ill-conditioned inverse problem. In order for the problem to be well defined, previous autofocus methods imposed, either implicitly or explicitly, additional constraints on the underlying image or the imaging system. The small-angle assumption has been at the core of many previous autofocus methods, which presumes the range of look angles of the SAR is sufficiently small. Our first contribution was to extend the successful MCA method to accommodate both the wide-angle monostatic SAR and bistatic SAR scenarios. We called this new autofocus algorithm the Fourier-domain multichannel autofocus (FMCA) method. FMCA was derived within a linear algebraic framework, allowing the phase errors to be corrected in a noniterative fashion. FMCA requires prior knowledge that a region in the underlying scene has zero or nearly-zero pixel values (low-return region). In practice, a low-return region exists in the sidelobes of the antenna pattern. The previously developed MCA approach can be viewed as a special case of FMCA when operating with a very small range of viewing angles.

Our second contribution was to recognize that at the heart of many state-of-the-art autofocus algorithms, including FMCA, is the solution to a constant modulus quadratic program (CMQP). CMQP is known to be NP-hard and previous methods all, either implicitly or explicitly, use eigenvalue relaxation (EVR) to approximate the CMQP. EVR has low computational cost but is very sensitive to noise. We proposed the use of semidefinite relaxation (SDR) to approximate the CMQP. SDR provides a tighter approximation to CMQP than does EVR, but at the cost of higher computational cost. However, there may be crucial situations where it is imperative that an image be focused as well as possible, using computationally intensive off-line processing. SDR recently has been applied to many problems in communications and signal processing, but this is the first time that SDR has been applied to the problem of SAR autofocus.

Our last contribution was the study of the autofocus problem using a bilinear parametric model. We analyzed the conditions for identifiability and solvability of the problem in the noiseless case, and then derived a novel maximum likelihood autofocus (MLA) method to deal with noisy observations. Under small-angle assumption, MLA coincides with the MCA technique. Under more realistic conditions, MLA outperforms FMCA, and is applicable to a broader class of scenarios. The main advantages of MLA, when compared to previous methods, is its reliance on a rigorous statistical model and its optimality within this setting.

5.2 Future Research Directions

As future research, we propose three directions that are direct extensions of our current work.

5.2.1 System Identification of MLA

A question remains to be answered regarding the identifiability of the bilinear system describing the SAR autofocus problem, shown in equation (4.12), in the noiseless case. Recall that MCA, FMCA and MLA phase estimation all can be expressed as the following CMQP:

$$\hat{\boldsymbol{\phi}} = \underset{\boldsymbol{\gamma} \in \Gamma}{\operatorname{argmin}} \left\| \mathbf{A} \boldsymbol{\gamma} \right\|^2 , \tag{5.1}$$

where

$$\mathbf{A} = \left(\mathbf{I} - \mathbf{L}\mathbf{L}^{\dagger} \right) \tilde{\mathbf{Y}} \tag{5.2}$$

for MLA and

$$\mathbf{A} = [\mathbf{L}^{\dagger}]_a \tilde{\mathbf{Y}} \tag{5.3}$$

for MCA and FMCA. The original MCA and FMCA developments require rank($\mathbf{A}$) = $M - 1$ to ensure the problem has a unique solution. However, due to the restricted solution space Γ, having rank equal to $M-1$ is only a sufficient condition. Moreover, we find that the rank $M-1$ condition is often too strong in many practical situations. This motivates us to study when the condition (4.15) in theorem 4.1 will be satisfied.

5.2.2 Modeling of Reflectivity Function

An additional direction for future work concerns the use of a more detailed reflectivity function model. Since we are only interested in recovering the magnitude of the reflectivity function for display, a more pertinent formulation would model the amplitudes and the phases of this function separately as done in [65]. In summary, the model of a radar scene is based on the fact that the received radar returns are the superpositions of the reflectors in the underlying target scene. For a typical SAR system, the image resolving capability is determined once the system specification is set. That is, depending on the SAR system specification, we can decompose the target scene into resolution cells where any two point reflectors within a resolution cell cannot be well-resolved. The SAR system collects a single backscatter coefficient for each resolution cell; denote this complex coefficient as $\theta[u,v]$. To simplify the problem formulation, we assume that $\theta[u,v]$ depends only on scatterers within cell (u,v).

From the above discussion, $\theta[u,v]$ can be expressed as

$$\theta[u,v] = \sum_{l \in \mathrm{cell}(u,v)} a_l e^{j\varphi_l} \tag{5.4}$$

where a_l represents the energy reflected from scatterer l and φ_l is the total phase shift of scatterer l due to reflection and the signal propagation delay. By introducing assumptions such as independence of the φ_l and the presence of many scatterers within a resolution cell it can be justified that $\theta[u,v]$ is well modeled as a circular symmetric Gaussian random variable. The magnitude of $\theta[u,v]$ will have a Rayleigh distribution and the squared magnitude $|\theta[u,v]|^2$ will have an exponential distribution, whereas the phase of $\theta[u, v]$ will be distributed uniformly on $[-\pi, \pi]$. Using this model, we can study how to estimate the amplitudes and the phases of the reflectivity function separately.

5.2.3 Computational Issues of MLA

An important research direction for future work involves reduction of the computational cost of MLA. From a practical point of view, implementing MLA as in (4.35) would be very expensive computationally. The bottleneck of the computation is evaluation of the pseudo-inverse of $\mathbf{L}$, $\mathbf{L}^\dagger$, which then relies on the factorization of $\mathbf{L}$ using singular value decomposition (SVD). The number of computations to compute the SVD of $\mathbf{L}$ (a $MN \times D$ matrix) is on the order of $\mathcal{O}(MND^2 + D^3)$ [72], which scales poorly with image size. We would like to address the computational issue of the pseudo-inverse of $\mathbf{L}$. Here we propose one possible way to simplify the computation of $\mathbf{L}^\dagger$ by using approximation. We borrow an idea from previous autofocus methods and approximate $\mathbf{L}^\dagger$ using polar-to-Cartesian interpolation and FFT. The advantage of using this approach is that we can have control over the tradeoff between accuracy and complexity. One extreme, we can choose the interpolation coefficients to perform $\mathbf{L}^\dagger$ exactly. More specifically, we can express $\mathbf{L}^\dagger$ as the identity

$$\mathbf{L}^\dagger = \mathbf{W}^H \mathbf{W} \mathbf{L}^\dagger, \tag{5.5}$$

where $\mathbf{W}$ denotes a MN point DFT matrix, and choose the interpolation coefficients as the realization of $\mathbf{W}\mathbf{L}^\dagger$. At the other extreme, we can choose the interpolation matrix to be the identity matrix, in which case we only need to perform an FFT, in which case the computational cost is reduced to $\mathcal{O}(D \log D)$. Of course, we do not expect good performance in this example. Another possibility is to use conventional SAR processing with a spatially-invariant interpolation kernel (e.g. sinc kernel) with the k nearest points. This interpolator would need MN time to find the k nearest points and an additional k time to calculate the interpolation coefficients, thus a total cost of $\mathcal{O}(DMNk + D\log D)$. We can choose k to control the tradeoff between accuracy and complexity.

It is important to emphasize that the computation of $\mathbf{L}^{\dagger}$ is data independent and only depends on the system specification. In other words, we only need to precompute $\mathbf{L}^{\dagger}$ once for every system setup and use it for all subsequent image formation. We would like to study other computationally efficient methods for solving or approximating the pseudo-inverse operation.

BIBLIOGRAPHY

BIBLIOGRAPHY

[1] Y. Wu and D. C. Munson, Jr., "Multistatic synthetic aperture imaging of aircraft using reflected television signals," *Proc. of SPIE, Algorithms for synthetic aperture radar imagery VIII*, vol. 4382, Apr. 2001.

[2] D. C. Munson, Jr. and R. L. Visentin, "A signal processing view of strip-mapping synthetic aperture radar," *IEEE Trans. on Acoustics,Speech,and Signal Processing*, vol. 37, no. 12, pp. 2131–2147, Dec. 1989.

[3] K. Liu and D. C. Munson, Jr., "Autofocus in multistatic passive SAR imaging," *IEEE International Conference on Acoustics, Speech and Signal Processing*, pp. 1277–1280, Mar. 2008.

[4] D. C. Munson, Jr., J. D. O'Brien, and W. K. Jenkins, "A tomographic formulation of spotlight-mode synthetic aperture radar," *Proc. of the IEEE*, vol. 71, pp. 917–925, Aug. 1983.

[5] C. V. Jakowatz, Jr., D. E. Wahl, P. H. Eichel, D. C. Ghiglia, and P. A. Thompson, *Spotlight-Mode Synthetic Aperture Radar: A Signal Processing Approach.* Boston: Kluwer Academic Publishers, 1996.

[6] D. C. Munson, Jr. and J. L. C. Sanz, "Image reconstruction from frequency-offset Fourier data," *Proc. of the IEEE*, vol. 72, no. 6, pp. 661–669, Jun. 1984.

[7] S. Basu and Y. Bresler, "$\mathcal{O}(n^2 \log 2n)$ filtered backprojection reconstruction algorithm for tomography," *IEEE Trans. on Image Processing*, vol. 9, pp. 1760–1773, Oct. 2000.

[8] A. Boag, Y. Bresler, and E. Michielssen, "A multilevel domain decomposition algorithm for fast $\mathcal{O}(n^2 \log n)$ reprojection of tomographic images," *IEEE Trans. on Image Processing*, vol. 9, pp. 1573–1582, Sept. 2000.

[9] M. D. Desai and W. K. Jenkins, "Convolution backprojection image reconstruction for spotlight mode synthetic aperture radar," *IEEE Trans. on Image Processing*, vol. 1, no. 4, pp. 505–517, Oct. 1992.

[10] Y. Ding and D. C. Munson, Jr., "A fast back-projection algorithm for bistatic SAR imaging," *IEEE International Conference on Image Processing*, vol. 2, pp. 449–452, Jun. 2002.

[11] S. Xiao, D. C. Munson, Jr., S. Basu, and Y. Bresler, "An $n^2 \log n$ back-projection algorithm for SAR image formation," *Asilomar Conference on Signals, Systems, and Computers 2000*, pp. 3–7, Oct. 2000.

[12] O. Arikan and D. C. Munson, Jr., "A tomographic formulation of bistatic synthetic aperture radar," *Intern. Conf. on Advances in Communication and Control Systems*, pp. 289–302, Oct. 1988.

[13] G. A. Bendor and T. W. Gedra, "Single-pass fine-resolution SAR autofocus," *Proc. of IEEE National Aerospace and Electronics Conference NAE-CON, Dayton, Ohio*, pp. 482–488, May 1983.

[14] T. C. Calloway and G. Donohoe, "Subaperture autofocus for synthetic apterture radar," *IEEE Trans. on Aerospace and Electronic Systems*, vol. 30, no. 2, pp. 617–621, Apr. 1994.

[15] C. E. Mancill and J. M. Swiger, "A map drift autofocus technique for correcting higher-order SAR phase errors," *Proc. 27th Annu. Tri-Service Radar Symp., Monterey, CA*, pp. 391–400, Jun. 1981.

[16] C. Jakowatz, Jr. and D. Wahl, "Eigenvector method for maximum-likihood estimation of phase errors in synthetic-aperture-radar imagery," *J. Opt. Soc. Am. A*, vol. 10, no. 12, pp. 2539–2546, Dec. 1993.

[17] W. Ye, T. Yeo, and Z. Bao, "Weighted least-squares estimation of phase errors for SAR/ISAR autofocus," *IEEE Trans. on Geoscience and Remote Sensing*, vol. 37, pp. 2487–2494, Sept. 1999.

[18] D. E. Wahl, P. H. Eichel, D. C. Ghiglia, and C. V. Jakowatz, Jr., "Phase gradient autofocus - a robust tool for high resolution SAR phase correction," *IEEE Trans. on Aerospace and Electronic Systems*, vol. 30, no. 3, pp. 827–835, Jul. 1994.

[19] P. H. Eichel, D. C. Ghiglia, C. V. Jakowatz, Jr., and D. E. Wahl, "Phase-gradient autofocus for SAR phase correction: explanation and demonstration of algorithmic steps," *Proc. of the IEEE Digital Signal Processing Workshop at Starved Rock State Park, IL*, pp. 6.6.1–6.6.2, Sept. 1992.

[20] P. Eichel and C. V. Jakowatz, Jr., "Phase-gradient algorithm as an optimal estimator of the phase derivative," *Optics Letters*, vol. 14, pp. 1101–1103, Oct. 1989.

[21] T. J. Kragh, "Monotonic iterative algorithm for minimum-entropy autofocus," in *Adaptive Sensor Array Processing Workshop*, Jun. 2006.

[22] L. Xi, L. Guosui, and J. Ni, "Autofocusing of ISAR images based on entropy minimization," *IEEE Trans. on Aerospace and Electronic Systems*, vol. 35, no. 4, pp. 1240–1252, Oct. 1999.

[23] F. Berizzi and G. Corsini, "Autofocusing of inverse synthetic aperture radar images using contrast optimization," *IEEE Trans. on Aerospace and Electronic Systems*, vol. 32, pp. 1185–1191, Jul. 1996.

[24] R. G. Paxman and J. C. Marron, "Aberration correction of speckled imagery with an image sharpness criterion, san diego, ca," *In Proc. of the SPIE Conference on Statistical Optics*, vol. 976, Aug. 1988.

[25] R. L. Morrison, Jr. and D. C. Munson, Jr., "An experimental study of a new entropy based SAR autofocus technique," *IEEE International Conference on Image Processing*, vol. 2, pp. 441–444, Dec. 2002.

[26] R. L. Morrison, Jr., D. C. Munson, Jr., and M. N. Do, "Avoiding local minima in entropy-based SAR autofocus," *IEEE workshop on statistical signal processing*, pp. 454–457, Sept. 2003.

[27] M. P. Hayes and S. A. Fortune, "Recursive phase estimation for image sharpening," *Image and Vision Computing, Dunedin, New Zealand*, Nov. 2005.

[28] J. R. Fienup and J. J. Miller, "Aberration correction by maximizing generalized sharpness metrics," *Journal of Optical Society of America*, 2003.

[29] R. L. Morrison, Jr., M. N. Do, and D. C. Munson, Jr., "MCA: A multichannel approach to SAR autofocus," *IEEE Trans. on Image Processing*, vol. 18, pp. 840 – 853, Apr. 2009.

[30] H. Cho and D. C. Munson, Jr., "Overcoming polar-format issues in multichannel SAR Autofocus," *Proc. 42nd Asilomar Conference on Signals, Systems and Computers*, pp. 523–527, Oct. 2008.

[31] M. Gurelli and C. Nikias, "EVAM: An eigenvector-based algorithm for multichannel blind deconvolution of input colored signals," *IEEE Trans. on Signal Processing*, vol. 43, no. 1, pp. 134–149, Jan. 1995.

[32] G. Harikumar and Y. Bresler, "Blind restoration of images blurred by multiple filters: Theory and efficient algorithms," *IEEE Trans. on Image Processing*, vol. 8, no. 2, pp. 202–219, Jun. 1999.

[33] Z. Luo and W. Yu, "An introduction to convex optimization for communications and signal processing," *IEEE Journal on Selected Areas in Communications*, vol. 24, pp. 1426–1438, Aug. 2006.

[34] W. Ma, T. N. Davidson, K. M. Wong, Z. Q. Luo, and P. C. Ching, "Quasimaximum-likelihood multiuser detection using semi-definite relaxation with application to synchronous CDMA," *IEEE Trans. on Signal Processing*, vol. 50, pp. 912–922, Apr. 2002.

[35] W. Ma, P. Ching, and Z. Ding, "Semidefinite relaxation based multiuser detection for M-ary PSK multiuser systems," *IEEE Journal on Selected Areas in Communications*, vol. 52, pp. 2862– 2872, Oct. 2004.

[36] M. X. Goemans and D. P. Williamson, "Improved approximation algorithms for maximum cut and satisfiability problem using semi-definite programming," *Journal of ACM*, vol. 42, pp. 1115–1145, Nov. 1995.

[37] A. Wiesel, Y. Eldar, and S. Shitz, "Semidefinite relaxation for detection of 16-QAM signaling in MIMO channels," *IEEE Signal Processing Letters*, vol. 12, no. 9, pp. 653–656, Sept. 2005.

[38] M. Abdi, H. El Nahas, A. Jard, and E. Moulines, "Semidefinite positive relaxation of the maximum-likelihood criterion applied to multiuser detection in a CDMA context," *IEEE Signal Processing Letter*, vol. 9, pp. 165–167, Jun. 2002.

[39] J. Jalden, C. Martin, and B. Ottersten, "Semidefinite programming for detection in linear systems - optimality conditions and space-time decoding," *IEEE International Conference on Acoustics, Speech, and Signal Processing*, vol. 4, pp. 9–12, Apr. 2003.

[40] P. H. Tan and L. K. Rasmussen, "The application of semidefinite programming for detection in CDMA," *IEEE Journal on Selected Areas in Communication*, vol. 19, pp. 1442–1449, Oct. 2001.

[41] X. M. Wang, W. S. Lu, and A. Antoniou, "A near-optimal multiuser detector for DS-CDMA systems using semidefinite programming relaxation," *IEEE Trans. on Signal Processing*, vol. 51, pp. 2446–2450, Sept. 2003.

[42] U. Zwich, "Outward rotations: a new tool for rounding solutions of semidefinite programming relaxations, with application to MAX-CUT and other problems," *Proc. of 31st ACM Symposium on Theory of Computing*, pp. 679 – 687, May 1999.

[43] U. Feige and M. Langberg, "The RPR^2 rounding technique for semidefinite programs," *Proc. of 28th International Colloquium on Automata, Languages and Programming, Crete, Greece*, pp. 213–224, Jul. 2001.

[44] S. Zhang and Y. Huang, "Complex quadratic optimization and semidefinite programming," *SIAM Journal on Optimization*, vol. 16, pp. 871–890, Jul. 2006.

[45] M. So, J. Zhang, and Y. Ye, "On approximating complex quadratic optimization problems via semidefinite programming relaxations," *Mathematical Programming*, vol. 110, no. 1, pp. 93–110, Jun. 2007.

[46] A. Singer, "Angular synchronization by eigenvectors and semidefinite programming," *Applied and Computational Harmonic Analysis*, vol. 30, pp. 20–36, Jan. 2011.

[47] S. Boyd and L. Vandenberghe, *Convex Optimization*. Cambridge University Press, Mar. 2004.

[48] L. Vandenberghe and S. Boyd, "Semidefinite programming," *SIAM Review*, vol. 38, no. 1, pp. 49–95, Mar. 1996.

[49] J. Sturm, "Using SeDuMi 1.02, a MATLAB toolbox for optimization over symmetric cones," *Optimization Methods and Software*, pp. 625–653, 1999.

[50] R. Monteiro, "First- and second-order methods for semidefinite programming," *Mathematical Programming*, vol. 97, pp. 209–244, May 2003.

[51] Z. Wen, D. Goldfarb, and W. Yin, "Alternating direction augmented lagrangian methods for semidefinite programming," Dept of IEOR, Columbia University, Tech. Rep., 2009.

[52] C. Helmberg and F. Rendl, "A spectral bundle method for semidefinite programming," *SIAM Journal on Optimization*, vol. 10, pp. 673–696, 1997.

[53] C. Helmberg, "A cutting plane algorithm for large scale semidefinite relaxations in the sharpest cut," MPS/SIAM Ser. Optim, Tech. Rep., 2001.

[54] S. Verdu, "Computational complexity of optimum multiuser detection," *Algorithmica*, vol. 4, pp. 303–312, Jun. 1989.

[55] A. Ben-Tal, A. Nemirovski, and C. Roos, "Extended matrix cube theorems with applications to μ-theory in control," *Mathematics of Operations Research*, vol. 23, pp. 497–523, Jul. 2003.

[56] M. Goemans, "Semidefinite programming in combinatorial optimization," *Mathematical Programming*, pp. 143 – 161, Oct. 1997.

[57] A. Nemirovski, C. Roos, and T. Terlaky, "On maximization of quadratic form over intersection of ellipsoids with common center," *Mathematical Programming*, pp. 463–473, 1999.

[58] A. Ben-Tal, A. Nemirovski, and C. Roos, " Extended Matrix Cube Theorems with applications to μ-Theory in Control," *Mathematics of Operations Research*, vol. 28, pp. 497–523, 2003.

[59] K. Liu and D. C. Munson, Jr., "Fourier-domain multichannel autofocus for synthetic aperture radar," *42nd Asilomar Conference on Signals, Systems and Computers*, pp. 848 – 852, Oct. 2008.

[60] ——, "Fourier-domain multichannel autofocus for synthetic aperture radar," *Accepted by IEEE Trans. on Image Processing, DOI (identifier) 10.1109/TIP.2011.2156421.*

[61] V. Patel, G. Easley, D. Healy, and R. Chellappa, “Compressed synthetic aperture radar,” *IEEE Journal on Selected Topics in Signal Processing*, vol. 4, pp. 244–254, Apr. 2010.

[62] I. Stojanovic and W. Karl, “Imaging of moving targets with multi-static SAR using an overcomplete dictionary,” *IEEE Journal on Selected Topics in Signal Processing*, vol. 4, pp. 164–176, Feb. 2010.

[63] M. Cetin, W. Karl, and D. Castanon, “Feature enhancement and ATR performance using nonquadratic optimization-based SAR imaging,” *IEEE Trans. on Aerospace and Electronic Systems*, vol. 39, pp. 1375–1395, Oct. 2003.

[64] M. Cetin and W. Karl, “Feature-enhanced and ATR performance using nonquadratic optimization-based SAR imaging,” *IEEE Trans. on Aerospace and Electronic Systems*, vol. 10, no. 4, pp. 623–631, Apr. 2001.

[65] S. N. Madsen, “Spectral properties of homogeneous and nonhomogeneous radar images,” *IEEE Trans. on Aerospace and Electronic Systems*, vol. AES-23, no. 4, pp. 583–588, Jul. 1987.

[66] A. O. Hero, R. Piramuthu, and J. A. Fessler, “Minimax emission computed tomography using high-resolution anatomical side information and B-Spline models,” *IEEE Trans. on Information Theory*, vol. 45, no. 3, pp. 920–938, Apr. 1999.

[67] J. C. Ye, Y. Bresler, and P. Moulin, “Asymptotic global confidence regions in parametric shape estimation problems,” *IEEE Trans. on Information Theory*, vol. 46, pp. 1991–1895, Aug. 2000.

[68] ——, “Cramer-Rao bounds for 2-D Target shape estimation in nonlinear inverse scattering problems with application to passive radar,” *IEEE Trans. on Antennas and Propagation*, vol. 5, pp. 771–783, May 2001.

[69] ——, “Cramer-Rao bounds for parametric shape estimation in inverse problems,” *IEEE Trans. on Image Processing*, vol. 12, no. 1, pp. 71–84, Jan. 2003.

[70] S. M. Kay, *Fundamentals of Statistical Signal Processing.* Prentice Hall, 1993.

[71] Center for Imaging Science Image Database. [Online]. Available: http://cis.jhu.edu/data.sets/MSTAR

[72] T. K. Moon and W. C. Stirling, *Mathematical Methods and Algorithms for Signal Processing.* Upper Saddle River, NJ: Prentice Hall, 2000.